RADAR STUDIES OF ATYPICAL EQUATORIAL SPREAD *F* EVENTS IN THE AMERICAN SECTOR

by

Weijia Zhan

APPROVED BY SUPERVISORY COMMITTEE:

Fabiano Rodrigues, Chair

Roderick Heelis

Russell Stoneback

Cesar Valladares

Lindsay King

Copyright © 2019

Weijia Zhan

All rights reserved

This dissertation

is dedicated to my parents,

who supported me with full love

all the time.

RADAR STUDIES OF ATYPICAL EQUATORIAL SPREAD *F* EVENTS IN THE AMERICAN SECTOR

by

WEIJIA ZHAN, BE, MS

DISSERTATION

Presented to the Faculty of

The University of Texas at Dallas

in Partial Fulfillment

of the Requirements

for the Degree of

DOCTOR OF PHILOSOPHY IN

PHYSICS

THE UNIVERSITY OF TEXAS AT DALLAS

December 2019

ACKNOWLEDGMENTS

First of all, I would give my most sincere gratitude to my advisor, Dr. Rodrigues. To fulfill this dissertation, I must thank Dr. Rodrigues for his excellent guidance in my research. This work could not have been done without his full support, patience and helpful discussions. I also appreciate very much the help from my dissertation committee members. Dr. Valladares was always kind and patient to answer my questions. Dr. Heelis always gave insightful views on the topics in my research. I can always feel the passion and kindness Dr. King has when I talk to her and seek for help. Thanks to Dr. Stoneback for providing C/NOFS data and giving useful advice on analyzing it. In addition, I must thank Sam Shidler. We have worked in the same office for more than three years. We have had constructive discussions in research and he can always give helpful hints. I also got to know more about the American culture and life during our conversations after work or during lunch. I also thank everyone at the Center for Space Sciences. I have really enjoyed the comfortable and happy life everyday here. The past four and a half years at the Center and at UT Dallas were a really wonderful experience in my life.

Work at UT Dallas was partially supported by NASA (80NSSC18K1203) and NSF (AGS-1554926). This dissertation used observations made by the Jicamarca Radio Observatory in Peru and by the MELISSA radar system in Brazil. The Jicamarca Radio Observatory is a facility of the Instituto Geofisico del Peru operated with support from the NSF (AGS-1433968) through Cornell University. The development, deployment and maintenance of the MELISSA system was supported by an AFOSR award (FA9550-13-1-0095) to UT Dallas. This work uses the SAMI2 ionosphere model written and developed by the Naval Research Laboratory. Finally, I would like to thank Dr. Nicholas Pedatella (NCAR-HAO) for making WACCM-X simulation results available to our study.

October 2019

RADAR STUDIES OF ATYPICAL EQUATORIAL SPREAD F EVENTS IN THE AMERICAN SECTOR

Weijia Zhan, PhD
The University of Texas at Dallas, 2019

Supervising Professor: Fabiano Rodrigues, Chair

Equatorial spread F (ESF) is the name given, for historical reasons, to the manifestation of a broad range of ionospheric F-region irregularities observed at low latitudes. Since the report of ESF by *Booker and Wells* (1938), a large number of efforts have been dedicated to studies of ESF events. These efforts led to a significant improvement of our understanding of typical, post-sunset ESF. Recently, however, renewed attention has been devoted to atypical ESF events. That is, to events that occurred in the post-midnight sector and/or June solstice conditions. The efforts of this dissertation contribute to a better understanding of atypical ESF events with focus on the American sector.

We evaluated the hypothesis of weakening vertical plasma drifts creating favorable conditions for the generation of postmidnight ESF. We used numerical simulations aided by incoherent scatter radar measurements of a prototypical event observed at the Jicamarca Radio Observatory (JRO) to test this hypothesis during June solstice, low solar flux conditions in the American sector ($\sim$75°W). We found that the weakening drifts did produce unstable conditions with positive growth rates. The growth rates, however, were much slower than those obtained for typical, premidnight ESF events and those obtained for similar drift conditions in other longitude sectors. Further numerical analyses showed that the action

of converging neutral winds, in combination with weakening drifts, could have produced favorable conditions for instability development.

Next, we used long-term coherent backscatter radar (Jicamarca Unattended Long-term Investigations of the ionosphere and Atmosphere, JULIA) measurements made at the JRO to better understand the morphology and origin of the postmidnight ESF irregularities in the American sector. The study is motivated by high occurrence rates of postmidnight ESF observed by the C/NOFS satellite during the 2008/2009 solar minimum. Collocated digisonde observations provide additional insight on F-region conditions leading to these ESF events. The radar observations show that ESF events during December solstice start in the postsunset sector. These ESF events and the conditions for their development are shown to continue through midnight hours. The predominance of postmidnight irregularities on satellite observations during December solstice is explained by the slow vertical development of the ESF structures, which only reach the topside near midnight in most cases. In June solstice, however, JULIA observations show that ESF started predominately in the midnight to postmidnight sector.

Finally, we also maintained, processed and analyzed measurements made by a 30 MHz coherent backscatter radar system located in the low-latitude site of São Luis, Brazil in the eastern American sector ($\sim$45°W). This radar system is referred to as Measurements of Equatorial and Low-latitude Ionospheric irregularities over São Luís, South America (MELISSA) and made observations between March 2014 and December 2018. We analyzed pre- and postmidnight F-region echoes with focus on the spectral features of postmidnight echoes and how they compare to spectra of echoes observed in the post-sunset sector. The radar observations indicate that post-midnight F-region irregularities were generated locally, and were not a result of "fossil" structures generated earlier in time (in other longitude sectors) and that drifted into the radar field of view. This also includes cases where the echoes are weak and that would be associated with decaying ESF structures. Collocated digisonde observations

show modest but noticeable F-region apparent uplifts prior to post-midnight ESF events. We associate the equatorial uplifts with disturbed dynamo effects and with destabilizing F-region conditions leading to ESF development.

TABLE OF CONTENTS

ACKNOWLEDGMENTS v

ABSTRACT vi

LIST OF FIGURES xii

LIST OF TABLES xvi

CHAPTER 1 INTRODUCTION 1

1.1 The low-latitude ionosphere 1

1.2 Ionospheric $\mathbf{E} \times \mathbf{B}$ drifts 2

1.3 Ionospheric conductivities and currents 5

1.4 Thermospheric winds and vertical drifts 7

1.5 The pre-reversal enhancement (PRE) 8

1.6 The Generalized Rayleigh-Taylor instability and ESF 9

1.7 Typical, post-sunset ESF 11

1.8 On radar observations of ESF 13

CHAPTER 2 MOTIVATION AND SCIENCE QUESTIONS 15

2.1 Background and Motivation 16

2.2 Specific Science Questions 19

CHAPTER 3 JUNE SOLSTICE EQUATORIAL SPREAD-F IN THE AMERICAN SECTOR: A NUMERICAL ASSESSMENT OF LINEAR STABILITY AIDED BY INCOHERENT SCATTER RADAR MEASUREMENTS 23

3.1 Introduction 24

3.2 Measurements, Models and Analyses 26

3.2.1 Radar measurements 26

3.2.2 Low-latitude ionospheric modeling 27

3.2.3 Numerical assessment of F-region stability 28

3.3 Results and Discussion 29

3.3.1 Weakening vertical plasma drifts 29

3.3.2 SAMI2 simulations: Apparent uplifts 31

3.3.3 SAMI2 simulations: Linear growth rates 32

3.3.4 Comparisons with typical ESF conditions . . . 35
3.3.5 Thermospheric wind effects . . . 37
3.4 Summary and Conclusions . . . 43
CHAPTER 4 ON THE GENESIS OF POST-MIDNIGHT EQUATORIAL SPREAD-F: RESULTS FOR THE AMERICAN/PERUVIAN SECTOR . . . 45
4.1 Introduction . . . 46
4.2 Measurements and Analyses . . . 48
4.2.1 Measurements . . . 48
4.2.2 Analyses . . . 49
4.3 Results and Discussion . . . 50
4.3.1 On post-sunset ESF . . . 51
4.3.2 On post-midnight ESF . . . 52
4.4 Conclusions . . . 58
CHAPTER 5 MELISSA: SYSTEM DESCRIPTION AND SPECTRAL FEATURES OF PRE- AND POST-MIDNIGHT F-REGION ECHOES . . . 60
5.1 Introduction . . . 61
5.2 Instrumentation, Observations and Analysis . . . 64
5.2.1 Instrumentation: MELISSA . . . 64
5.2.2 Observations . . . 66
5.2.3 Spectral Analysis . . . 67
5.3 Results and Discussion . . . 69
5.3.1 Pre-midnight F-region echoes . . . 70
5.3.2 Post-midnight F-region echoes . . . 73
5.3.3 Potential origin of the observed post-midnight uplifts . . . 78
5.4 Summary . . . 81
CHAPTER 6 CONCLUSIONS . . . 84
6.1 On the role of weakening downward drifts in the generation of postmidnight ESF . . . 84
6.2 On the genesis of postmidnight ESF . . . 85
6.3 On the spectral features of pre- and post-midnight ESF . . . 85

6.4 Future work 87
APPENDIX ON THE QUIET-TIME DAY-TO-DAY VARIABILITY OF VERTICAL DRIFTS AND POSTMIDNIGHT ESF 88
A.1 Introduction 88
A.2 Methodology 90
A.2.1 SAMI2 90
A.2.2 WACCM-X 91
A.2.3 Climatological Drift Model (SF99) 92
A.2.4 GRT Linear Growth Rate 93
A.3 Results and Discussion 93
A.3.1 On WACCM-X drifts 93
A.3.2 On SF99 Drifts with WACCM-X Variabilities 95
A.3.3 Linear Growth Rate Results 96
A.4 Concluding Remarks 98
REFERENCES 108
BIOGRAPHICAL SKETCH 122
CURRICULUM VITAE

LIST OF FIGURES

1.1 Typical vertical profiles of electron density in the mid-latitude ionosphere. From *Hargreaves* (1992) 2

1.2 Relative magnitude and direction of ion and electron velocities produced by the direct action of neutral winds and electric fields. Approximate locations of the E- and F-regions are shaded (*Heelis*, 2004). 4

1.3 The markers and thick lines show averaged vertical $\mathbf{E} \times \mathbf{B}$ drifts measured at the Jicamarca Radio Observatory near the magnetic equator. The error bars represent the variability of the drift measurements used in the averages. The thin lines show predictions of a climatological model. Columns from left to right correspond to equinox, June solstice and December solstice, respectively. Rows from top to bottom correspond to high, moderate and low solar flux conditions, respectively. From *Scherliess and Fejer* (1999). 5

1.4 Typical height profiles of the ionospheric conductivities for nighttime (left) and daytime (right) conditions. Produced by the ionospheric conductivity model at the World Data Center for Geomagnetism, Kyoto (`http://wdc.kugi.kyoto-u.ac.jp/ionocond/sightcal/index.html`). The dark solid line, light solid line and dashed line indicate parallel, Pedersen and Hall conductivities, respectively. 7

1.5 Prototypical wind pattern in the E-region as a function of latitude and local time for the northern hemisphere (*Tarpley*, 1970). 8

1.6 A schematic diagram of PRE (*Farley et al.*, 1986). 9

1.7 A schematic representation of the Rayleigh-Taylor instability in the equatorial ionosphere. From *Kelley* (2009). 10

1.8 Sequential sketches made from photos of the hydrodynamic Rayleigh-Taylor instability. A heavy fluid is initially supported by a transparent lighter fluid. From *Kelley* (2009). 10

1.9 Range-Time-Intensity (RTI) maps showing examples of post-sunset (a) bottom-type, (b) bottomside, (c) topside, and (d) post-midnight ESF radar events. These measurements were made by the JULIA radar system of the Jicamarca Radio Observatory. 14

3.1 (Top) Range-Time-Intensity (RTI) map for June 4-5, 2008. (Middle) Jicamarca ISR vertical drifts as a function of local time and height; positive values for upward drifts. (Bottom) Black markers shown mean vertical drifts for an altitude around 300 km. Red line shows interpolated drifts. 29

3.2 (Top) Range-Time-Intensity (RTI) map for June 4-5, 2008. (Middle) Mean vertical drifts for an altitude around 300 km. (Bottom) Digisonde estimates of the virtual height of the base of the F-layer (h'F) as a function of local time. 31

3.3 (Top) Model vertical drifts used to drive SAMI2. (Bottom) SAMI2 results of the electron density for Jicamarca. Iso-contours of electron density are also shown to help identify the behavior of the equatorial F-region. 32

3.4 Results of SAMI2 simulations using measured drifts (left hand side panels) and climatological (SF99) model drifts (right hand side) for June 4-5, 2008. Top panels: Equatorial vertical plasma drifts used as input. Middle panels: Local electron density over Jicamarca. Bottom panels: Flux-tube integrated linear growth rates for GRT instability. 33

3.5 Same as Figure 3.4 but driving SAMI2 with *Scherliess and Fejer* (1999)(SF99) model drifts for December 21, 2008 (left side panels) and March 21, 2008 (right side panels). Note that the growth rate color scale for March equinox is different from the other cases. 36

3.6 HWM93 meridional winds (around 200 km altitude) used in SAMI2 simulations for June 4-5, 2008. The dashed line indicates the latitude of Jicamarca (11.95° S). 38

3.7 Meridional wind patterns (poleward and equatorward) used in the numerical experiments. The blue marker indicates the latitude of Jicamarca (11.95° S). . . . 39

3.8 Linear growth rate results for June 4-5, 2008 using climatological (HWM93) meridional winds and weakening downward drifts. Top left: ratio of integrated Pedersen conductivity. Top right: integrated electron density gradient (Top-right). Bottom left: $\frac{g_e}{v_{eff}}$. Bottom right: Linear growth rate. 40

3.9 Linear growth rate results for June 4-5, 2008 using diverging (poleward) meridional winds and weakening downward drifts. Top left: ratio of integrated Pedersen conductivity. Top right: integrated electron density gradient (Top-right). Bottom left: $\frac{g_e}{v_{eff}}$. Bottom right: Linear growth rate. 41

3.10 Linear growth rate results for June 4-5, 2008 using converging (equatorward) meridional winds and weakening downward drifts. Top left: ratio of integrated Pedersen conductivity. Top right: integrated electron density gradient (Top-right). Bottom left: $\frac{g_e}{v_{eff}}$. Bottom right: Linear growth rate. 42

3.11 Linear growth rate results for June 4-5, 2008 using converging (equatorward) meridional winds and climatological (*Scherliess and Fejer*, 1999) equatorial drifts. Top left: ratio of integrated Pedersen conductivity. Top right: integrated electron density gradient (Top-right). Bottom left: $\frac{g_e}{v_{eff}}$. Bottom right: Linear growth rate. 43

4.1 The top panel shows an example of the Range-Time-Intensity map of echoes measured by JULIA on March 2, 2000. The bottom panel shows the regions were ESF irregularities were identified based on number of echoes above a certain SNR threshold. Please, see text for more details. 50

4.2 Variation of the solar flux index (F10.7) during the period under which JULIA measurements were made. 51

4.3 Occurrence rates of quiet-time equatorial spread F observed by JULIA between 1996 and 2015. Only seasons with at least 10 days of observations are shown. The bottom panel shows the variation of the average F10.7 index for each year. Curves show the four different seasons: March Equinox, June Solstice, September Equinox, and December Solstice. The top panels show height versus local time maps of the seasonal occurrence rates of ESF for each year. 53

4.4 Examples of JULIA RTI maps for June solstice 2009. Each panel also shows the variation of h'F (red markers) and hmF2 (green markers) measured by a collocated digisonde. 54

4.5 Examples of JULIA RTI maps for December solstice 2009. Each panel also shows the variation of h'F (red markers) and hmF2 (green markers) measured by a collocated digisonde. 57

5.1 Map of South America showing the location of the São Luís site where the MELISSA radar system is located. The location of the Jicamarca Radio Observatory is also shown for reference. 65

5.2 Range-Time-Intensity (RTI) showing an example of F-region observations made by MELISSA on March 22, 2014. The RTI map shows that F-region irregularities were not detected in the early nighttime hours (00:00-08:00 LT) but were observed in the post-sunset hours (18:00 - 24:00 LT). 66

5.3 The panels on the left hand side show examples of RTI maps of post-sunset ESF events observed by MELISSA during December Solstice 2015. The panels on right hand side show the post-midnight events observed by MELISSA. 68

5.4 Example of spectral analysis of premidnight F-region echoes 71

5.5 Example of spectral analysis of Near midnight F-region irregularities 74

5.6 Example 1 of spectral analysis of strong post-midnight F-region echoes 76

5.7 Example 2 of spectral analysis of strong post-midnight F-region echoes 77

5.8 Example of spectral analysis of weak post-midnight F-region echoes 78

5.9 The local time variation of h'F and hmF2 for the ESF events discussed in this study 79

5.10 RTI maps of the post-midnight events examined in this study 82

A.1 Climatology of the equatorial vertical drifts estimated from the Jicamarca incoherent incoherent scatter radar measurements (thick line). The error bars represent the variability of the drifts used in the averages. Predictions of the *Scherliess and Fejer* (1999) model (think solid line) are also shown for each season and solar flux condition. 89

A.2 Equatorial vertical plasma drifts simulated by the WACCM-X model for 30 days (gray line curves) around each season (Mar. 21, Jun. 21, Sep. 21, and Dec. 21) and their average (red curves). The curve is the SF99 model prediction for each season. 94

A.3 Synthetic vertical plasma drifts created using SF99 climatological predictions (blue curves) and WACCM-X drift variabilities for 30 days (gray line curves) around each season (Mar. 21, Jun. 21, Sep. 21, and Dec. 21). 97

A.4 Results of the linear growth rate estimates for March Equinox. The growth rates were estimated from SAMI2 outputs driven by the synthetic drift curves (Figure A.3). 100

A.5 Results of the linear growth rate estimates for June Solstice. The growth rates were estimated from SAMI2 outputs driven by the synthetic drift curves (Figure A.3). 101

A.6 Results of the linear growth rate estimates for September Equinox. The growth rates were estimated from SAMI2 outputs driven by the synthetic drift curves (Figure A.3). 102

A.7 Results of the linear growth rate estimates for December Solstice. The growth rates were estimated from SAMI2 outputs driven by the synthetic drift curves (Figure A.3). 103

A.8 Results of the linear growth rate estimates for March Equinox. The growth rates were estimated from SAMI2 outputs driven by WACCM-X drift curves (Figure A.2). 104

A.9 Results of the linear growth rate estimates for June Solstice. The growth rates were estimated from SAMI2 outputs driven by WACCM-X drift curves (Figure A.2). 105

A.10 Results of the linear growth rate estimates for September Equinox. The growth rates were estimated from SAMI2 outputs driven by WACCM-X drift curves (Figure A.2). 106

A.11 Results of the linear growth rate estimates for December Solstice. The growth rates were estimated from SAMI2 outputs driven by WACCM-X drift curves (Figure A.2). 107

LIST OF TABLES

5.1 Radar parameters for the F-region observation mode used by MELISSA. 66

5.2 Summary of the F-region observations made by MELISSA between 2014 and 2018. The observations are grouped into seasons. Each season is sub-divided into PRE- and POST-midnight observations. The first value in each group indicates the total number of observations, while the value in parentheses indicates the number of observations where echoes were identified. Finally, N/A indicates that observations were not available. 69

CHAPTER 1

INTRODUCTION

The main goal of this dissertation is to advance our understanding of the ionospheric phenomenon known as equatorial spread F (ESF). ESF is the name given, for historical reasons, to the manifestation of electron density irregularities in the low-latitude ionosphere. It was first observed as diffuse radio echoes from the ionosphere in the equatorial region (*Booker and Wells*, 1938). In addition to its scientific importance, the study of ESF has been motivated by its impact on radio signals used in different types of applications (communications, remote sensing, navigation, etc.). ESF morphology and occurrence rates vary with local time, season, longitude, solar flux, and geomagnetic activity. Additionally, ESF also has a high day-to-day variability.

In this chapter, we give a brief introduction to the Earth's low-latitude ionosphere and ESF before providing more details about main goals and results of this dissertation.

1.1 The low-latitude ionosphere

The ionosphere is an ionized region of the upper atmosphere, located between about 60 and 1000 km altitude. Photo-ionization of neutral molecules by solar radiation in extreme ultraviolet (EUV) and X-ray parts is the main source of ionospheric production at middle and low latitudes (*Hargreaves*, 1992; *Schunk and Nagy*, 2001). The ionospheric electron density profile exhibits a layered structure, with distinct regions referred to as D, E, F_1, and F_2 as shown in Figure 1.1.

Figure 1.1 also shows that, at night, the D and F_1 regions vanish and the E region becomes much weaker. The F_2 region remains with reduced electron density. Figure 1.1 also shows that solar flux conditions significantly affect the ionospheric profiles. Ionospheric densities are much higher during periods of maximum sunspot (high solar activity) than during periods of minimum sunspot (low solar activity).

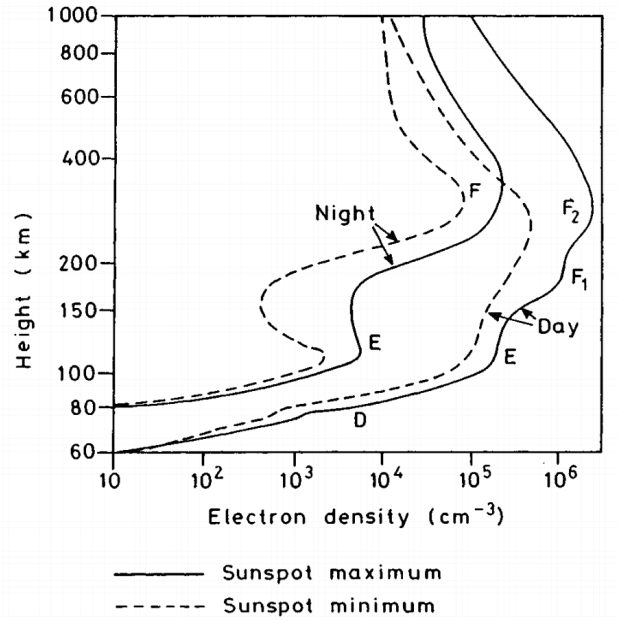

Figure 1.1. Typical vertical profiles of electron density in the mid-latitude ionosphere. From *Hargreaves* (1992)

.

1.2 Ionospheric $\mathbf{E} \times \mathbf{B}$ drifts

The behavior of the low latitude ionospheric plasma and the phenomena to be studied are strongly controlled by background electric fields. These ionospheric electric fields are generated to maintain ionospheric currents divergence-free. The ionospheric currents are mainly produced by the dynamo action of thermospheric neutral winds with contributions from plasma pressure gradients and gravity.

In this section, we review the formulation that describes the motion of ions and electrons under the action of external forces. We review, in particular, the F-region plasma motion accompanying the background electric field, which is commonly referred to as $\mathbf{E} \times \mathbf{B}$ drift.

Starting with the momentum equation for a weakly ionized, single-ion, magnetized plasma, under the action of force $\mathbf{F}$, the velocity component parallel and perpendicular to the magnetic field of charged particles can be written, respectively, as (*Heelis*, 2004):

$$\mathbf{V}_{\alpha\parallel} = \frac{1}{M_\alpha \nu_\alpha} F_{\alpha\parallel} + \mathbf{U}_\parallel \tag{1.1}$$

and

$$\mathbf{V}_{\alpha\perp} = \frac{1}{M_\alpha \nu_\alpha} \frac{1}{1 + (\frac{\Omega_\alpha}{\nu_\alpha})^2} \left[\mathbf{F}_{\alpha\perp} + \frac{\Omega_\alpha}{\nu_\alpha} \mathbf{F}_{\alpha\perp} \times \hat{\mathbf{b}} \right] + \mathbf{U}_\perp \tag{1.2}$$

where α represents ions or electrons, $\parallel$ and $\perp$ indicate the directions parallel and perpendicular to the magnetic field, respectively, $\hat{\mathbf{b}}$ is the unit vector along field line ($\hat{\mathbf{b}} = \mathbf{B}/B$), M_α is mass, ν_α is the collision frequency between ions or electrons with neutral species, and Ω_α is gyro-frequency. Finally, $\mathbf{U}$ is the neutral wind vector velocity.

The forces ($\mathbf{F}$) acting on the plasma can be described by:

$$\mathbf{F} = -\frac{1}{N_\alpha} \nabla (N_\alpha k T_\alpha) + M_\alpha \mathbf{g} + q_\alpha (\mathbf{E} + \mathbf{U} \times \mathbf{B}) \tag{1.3}$$

where N_α is the charge density, k is Boltzmann's constant, T_α is the plasma temperature, $\mathbf{g}$ is the gravitational acceleration, q_α is the electric charge of the particle in question (electrons or ions), and $\mathbf{E}$ is the external electric field.

Figure 1.2 summarizes the behavior of ion and electron velocities at different ionospheric regions driven by the action of neutral winds (top) and electric fields (bottom). Changes in the velocity behavior are controlled by changes in the ratio of gyro-to-collision frequencies ($\frac{\Omega_\alpha}{\nu_\alpha}$). For instance, at F-region heights where collision frequencies are small compared to gyro-frequencies, ions and electrons in the presence of a background electric field tend to move in the $\mathbf{E} \times \mathbf{B}$ direction. Therefore, at magnetic equatorial F-region heights an electric field pointing in the upward direction is associated with ionospheric plasma motion in the zonal (magnetic east) direction. Similarly, an electric field pointing in the zonal (eastward) direction is associated with ionospheric plasma motion in the upward direction.

The development of ESF, the main subject of this dissertation, is often associated with the behavior of vertical $\mathbf{E} \times \mathbf{B}$ drifts (*Fejer et al.*, 1999). Prior to providing more information

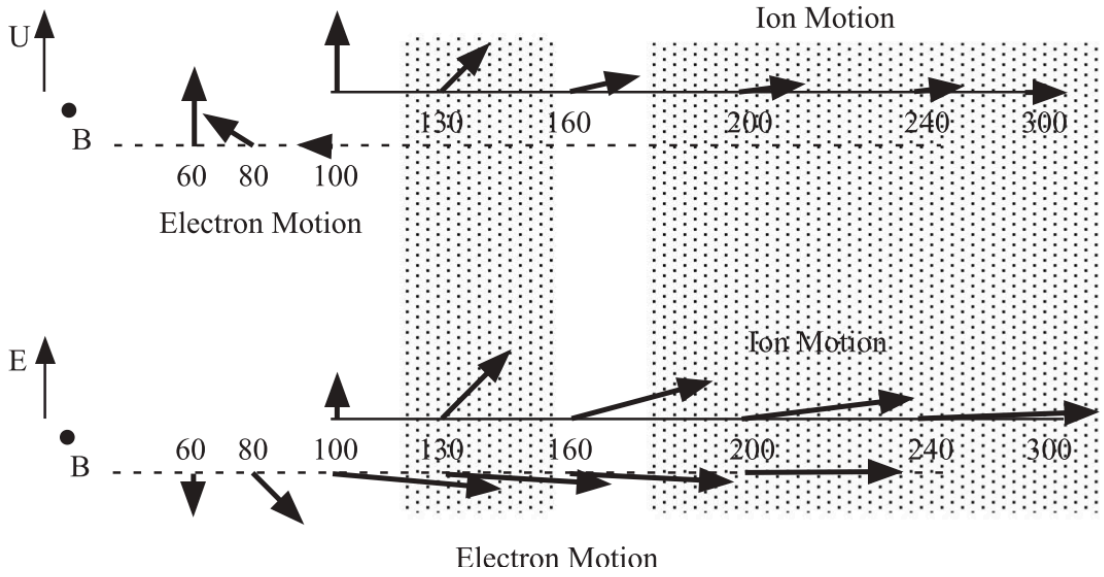

Figure 1.2. Relative magnitude and direction of ion and electron velocities produced by the direct action of neutral winds and electric fields. Approximate locations of the E- and F-regions are shaded (*Heelis*, 2004).

about the relationship between vertical drifts and ESF, we describe the main features related to the $\mathbf{E} \times \mathbf{B}$ plasma drift patterns that are observed near the magnetic equator.

Figure 1.3 shows climatological curves of F-region vertical $\mathbf{E} \times \mathbf{B}$ plasma drifts measured at the Jicamarca Radio Observatory (JRO) using the incoherent scatter radar technique. The curves represent averaged measurements made under different solar flux conditions and seasons. They show that, in general, the drifts are upward during the day and downward at night. The curves also show an enhancement of the vertical drifts around sunset hours that will be discussed later in this chapter.

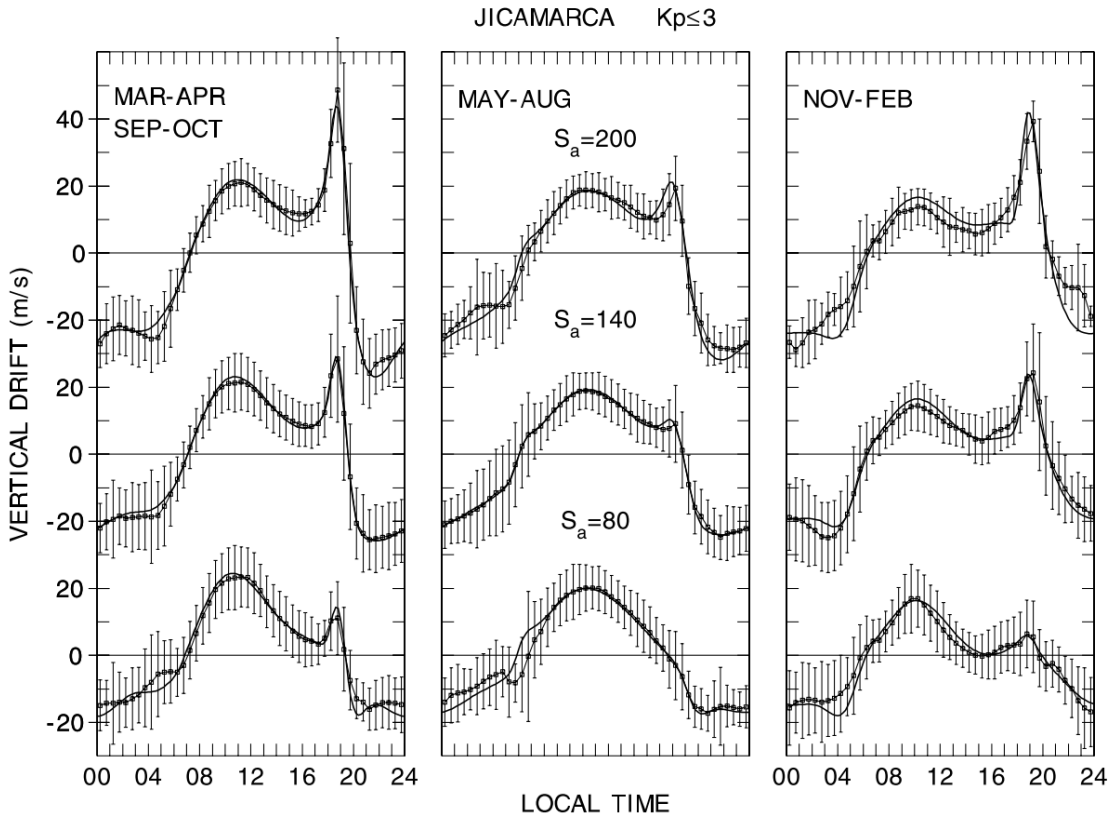

Figure 1.3. The markers and thick lines show averaged vertical $\mathbf{E} \times \mathbf{B}$ drifts measured at the Jicamarca Radio Observatory near the magnetic equator. The error bars represent the variability of the drift measurements used in the averages. The thin lines show predictions of a climatological model. Columns from left to right correspond to equinox, June solstice and December solstice, respectively. Rows from top to bottom correspond to high, moderate and low solar flux conditions, respectively. From *Scherliess and Fejer* (1999).

.

1.3 Ionospheric conductivities and currents

Equatorial ionospheric electric fields are produced, in most part, by the dynamo action of neutral winds at thermospheric heights (above 100 km altitude). At E-region heights, neutral winds usually refer to tides propagated from lower atmosphere. Among these tides, semidiurnal and diurnal tides dominate. At F-region heights, neutral winds are mainly driven by pressure gradients caused by *in situ* solar EUV heating (*Hargreaves*, 1992; *Kelley*,

2009). F-region winds are usually modified by ion drag and sometimes by tides propagated from lower atmosphere.

Taking into consideration the motion of ions and electrons due to the action of neutral winds and electric fields, the electric current density at ionospheric heights can be written as (*Richmond*, 1989):

$$\mathbf{J} = \sigma_0 \mathbf{E}_{\parallel} + \sigma_P(\mathbf{E}_{\perp} + \mathbf{U} \times \mathbf{B}) - \sigma_H(\mathbf{E}_{\perp} + \mathbf{U} \times \mathbf{B}) \times \hat{\mathbf{b}} \tag{1.4}$$

where σ_P, σ_H, and σ_0 are the Pedersen, Hall and direct conductivities, respectively. The subscripts $\parallel$ and $\perp$ indicate components parallel and perpendicular to $\mathbf{B}$, respectively. Here, σ_P, σ_H, and σ_0 are as follows (*Heelis*, 2004):

$$\sigma_P = Ne^2\left[\frac{1}{m_e}\frac{\nu_e}{\nu_e^2+\Omega_e^2} + \frac{1}{m_i}\frac{\nu_i}{\nu_i^2+\Omega_i^2}\right] \approx \frac{Ne^2}{m_i}\frac{\nu_i}{\nu_i^2+\Omega_i^2}, \tag{1.5}$$

$$\sigma_H = Ne^2\left[\frac{1}{m_e}\frac{\Omega_e}{\nu_e^2+\Omega_e^2} - \frac{1}{m_i}\frac{\Omega_i}{\nu_i^2+\Omega_i^2}\right] \tag{1.6}$$

$$\sigma_0 = \frac{Ne^2}{m_e\nu_e} + \frac{Ne^2}{m_i\nu_i} \tag{1.7}$$

As an illustration, Figure 1.4 shows plots of typical vertical variations of σ_0, σ_P and σ_H for a location near the magnetic equator (Jicamarca) during nighttime (0000 LT) and daytime (1200 LT) conditions. The most striking feature in this plot is that σ_0 is several orders of magnitude larger than σ_P and σ_H at all heights. Figure 1.4 also shows that the Hall conductivity has a peak around 110 km and quickly decreases with height. The Pedersen conductivity also has a peak at E-region heights, but decreases less quickly than the Hall conductivity. Finally, both Hall and Pedersen conductivities reduce dramatically at night. Significant Pedersen conductivity, however, remains at F-region heights ($\sim$300 km).

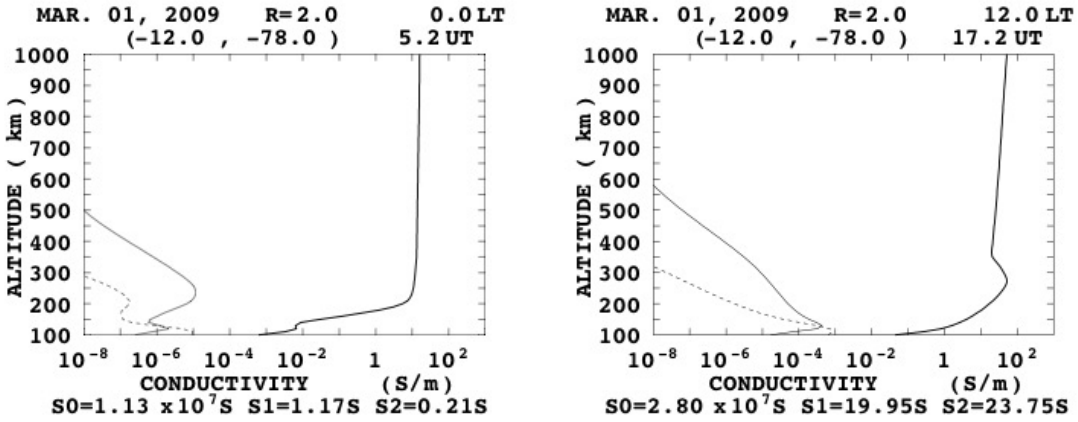

Figure 1.4. Typical height profiles of the ionospheric conductivities for nighttime (left) and daytime (right) conditions. Produced by the ionospheric conductivity model at the World Data Center for Geomagnetism, Kyoto (`http://wdc.kugi.kyoto-u.ac.jp/ionocond/sightcal/index.html`). The dark solid line, light solid line and dashed line indicate parallel, Pedersen and Hall conductivities, respectively.

1.4 Thermospheric winds and vertical drifts

We now return our attention to thermospheric winds and their role in creating low-latitude plasma motion. Figure 1.5 shows an idealized pattern of the horizontal component of neutral winds at E-region heights as a function of latitude and local time. In the E-region, both Hall and Pedersen conductivities are important and need to be considered to understand current flow and the resulting plasma motion.

Figure 1.5 shows that, around 1200 LT, the direction of the wind is mostly poleward with magnitude increasing with latitude. Below about 20° latitude, this wind causes zonal (westward) Pedersen currents. Due to day/night gradients in ionospheric F-region electron density and conductivities, an accumulation of positive (negative) charges around sunrise (sunset) is observed. That configuration of charges produces a polarization electric field that is directed to the east during the day, and to the west at night. These polarization electric drifts are associated with the overall pattern of upward drifts during daytime hours and downward drifts during nighttime hours seen in Figure 1.3.

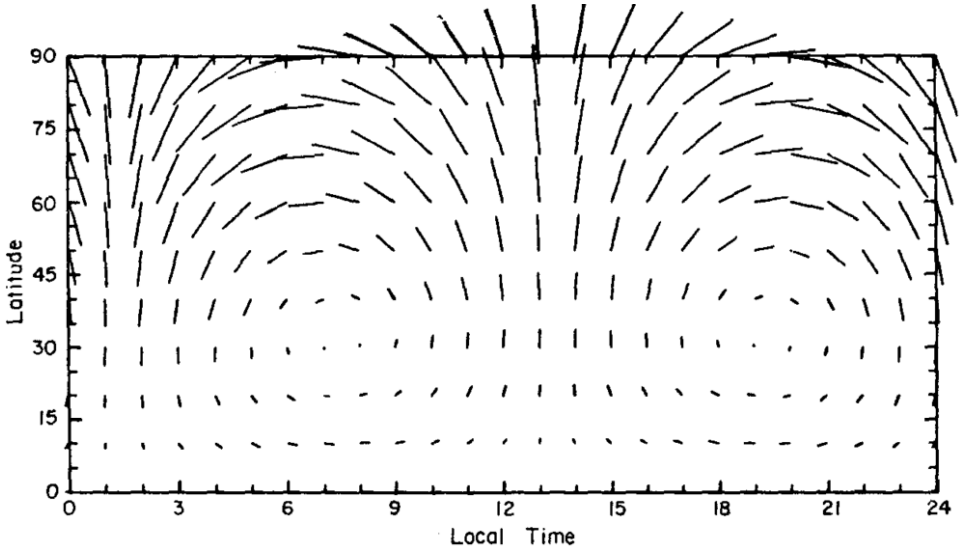

Figure 1.5. Prototypical wind pattern in the E-region as a function of latitude and local time for the northern hemisphere (*Tarpley*, 1970).

1.5 The pre-reversal enhancement (PRE)

In addition to the diurnal variation of the drifts, Figure 1.3 also shows an enhancement of the vertical drifts prior to its reversal around sunset hours in all seasons, except in June solstice during solar minimum conditions. This feature is called the pre-reversal enhancement (PRE) of vertical the plasma drifts or zonal electric fields.

The origin of the PRE is explained taking into consideration the role of neutral winds at F-region heights. Here, we present the mechanism proposed by *Farley et al.* (1986). But we must point out that there are two other explanations for the PRE (see for instance, *Rishbeth* (1971); *Haerendel and Eccles* (1992)).

In the explanation formulated by *Farley et al.* (1986), the zonal component of equatorial thermospheric winds at F-region heights around sunset is assumed to be in the eastward direction (*Kelley*, 2009). It is also considered that the Pedersen conductivity, around sunset, is mostly confined to a slab around F-region heights. Therefore, the eastward wind will drive an upward Pedersen current with a divergence that has a corresponding downward

polarization electric field (E_z) at the magnetic equator as illustrated in Figure 1.6. This electric field will be mapped along the magnetic field to the off-equator E-region. There, this electric field field is consistent with a Hall current at the dusk terminator ($J_{\theta\phi}$). Because of the day/night conductivity gradients, a negative charge is created near the terminator, which drives an eastward electric field (E_ϕ) in the dayside. This electric field maps back to the equatorial F-region where it contributes to the PRE.

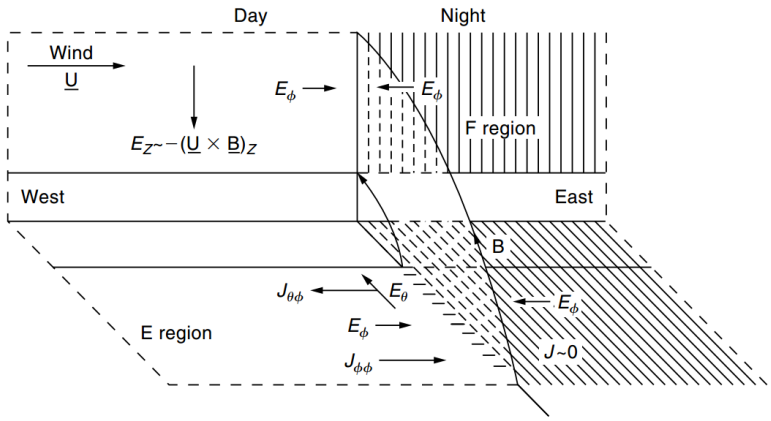

Figure 1.6. A schematic diagram of PRE (*Farley et al.*, 1986).

1.6 The Generalized Rayleigh-Taylor instability and ESF

Now that we have an overall view of the general behavior of the electric fields and plasma drifts at low latitudes, we move on to providing more details about equatorial spread F (ESF).

As mentioned earlier, ESF is the name given to the manifestation of electron density irregularities in the low-latitude ionosphere. *Dungey* (1956) first proposed that a gravitational instability developing in the bottomside of the F-region could explain the generation of ESF irregularities. Then, *Woodman and La Hoz* (1976) expanded this idea explaining that bottomside disturbances could penetrate into the topside ionosphere through a non-linear

process, which would be similar to what is observed during Rayleigh-Taylor (RT) instability in neutral fluids.

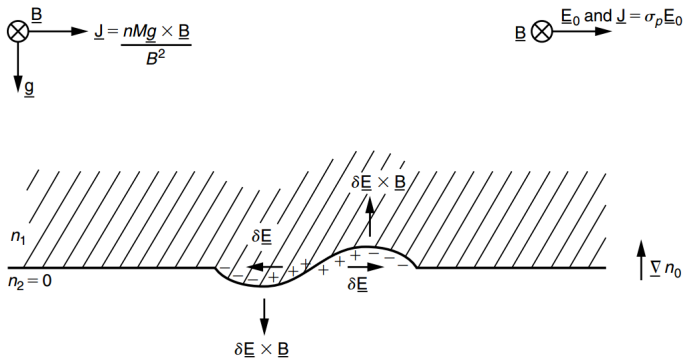

Figure 1.7. A schematic representation of the Rayleigh-Taylor instability in the equatorial ionosphere. From *Kelley* (2009).

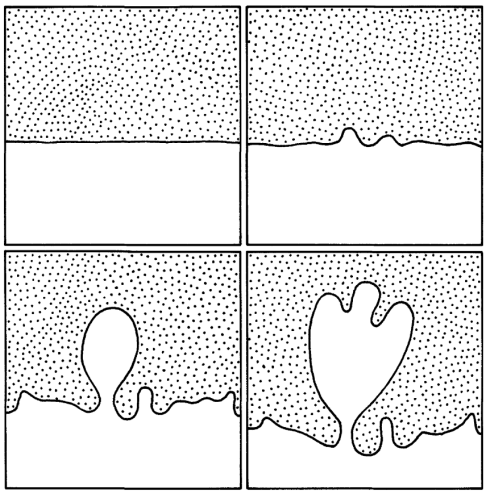

Figure 1.8. Sequential sketches made from photos of the hydrodynamic Rayleigh-Taylor instability. A heavy fluid is initially supported by a transparent lighter fluid. From *Kelley* (2009).

Figure 1.7 illustrates a plasma configuration in which the ionospheric RT instability would find favorable growth conditions. It shows a slab of plasma (with density n_1) above a region devoid of plasma ($n_2 = 0$). In this configuration, gravity is downward, an external magnetic field is into the page, a background electric field (E_0) is to the right, and the plasma

gradient (∇n_0) is upward. Gravity and the background electric field drive a current density to the right as indicated in the Figure. This configuration resembles the ionospheric plasma configuration seen near the magnetic equator around sunset hours.

Figure 1.7 also shows that if a small density disturbance is observed in the interface between n_1 and n_2 the current will produce charge accumulations and polarization electric fields $\delta\mathbf{E}$. This polarization electric field is such that it causes the region devoid of plasma to enter the region with plasma. With time, the plasma density disturbance grows larger as illustrated in Figure 1.8.

When we take into account the presence of zonal electric fields (E), gravity (g), and neutral winds with components in the zonal ($\mathbf{U}_z$) and vertical ($\mathbf{U}_v$) directions on a region of plasma with vertical gradient scale height (L) then a more complete expression for the local linear growth rate (γ) can be obtained for the ionospheric plasma RT instability (*Kelley*, 2009):

$$\gamma = \frac{1}{L}\left(\frac{E}{B} + \frac{g}{\nu_{in}} - U_v + \frac{\nu_{in}}{\Omega_i}U_z\right) \tag{1.8}$$

where $L = \left(\frac{1}{N_0}\frac{\partial N}{\partial h}\right)^{-1}$, h is height, and ν_{in} is the ion-neutral collision frequency.

1.7 Typical, post-sunset ESF

Equation 1.8 can explain most of the observed features in typical ESF events. ESF is often observed after sunset during equinoctial months in most longitude sectors. This is because the growth rate finds favorable conditions during those periods. Around sunset the PRE contributes substantially to the the E/B term. The vertical drifts associated with the PRE also lift the equatorial ionosphere to higher altitudes where ν_{in} is substantially decreased, and g/ν_{in} therefore increases. Additionally, during sunset, large vertical density gradients

(small L) in the bottomside F-region are observed as a result of the fast recombination of molecular ions contributing to an increase in the linear growth rate.

While Equation 1.8 can explain the main features in ESF, it is now well recognized that the linear stability is not determined by local plasma parameters only, but by the environment along a magnetic field line. *Sultan* (1996) derived an expression for the linear growth rate of the ionospheric (Generalized) RT instability that takes into consideration the variation of ionospheric and thermospheric parameters along magnetic field lines. The growth rate is given by:

$$\gamma = \frac{\Sigma_P^F}{\Sigma_P^E + \Sigma_P^F}(V_p - U_L^p + \frac{g_e}{\nu_{eff}})K^F - R \tag{1.9}$$

where Σ_P^E and Σ_P^F are flux-tube integrated E- and F-region Pedersen conductivities, respectively. V_p is the equatorial vertical drift velocity (the same as $\frac{E}{B}$). U_L is the flux-tube integrated neutral wind component perpendicular to the magnetic field and weighted by the Pedersen conductivity. g_e is the local gravitational acceleration defined as $\frac{g_0}{L^2}$ (where g_0 is the gravitational acceleration on the equatorial surface of earth, and L is the distance from the center of the Earth in Earth radii). ν_{eff} is the flux-tube integrated effective F-region ion-neutral collision frequency. K^F is defined by $\frac{1}{N_e}\frac{\partial N_e}{\partial h}$ (where N_e is the flux-tube integrated electron density, and h is the height in equatorial plane). The recombination term R can be neglected since it is only important locally in the E region (*Sultan*, 1996).

Equation 1.9 allows us to evaluate the linear stability of the low-latitude ionosphere under different thermospheric and ionospheric conditions, and it will be used in the investigations that are part of this dissertation.

1.8 On radar observations of ESF

ESF is related to low-latitude F-region density irregularities with scale sizes ranging from centimeters to hundreds of kilometers (e.g. *Hysell*, 2000; *Woodman*, 2009). Ground-based radars are often used to remotely sense ionospheric irregularities associated with ESF. These radars measure the scattering of radio waves caused by ionospheric plasma waves. In general, meter-scale plasma waves cause Bragg scattering of radio waves. Field-aligned irregularities, in particular, cause strong, coherent radar echoes that can be detected by relatively small, low power (coherent) backscatter radars. Based on radar measurements, ESF irregularities start to appear at the bottom-side of the equatorial F-region, develop vertically and reach the topside ionosphere. Radar observations also show that ESF can occur as high as 1,500 km altitude (e.g. *Farley et al.*, 1970).

Based on range-time-intensity (RTI) maps, which describe the height-vs-time evolution of backscattered echoes from the ionospheric irregularities, Woodman and La Hoz (1976) divided ESF into three types: bottom-type, bottom-side and topside ESF. Bottom-type ESF is associated with a narrow (a few 10s of km in height) echoing layer that appears in the bottomside F-region with a relatively long duration (1-to-2 hours) around the time of the PRE. Bottomside ESF is associated with a layer of echoes in the RTI maps that also appear at bottomside F-region heights. The bottomside echoes, however, are stronger and more structure than the echoes associated with bottom-type echoing layers. Topside ESF is associated with echoing layers that reach the topside ionosphere, and with ESF plasma depletion events observed by satellites.

Figure 1.9 shows examples of radar observations of typical, post-sunset ESF events. It shows, from a to c, examples of RTI maps that indicate the occurrence of bottom-type, bottomside and topside echoes observed by the 50 MHz radar system (JULIA) of the Jicamarca Radio Observatory, in Peru. Figure 1.9 also shows an example of an atypical ESF event (d), that was observed after midnight hours.

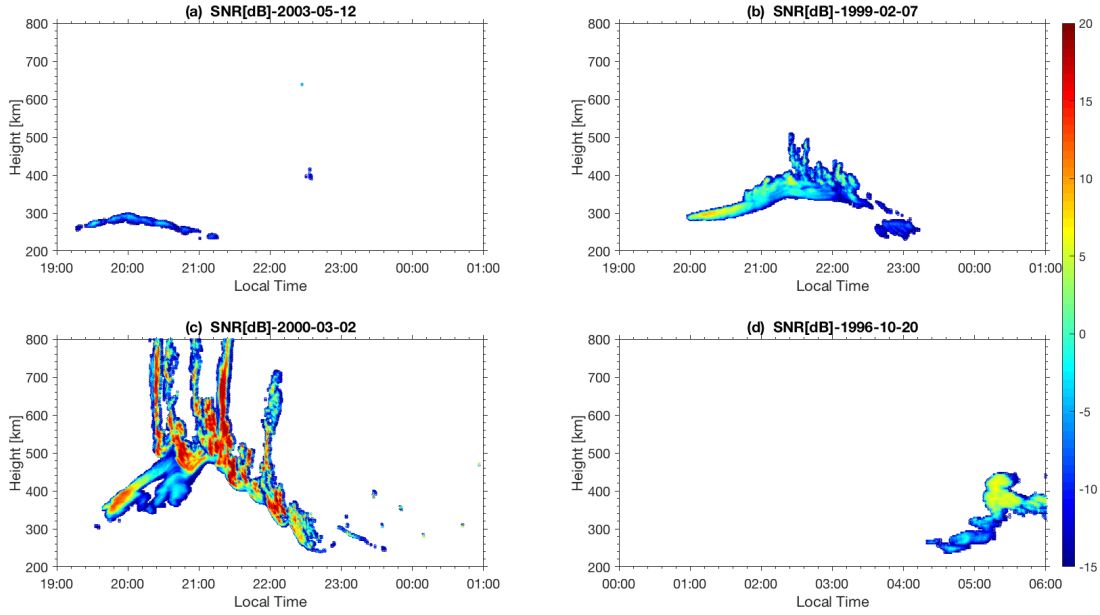

Figure 1.9. Range-Time-Intensity (RTI) maps showing examples of post-sunset (a) bottom-type, (b) bottomside, (c) topside, and (d) post-midnight ESF radar events. These measurements were made by the JULIA radar system of the Jicamarca Radio Observatory.

In the investigation, we will use radar observations of ESF, combined with numerical modeling and observations of background ionospheric conditions to advance our understanding of atypical, post-midnight ESF events. In the next chapter, we describe three specific science questions which will be addressed as part of the work. The efforts and results towards science questions 1, 2 and 3 are presented in chapters 3, 4 and 5, respectively. Additionally, preliminary results related to potential future work are presented in Appendix A.

CHAPTER 2

MOTIVATION AND SCIENCE QUESTIONS

A large number of efforts have been dedicated to studies of post-sunset (pre-midnight) equatorial spread F (ESF) events (e.g *Woodman and La Hoz*, 1976; *Abdu et al.*, 1981; *Hysell and Burcham*, 1998; *Fejer et al.*, 1999; *Woodman*, 2009; *Aveiro and Hysell*, 2010), which led to a significant improvement of our understanding of this phenomenon.

In the past two decades, however, more attention has been devoted to ESF events observed in the post-midnight sector (*MacDougall et al.*, 1998; *Sastri*, 1999; *Niranjan et al.*, 2003; *Patra et al.*, 2009; *Gentile et al.*, 2011; *Li et al.*, 2011; *Stoneback et al.*, 2011; *Nishioka et al.*, 2012; *Otsuka et al.*, 2012; *Yokoyama et al.*, 2011; *Ajith et al.*, 2016; *Dao et al.*, 2017; *Smith and Heelis*, 2017, 2018a,b). These post-midnight ESF events are intriguing because the primary driver of post-sunset ESF, enhanced upward plasma drifts, is not believed to occur in the post-midnight sector under geomagnetically quiet conditions.

As explained in Chapter 1, the GRT instability driven, in the most part, by the PRE can explain the high occurrence rate of post-sunset ESF and most of the observed variations in longitude and season. However, a secondary peak in the occurrence rate of ESF events observed after midnight during June solstice of solar minimum conditions (*Patra et al.*, 2009; *Heelis et al.*, 2010; *Li et al.*, 2011; *Yokoyama et al.*, 2011; *Otsuka et al.*, 2012) has yet to be better understood. During post-midnight hours, equatorial vertical plasma drifts are expected to be downward according to climatological drift models (*Fejer et al.*, 1999) and, therefore, other destabilizing factors should be considered.

In this chapter, we review some of the main findings related to post-midnight ESF events that have been reported by previous studies, and provide specific science questions to be addressed as part of this dissertation work.

2.1 Background and Motivation

The detection of ESF events at a given longitude sector during post-midnight hours could be attributed to two distinct scenarios: First, they could be the result of an instability process that produced "fresh" irregularities in the midnight/post-midnight sector. Second, they could be the result of irregularities which were generated in the post-sunset sector, but to the west of the observing location, and drifted eastward with the bulk plasma motion and across the field-of-view of the observations.

About 20 years ago, *MacDougall et al.* (1998) emphasized that only a few studies of post-midnight (pre-sunrise) ESF events existed. Motivated by the lack of these studies, they analyzed measurements made by a vertical radio sounder (ionosonde). The observations were made between November 1994 and October 1995 in Fortaleza, Brazil near the magnetic equator. The most striking result of their study was the high occurrence rate of ESF during post-midnight hours around June and December solstices. Using interferometric observations, they also pointed out the occurrence of irregularity patches, which were correlated with ionospheric height variations and vertical velocity variations. *MacDougall et al.* (1998) suggested that Rayleigh-Taylor instability could be associated with bottomside bulges of the ionosphere caused by a gradient-drift instability and then produced spread F.

Sastri (1999) used ionosonde observations made at a station near the magnetic equator in the Indian sector (Kodaikanal, 4°N dip lat) to determine and study the occurrence of post-midnight ESF. Only observations made during June solstice (1994 and 1995) were analyzed. They pointed out that an increase in virtual height of the F-region base (h'F) preceded the occurrence of post-midnight ESF in most cases, but that the increase did not produce sufficient conditions for ESF appearance. They pointed out that the lack of ESF, despite h'F increases, could be due to the inhibiting action of neutral winds and the lack of seed waves capable of triggering the instability.

Additional information about ESF can be obtained from observations made by ionospheric radar systems. In fact, a significant amount of understanding about ESF comes from coherent and incoherent scatter radar observations at the Jicamarca Radio Observatory in Peru.

The upgrade or deployment of new coherent radar systems in the past 20 years or so at various sites led to new studies of post-sunset and post-midnight ESF at various longitude sectors. For instance, radar observations made in Gadanki, India (13.5°N, 79.2°E, 6.4° N dip lat) showed the occurrence of post-midnight ESF during all 20 nights of observations made during June solstice of low-solar flux conditions. They reported that while the intensity of the post-midnight ESF echoes were comparable to those of equinoctial, pre-midnight decaying ESF irregularities, the velocity pattern of the observed structures, however, was distinct. The upward velocity pattern indicated that post-midnight ESF events could have been generated after midnight. *Otsuka et al.* (2012) also reported results of new observations made by a VHF (30.8 MHz) radar system deployed in the low-latitude site of Kototabang, Indonesia (0.20°S, 100.32°E; 10.4°S dip lat). Analyses of observations made from February 2006 to December 2010 showed the occurrence of post-midnight ESF between May and August every year. Average velocity of the zonal propagation of these post-midnight ESF irregularities was about 50 m/s westward.

The implementation of the Jicamarca Unattended Long-term Investigations of the ionosphere and Atmosphere (JULIA) mode of the Jicamarca radar, allowed semi-continuous observations of ESF in the American sector starting in 1996 (*Hysell and Burcham*, 1998). *Hysell and Burcham* (2002) used JULIA observations made between August 1996 and April 2000 to investigate the morphology (in height and local time) of ESF events. Their focus, however, was on the variability of post-sunset ESF. Limitations in the number of observations at the time restricted their analyses to equinox and December solstice and to a limited range of solar flux conditions. They did, however, pointed out that geomagnetic activity in-

creases the occurrence of post-midnight ESF through disturbance electric fields particularly during solar minimum conditions.

More recently, *Ajith et al.* (2015) used the East-West scanning capability of the Equatorial Atmosphere Radar - EAR (0.2°S, 100.3°E, 10.1°S dip lat) to study ESF events. The scanning capability allowed them to determine events that were generated locally ("fresh" ESF events). They analyzed measurements made during moderate solar flux conditions (2011 – 2012), and found that fresh ESF events were confined to post sunset hours (1900–2100 LT) during equinoxes. During June solstice, however, the majority of fresh ESF events occurred around midnight hours (2200–0300 LT).

Then a further statistical study made by *Ajith et al.* (2015) showed a secondary maximum of occurrence rates of evolving-type ESF, which was defined as ESF events that are originated within the field-of-view (FOV) of Equatorial Atmospheric Radar (EAR) in Indonesia and found to grow successively, and this type of ESF is dominant during postmidnight in June solstice.

While ionosonde and radar measurements can provide long-term observations of ESF at a given location, sensors on satellites can provide information about ESF occurrence over the globe for different seasons and solar flux conditions (*Huang et al.*, 2002; *Gentile et al.*, 2006; *Xiong et al.*, 2010). The low-inclination orbit C/NOFS satellite, for instance, found high occurrence rates of post-midnight ESF during the 2008-2009 extended solar minimum (*de La Beaujardiere et al.*, 2009; *Burke et al.*, 2009; *Heelis et al.*, 2010; *Huang et al.*, 2011; *Yizengaw et al.*, 2013; *Huang et al.*, 2014).

Some of these studies suggested that quiet-time upward plasma drifts (eastward electric field) could have been the main factor responsible for the generation of post-midnight ESF (*de La Beaujardiere et al.*, 2009; *Yizengaw et al.*, 2013). *Stoneback et al.* (2011), for instance, reported that upward drifts were observed by C/NOFS sensors near midnight and they are strongest in solstice seasons. They hypothesized that these abnormal drifts could have been

the result of enhanced semi-diurnal tides. They also reported that the upward drifts at night are associated with regions with high occurrence rates of postmidnight ESF during December 2008 and June 2009 solstices.

It has also been suggested that post-midnight ESF events could occur without enhanced upward drifts (*Nicolls et al.*, 2006). In that case, other factors such as the apparent uplift of the F-region around midnight, combined with a decrease in ion-neutral collision frequency could lead to an enhanced linear growth rate (see Equation 1.9) and ESF development. Additionally, *Huba et al.* (2013) suggested that equatorward neutral winds could destabilize the evening F-region. This wind pattern could also destabilize the F-region near midnight, and contribute to ESF generation even under weak plasma drift conditions (*Ajith et al.*, 2016).

The overall goal of this dissertation work is to advance our understanding about the morphology and generation of ESF events observed during June solstice and/or during post-midnight hours.

2.2 Specific Science Questions

Given the observations available, we focus our analyses on events in the American sector. The following science questions were addressed as part of this dissertation:

1. **Can weakening downward plasma drifts explain the development of post-midnight ESF events observed in the American sector?**

   As mentioned earlier, equatorial plasma drifts are expected to be predominantly downward during post-midnight hours based on climatological estimates of F-region drifts. This scenario has been thought to be unfavorable to the development of ESF. Previous studies, however, have hypothesized that weakening plasma drifts can provide enough

favorable conditions for the growth of the GRT instability in the post-midnight sector and to explain the occurrence of post-midnight ESF during June solstice low solar flux conditions (*Nicolls et al.*, 2006; *Ajith et al.*, 2016). To better understand the relationship between weakening drifts and ESF events observed in the American sector, we will combine radar observations of both vertical plasma drifts and ESF made at the Jicamarca Radio Observatory and ionospheric model analysis.

2. **What is the response in the morphology of post-midnight ESF events to varying solar flux conditions, particularly those of the 2008/2009 deep solar minimum?**

   Satellite studies showed an unexpected high occurrence of post-midnight ESF events during the 2008/2009 deep solar minimum (*Heelis et al.*, 2010). These ESF events were associated with an abnormal behavior of equatorial plasma drifts, which included upward drifts near local midnight (*Stoneback et al.*, 2011). To better understand the behavior of ESF in the American (Peruvian) sector including their origin (in local time), we will analyze the morphology of ESF using long-term (20 years) coherent backscatter radar observations. The observations allow us to determine the response of ESF development to seasonal and solar flux conditions.

3. **What are the spectral features of atypical, post-midnight radar ESF? More specifically, how do they compare with the spectral features of typical, post-sunset ESF events?**

   In order to advance our ability to distinguish non-locally generated (old, fossil) post-midnight ESF events from those locally generated (recent, fresh), we will investigate the spectral characteristics of the Doppler spectra observed by coherent backscatter radar systems. We will focus, in particular, on measurements made in the Brazilian

sector by a new, low-power radar system. The Measurements of Equatorial and Low-latitude Ionospheric irregularities over São Luís, South America (MELISSA) is a 30 MHz radar system that operated in São Luís, Brazil between 2014 and 2018. Unlike previous observations made in that site, raw voltages have been saved allowing us to analyze the Doppler spectra of the observed echoes. We will determine the spectral features of post-midnight ESF events and compare with those of typical ESF in the early (developing ESF phase) and late evening (decaying) phase.

This dissertation is organized as follows: In Chapter 3 we provide information about the results of our efforts towards addressing science question 1. Chapter 4 reports our results related to science question 2. Then, Chapter 5 describes our efforts towards science question 3. Finally, Chapter 6 provides concluding remarks and information about future work. With respect to future work, in Appendix A, we present preliminary results of a potential follow-up investigation related to the following science question:

To what extent can the quiet-time, day-to-day variability of the equatorial vertical drifts contribute to the observed occurrence of post-midnight ionospheric irregularities?

Our previous studies have led us to identify that it would be important to better understand to what degree the day-to-day variability of vertical drifts in the equatorial F-region affect the GRT instability. Focus is to be given to the post-midnight sector during June solstice and low solar flux conditions. Since routine measurements of vertical drifts during the period of interest are not available, we suggest a numerical modeling approach. We will use a state-of-the-art numerical model of the atmosphere and ionosphere (WACCM-X) to derive short-term (day-to-day), physics-based variabilities of the vertical drifts. Aided by climatological models of the drifts, we would then create synthetic drift curves that could emulate the day-to-day variabilities of the drifts for the Peruvian sector. These synthetic

curves could then be used to drive the SAMI2 model whose outputs will be used to evaluate the stability of the nighttime equatorial F-region. Initial results related to the study described above are provided in Appendix.

CHAPTER 3

JUNE SOLSTICE EQUATORIAL SPREAD-F IN THE AMERICAN SECTOR: A NUMERICAL ASSESSMENT OF LINEAR STABILITY AIDED BY INCOHERENT SCATTER RADAR MEASUREMENTS[1]

Authors – Weijia Zhan and Fabiano S. Rodrigues

W. B. Hanson Center for Space Sciences, MS/WT15

The University of Texas at Dallas

800 West Campbell Road

Richardson, Texas 75080-3021

Corresponding author: Weijia Zhan

[1]An edited version of this chapter was published by AGU. Copyright (2018) American Geophysical Union. Zhan, W., & Rodrigues, F. S. (2018). June solstice equatorial spread F in the American sector: A numerical assessment of linear stability aided by incoherent scatter radar measurements. Journal of Geophysical Research: Space Physics, 123, 755 - 767. 2017JA024969. To view the published open abstract, go to https://doi.org/10.1002/2017JA024969.

3.1 Introduction

It is believed that the pre-reversal enhancement (PRE) of the equatorial ionospheric vertical plasma drifts, that occurs around sunset, is the main factor controlling the occurrence of equatorial spread-F (ESF). As pointed in previous studies (*Sultan*, 1996; *Fejer et al.*, 1999), the enhanced upward drifts during the PRE maximize the linear growth rate of the Generalized Rayleigh-Taylor (GRT) instability, which is responsible for ESF, in two ways: The vertical drifts increase, directly, the linear growth rate of the GRT instability. The drifts also lift the F-region to a region of lower ion-neutral collision frequencies increasing even further the GRT linear growth rate. This scenario explains the high occurrence rate of ESF after sunset. It also explains the high ESF occurrence rates during seasons/longitudes where the day-night terminator is aligned with the magnetic meridian. The alignment between terminator and magnetic meridian is known to increase the magnitude of the PRE (*Abdu et al.*, 1981; *Tsunoda*, 1985).

Radar studies have, however, indicated that ESF events can also occur during periods that are not favorable for the development of the GRT instability. These studies have shown an unexpected high occurrence rate of the F-region echoes during post-midnight hours under June solstice and low solar flux conditions (e.g., *Patra et al.*, 2009; *Yokoyama et al.*, 2011; *Otsuka et al.*, 2012; *Li et al.*, 2011). During this period the PRE is expected to be weak with the drifts remaining negative (downward) throughout the night based on climatological studies (e.g., *Scherliess and Fejer*, 1999; *Patra et al.*, 2009), for instance, found the occurrence of F-region irregularities on every night of a 20-day observation campaign with the Gadanki VHF radar in the Indian sector.

Potential hypotheses for the occurrence of ESF during June solstice include the abnormal upward vertical drifts during nighttime hours (e.g., *Yizengaw et al.*, 2013; *Yokoyama et al.*, 2011; *Fang et al.*, 2016). *Yizengaw et al.* (2013) suggested that the upward drift during post-midnight observed by C/NOFS in the African sector could be associated with polarization

electric fields generated by sporadic E layer (Es) instabilities. This off-equatorial polarization electric field would map to the base of the equatorial F-region, where it is associated with abnormal upward drifts.

Yokoyama et al. (2011), based on radar measurements, and *Fang et al.* (2016), based on numerical simulations, also suggested that the so-called midnight temperature maximum (MTM) could be linked to abnormal ESF events. The MTM, which has been linked to a convergence of thermospheric neutral winds towards the magnetic equator, can affect the dynamics of the low-latitude ionospheric plasma and electrodynamics, and produce conditions favorable for ESF development.

An earlier study by *Nicolls et al.* (2006) investigated the occurrence of "apparent" uplifts of the equatorial F-region observed by ionosondes. They showed, using simple numerical simulations of the F-region behavior, that the "apparent" motion of the F-region is a result of the combined effects of recombination in the bottomside F-region and weak $\mathbf{E} \times \mathbf{B}$ downward drifts. More interestingly, they also suggested that the weakening drifts could lead to conditions that are favorable to GRT instability and could explain, at least in part, the occurrence of ESF during post-midnight hours.

More recently, *Ajith et al.* (2016) attempted to explain the occurrence of June solstice, post-midnight radar plumes observed by the Equatorial Atmosphere Radar (EAR) in the Indonesian sector using vertical plasma drift measurements made by the Ion Velocity Meter (IVM) instrument on the C/NOFS satellite. The low temporal resolution of the satellite measurements required them to use an average drift curve based on measurements made at topside heights over a period of two months and a longitude span of 60 degrees. They found, nevertheless, a curve that shows weakening of the downward drifts around midnight. Using this curve and numerical simulations for the Indonesian sector they found positive growth rates during post-midnight hours.

Here, we present the results of a study that investigated the role of weakening drifts on the generation of post-midnight ESF in the American sector. The study combines radar

measurements of vertical plasma drifts and ESF, and data-driven model simulations of the low-latitude ionosphere. Following the procedure of *Ajith et al.* (2016), we use the simulations to evaluate the effects of weakening downward drifts on the linear stability of the equatorial F-region, and the occurrence of post-midnight ESF during June solstice, low solar flux conditions in the American sector.

This chapter is organized as follows: In section 3.2, we provide information about the radar measurements and numerical models of the ionosphere and ESF used in the study. In section 3.3, we present and discuss the main results of our study including those related to simulation of the low-latitude ionosphere using measured and climatological drifts, linear stability analyses, and potential effects of thermospheric winds. In section 3.4, we summarize the main findings of our analyses.

3.2 Measurements, Models and Analyses

3.2.1 Radar measurements

In order to obtain more information about the weakening of nighttime downward drifts as well as ESF, we analyzed measurements made by the Drift Mode experiments (*Kudeki et al.*, 1999) of the incoherent scatter radar (ISR) of the Jicamarca Radio Observatory (11.95° S, 76.87° W, ∼1°N dip latitude).

This mode takes advantage of the two orthogonal polarizations available at Jicamarca to create two antenna beams, one pointed to the west and another to the east. These beams are only a few degrees (∼2.5°) off zenith, and the line-of-sight measurements of the mean Doppler shifts are used to obtain line-of-sight (LOS) ion velocities. These LOS velocities are then combined to obtain the vertical and zonal components of the plasma drifts as a function of local time and height. The radar beams are also pointed close to perpendicular to the magnetic field. Under this geometry, the measured ISR spectrum narrows (*Sulzer and*

Gonzlez, 1999) and allows accurate measurements of the Doppler shifts and velocities. It also allows the detection of coherent scatter echoes produced by field-aligned irregularities associated with ESF. When coherent scatter echoes are present, however, ISR measurements of the drifts are not possible. Nevertheless, the radar mode allows us to study the behavior of the plasma drifts prior to ESF development.

Drift Mode ISR measurements used in this study were made between 1994 and 2013. We found that observations were made in 386 different days during this period. Of those, only 61 measurements were made during June Solstice (June and July) and only 13 (of those 61) were made during conditions considered as of low solar flux (F10.7 $\leq$ 80 SFU). Post-midnight drift measurements are severely affected by the high background (sky) noise, which maximizes around midnight in July/July. Then, we found one night of observations (June 4-5, 2008) when the drift measurements between 18:00 LT and midnight were available, and resemble the pattern that could be used to guide our evaluation of the role of weakening drifts in ESF development.

In addition to ISR measurements, F-region parameters from a collocated digisonde were also available to this study.

3.2.2 Low-latitude ionospheric modeling

In order to better understand and quantify the effects of the nighttime vertical drifts in the low-latitude ionosphere, we followed a data-driven procedure similar to that used by *Ajith et al.* (2016). We combined the low-latitude model of the ionosphere SAMI2 (SAMI2 is Another Model of the Ionosphere) and vertical plasma drift curves estimated from Jicamarca ISR measurements.

SAMI2 is a physics-based theoretical model of the low- and mid-latitude ionosphere (*Huba et al.*, 2000). It describes the dynamics and chemical evolution of seven ion species (H^+, He^+, N^+, O^+, N_2^+, NO^+ and O_2^+) in the altitude range between about $\sim$100 km to

several thousand kilometers. It models the plasma along the geomagnetic field lines from hemisphere to hemisphere including ion inertia in the ion momentum equation for motion along the dipole field line. The neutral species are specified by the NRLMSISE00 model (*Hedin*, 1996). Thermospheric winds are specified by the HWM93 model (*Picone et al.*, 2002).

One of the drivers for SAMI2 is the local time variation of the equatorial vertical plasma drifts. We modified SAMI2 to accept an external input with user-defined drifts, which are based on Jicamarca measurements. We then used SAMI2 thermospheric and ionospheric outputs to evaluate the stability of the equatorial F-region given the history of the drifts.

3.2.3 Numerical assessment of F-region stability

In order to evaluate the stability of the equatorial F-region we followed the procedure described by *Sultan* (1996), and computed the flux-tube integrated linear growth rate of the GRT instability:

$$\gamma_{RT} = \frac{\Sigma_P^F}{\Sigma_P^E + \Sigma_P^F}(V_p - U_L^P + \frac{g_e}{\nu_{eff}})K^F \tag{3.1}$$

Where Σ_P^E and Σ_P^F are flux-tube integrated E- and F-region Pedersen conductivities, respectively. V_p is the equatorial vertical drift velocity. U_L^P is the Pedersen conductivity weighted, flux-tube integrated thermospheric meridional winds perpendicular to field line. g_e is the local gravitational acceleration defined as $\frac{g_0}{L^2}$ (where g_0 is the gravitational acceleration on the equatorial surface of earth, and L is the McIlwain parameter, that is, the geocentric distance in units of Earth radii). ν_{eff} is the flux-tube integrated effective F-region ion-neutral collision frequency weighted by number density along the flux tube. K^F is defined by $\frac{1}{N_e}\frac{\partial N_e}{\partial h}$ (where N_e is the flux-tube integrated electron density, and h is the height in the magnetic equatorial plane).

3.3 Results and Discussion

3.3.1 Weakening vertical plasma drifts

Figure 3.1 shows plasma drift and ESF measurements made by the Jicamarca ISR when an event of weakening downward drifts was identified on June 4-5, 2008 for this study. The event was observed during low solar flux conditions. The mean F10.7 solar flux index for June 4-5 is 68 SFU. The event was also measured under quiet geomagnetic conditions. The geomagnetic Kp index did not exceed 1 on June 4 and did not exceed 2 on June 5.

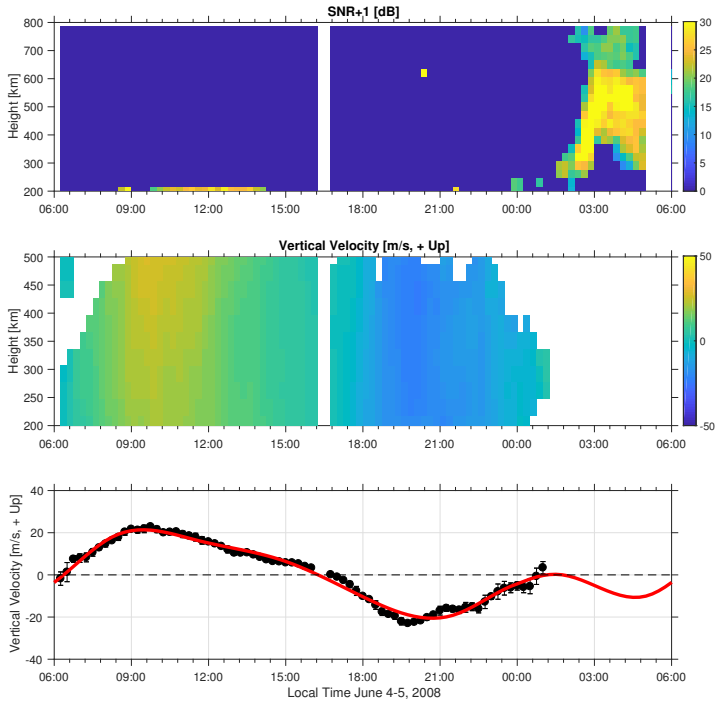

Figure 3.1. (Top) Range-Time-Intensity (RTI) map for June 4-5, 2008. (Middle) Jicamarca ISR vertical drifts as a function of local time and height; positive values for upward drifts. (Bottom) Black markers shown mean vertical drifts for an altitude around 300 km. Red line shows interpolated drifts.

The top panel of Figure 3.1 shows the Range-Time-Intensity (RTI) map of the observed echoes. The RTI maps shows that a post-midnight ESF event started to appear around 01:30

LT. The echoes show a bottom-type layer around 02:00 LT and then a topside layer (plume) starting around 03:00 LT. The sequence resemble the development of typical, pre-midnight ESF (e.g. *Woodman and La Hoz*, 1976; *Hysell and Burcham*, 2002; *Smith et al*, 2015).

The middle panel shows the vertical drift velocity as a function of local time and height. One can see that the drifts did not change significantly with height during the period when measurements are available. Note that accurate ISR drift observations were not available during periods of ESF or when the electron density was extremely low.

The bottom panel shows, as black markers, average drifts for the height around 300 km. The error bars represent the variability (standard deviation) of the drifts measurements used in the average. In addition to the measured drifts we also show, as a red line, modeled drifts. The modeled drifts were obtained using cubic B-splines. Because no measured drifts were available in the period around the ESF event, we chose to use a periodic (diurnal) cubic B-spline curve to model the drifts. The model curve resembles the drift pattern considered by *Nicolls et al.* (2006) and, therefore, can then be used to drive the numerical simulations and evaluate the effects of weakening drifts in the linear stability of the equatorial F-region.

Figure 3.2 shows the behavior of the F-region over Jicamarca prior to and during the weakening of the drifts. The top and middle panels show, again, the RTI map of the echoes and the mean vertical drifts, respectively. The bottom panel shows the virtual height of the base of F-layer (h'F) estimated from collocated ionograms. One can identify an increase in h'F starting around 22:30 LT, when the magnitude of drifts is about 10 m/s or less, which agrees with *Nicolls et al.* (2006)'s hypothesis of apparent uplifts associated with weak downward drifts.

The weakening of the downward drifts between 21:00 LT and 01:00 LT could lead one to think that there is, indeed, a causal relationship with the ESF event observed later on, as proposed by *Nicolls et al.* (2006). In the following sections, we present numerical simulations and analyses that better quantify the potential relationship between the drift pattern and ESF development.

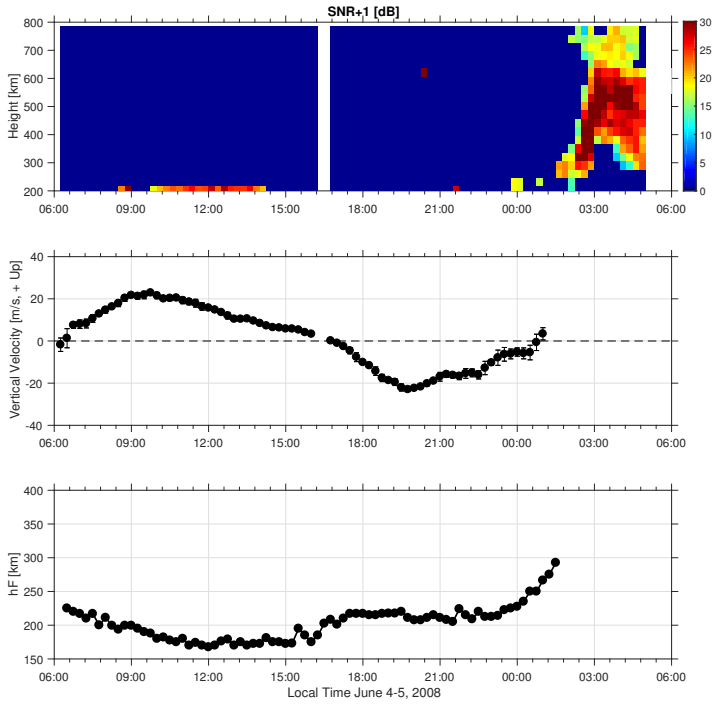

Figure 3.2. (Top) Range-Time-Intensity (RTI) map for June 4-5, 2008. (Middle) Mean vertical drifts for an altitude around 300 km. (Bottom) Digisonde estimates of the virtual height of the base of the F-layer (h'F) as a function of local time.

3.3.2 SAMI2 simulations: Apparent uplifts

Using the model vertical drifts (red line in Figure 3.1) we ran a simulation of the low-latitude ionosphere using SAMI2 for the solar, geomagnetic and thermospheric conditions of June 4-5, 2008 and the magnetic meridian plane of the Jicamarca site.

Figure 3.3 shows the results of the simulation illustrating the effects of weakening downward drifts in the F-region over Jicamarca. The top panel of Figure 3.3 shows the input model drifts. The bottom panel shows the electron density profiles for the Jicamarca location as a function local time. To aid visualization of the results we also show iso-contours of the electron densities. The iso-contours help to identify an increase in the height of the bottomside F-region, starting around 22:30 LT. At about 02:30 LT, one can see steep vertical

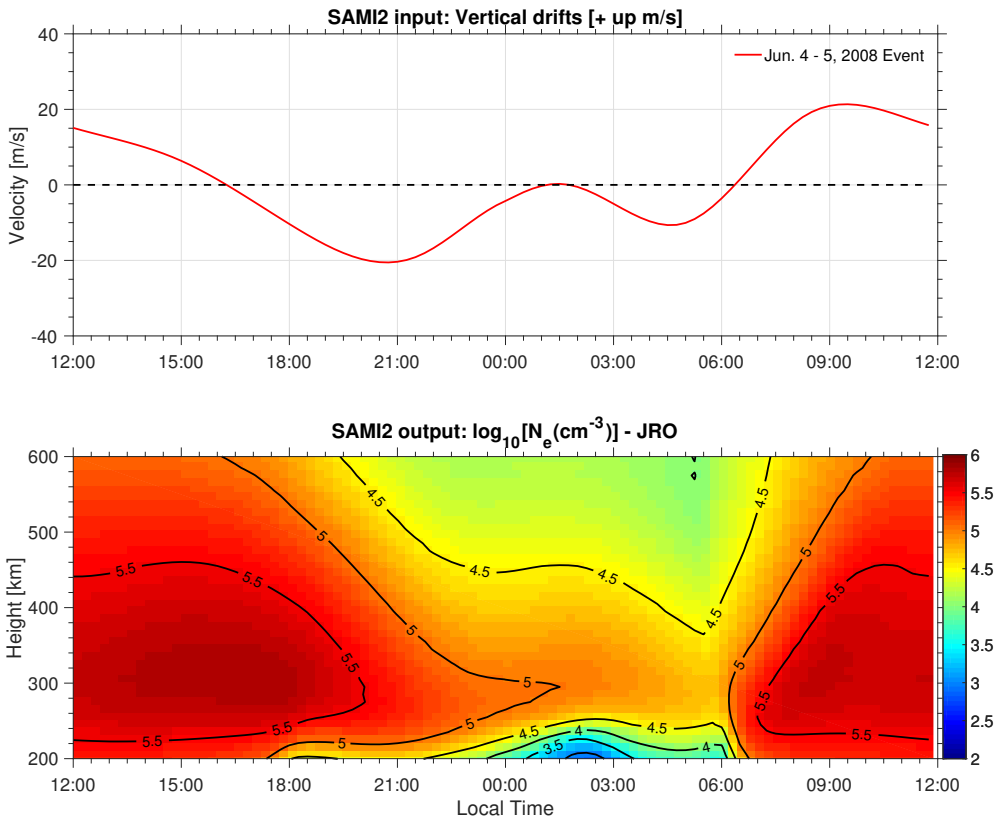

Figure 3.3. (Top) Model vertical drifts used to drive SAMI2. (Bottom) SAMI2 results of the electron density for Jicamarca. Iso-contours of electron density are also shown to help identify the behavior of the equatorial F-region.

gradients in electron density when the bottomside F-region reaches an altitude of about 250 km.

The SAMI2 simulations, driven by actual equatorial drifts, confirm the apparent uplift effects proposed by *Nicolls et al.* (2006). The simulations also indicate the contribution of weakening drifts to creating an unstable F-region in the post-midnight sector.

3.3.3 SAMI2 simulations: Linear growth rates

Using thermospheric and ionospheric outputs of SAMI2, we also computed the flux-tube integrated values of the linear growth rate for the GRT instability (Equation 3.1).

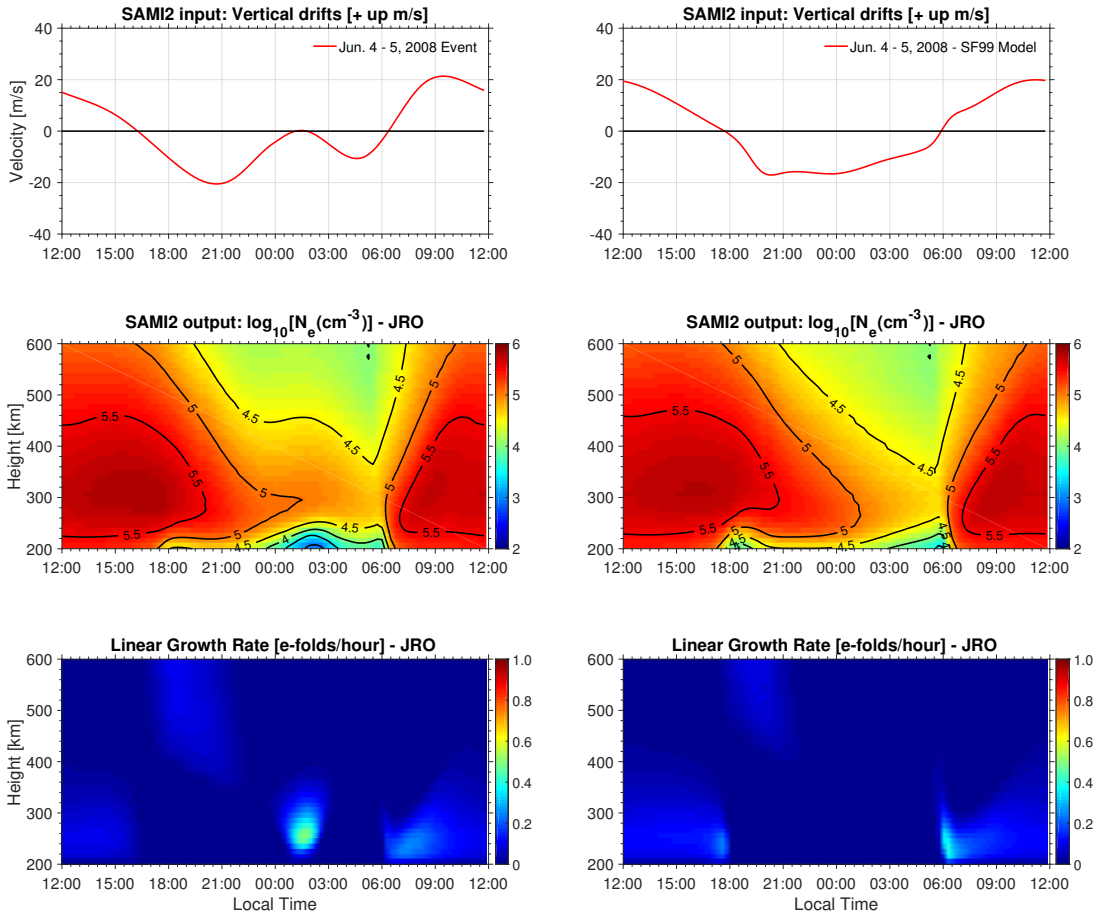

Figure 3.4. Results of SAMI2 simulations using measured drifts (left hand side panels) and climatological (SF99) model drifts (right hand side) for June 4-5, 2008. Top panels: Equatorial vertical plasma drifts used as input. Middle panels: Local electron density over Jicamarca. Bottom panels: Flux-tube integrated linear growth rates for GRT instability.

Figure 3.4 shows the results of our estimates of the growth rates. It shows results of two distinct scenarios, for comparison purposes. The left hand side panels show the results for simulations using the drifts based on measurements made during the event of June 4-5, 2008. The right hand side panels show the results for SAMI2 simulations that were obtained using the *Scherliess and Fejer* (1999) climatological model of vertical drifts for the same day. For each case, the top panel shows the input vertical drifts used in the SAMI2 simulations. The

middle panels show the electron density over Jicamarca as a function of local time. The bottom panels show the linear growth rates (in e-folds per hour) computed using simulation results. Iso-lines are added to help the reader to better identify growth rate values.

Unlike the measured drifts, the climatological drifts (right hand side) show downward plasma motion throughout the night. The drifts are about -18 m/s between sunset and midnight. Then the magnitude of the drifts start to slowly decrease (weaken). The slow weakening of the drifts only produce, as a result, a weak (and slow) apparent uplift of the F-layer. Only at sunrise the drifts are near 0 m/s, and the F-region peak reaches about 300 km altitude. No indication of strong vertical density gradients in the bottomside F-region are observed for most of the night. Even if density gradients where produced, they would be at altitudes where the $\frac{g_e}{\nu_{eff}}$ term of the growth rate is very small. Additionally, the downward climatological drifts lead to negative growth rates throughout the night. There are, however, positive but small growth rates when the drifts reverse direction, around sunset as well as sunrise.

The small growth rates around sunset are expected, based on the low occurrence rate of premidnight F-region echoes associated with the (weak or absent) PRE in June/July (e.g. *Smith et al*, 2015). Interestingly, the growth rates around sunrise are greater than those around sunset. The positive growth rates around sunset are driven, mainly, by increases in the bottomside vertical density gradients, which are caused by the rapid decrease in bottomside density due to recombination. The positive growth rates around sunrise are caused by a combination of the reversal of the drifts (upward after $\sim$ 06:00 LT) and vertical density gradients.

Finally, the simulations using the actual drifts for the June 4-5 event show, as mentioned earlier, an increase in the bottomside F-region height and vertical density gradient in the post-midnight sector (around 01:30 LT). These gradients, combined with an elevated height of the F-region (increased $\frac{g_e}{\nu_{eff}}$), produce favorable conditions for the GRT instability. This

is quantified by our calculation of the GRT linear growth rate, which shows positive values of about 0.5 e-folds per hour around 01:30 LT, just prior to the detection of ESF by the Jicamarca radar.

We must point out that while our results do confirm that the weakening drifts cause an unstable post-midnight F-region, the growth rates values are surprisingly small. They are much smaller than the values obtained by *Ajith et al.* (2016) (2.8 e-folds/hour or $\gamma_{GRT} = 7.8\times10^{-5}$ s^{-1}) for the Indonesian sector, and might not be able to explain the observations of a fully developed ESF plume.

3.3.4 Comparisons with typical ESF conditions

In order to better evaluate the growth rates observed in June 4-5, 2008, we also estimated growth rates for conditions of typical ESF occurrence in the Peruvian sector, that is, December and Equinox conditions.

Figure 3.5 shows results of SAMI2 simulations and growth rate calculations for December solstice (December 21, 2008) and March equinox (March 21, 2008) when ESF is known to occur associated with the PRE. The left hand side panels show the results for December, while the right side panels show results for March. The most noticeable feature in the simulation results is the positive growth rates around sunset, driven by the PRE.

In December solstice, there is a misalignment between the terminator and the magnetic meridian in the Peruvian sector, and the PRE is not expected to fully develop (*Abdu et al.*, 1981; *Tsunoda*, 1985). The *Scherliess and Fejer* (1999) drift model confirms that those conditions translate into a weak PRE followed by a slow reversal of the drifts after sunset. Despite the weak PRE, the growth rates are noticeably larger than those seen during the June 4-5 event. Growth rate values reach about 0.74 e-folds/hour around sunset, and are negative or near zero during the rest of the night.

The simulations for March equinox (right hand side panels of Figure 3.5) show, again, positive growth rates right after sunset. The growth rate values are greater than those

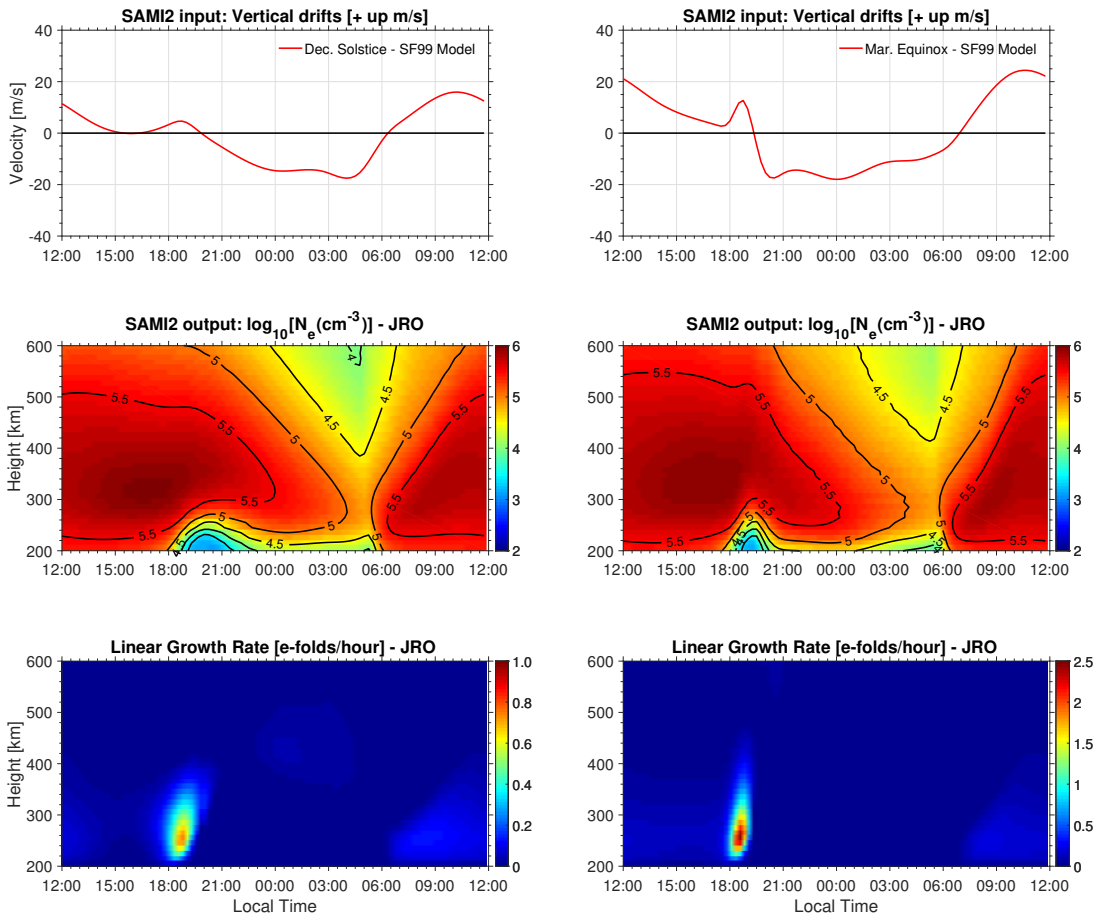

Figure 3.5. Same as Figure 3.4 but driving SAMI2 with *Scherliess and Fejer* (1999)(SF99) model drifts for December 21, 2008 (left side panels) and March 21, 2008 (right side panels). Note that the growth rate color scale for March equinox is different from the other cases.

obtained for December solstice. Note that the color scale is different from that used for Equinox conditions. During equinox, the magnetic meridian and the terminator are well-aligned providing optimal conditions for the development of the PRE. The *Scherliess and Fejer* (1999) model shows that indeed, under those conditions, a strong PRE peak can be observed. The alignment during equinox also makes the PRE to occur over a short period of time, which then makes the drifts to revert direction much more quickly than under December

solstice conditions. Associated with this well-developed PRE, we can also see steep gradients in the local electron density and growth rate values reaching 2.5 e-folds per hour. Our results for equinox conditions agree with those obtained by *Ajith et al.* (2016). While our post-sunset growth rates were about 2.5 e-folds/hour, their results for the Indonesian sector and average C/NOFS drifts were around 2.8 e-folds/hour.

The behavior of the PRE and estimates of the growth rates agree with observational results of drifts and ESF at Jicamarca. *Smith et al* (2016), for instance, showed that ESF events develop more quickly during Equinox. This is a consequence of the larger growth rates during that period. They also showed that ESF events tend to last long during December solstice. This has been attributed to the slow reversal of the drifts and, consequently, slow process of F-region stabilization.

The numerical simulations show that the linear growth rate values for the June 4-5 event (0.5 e-folds/hour) are not much smaller than those obtained by *Ajith et al.* (2016) for June solstice conditions in Indonesia, but are also much smaller than those obtained for equinox post-sunset. Furthermore, the June event growth rates are smaller than those obtained for December solstice during post-sunset hours. Therefore, the results suggest that even though unstable conditions are produced by the weakening event of June 4-5, it is unlikely to explain, alone, the development of the full blown radar plume observed by the Jicamarca radar.

In the following section, we explore the hypothesis of meridional winds contributing to destabilizing the equatorial F-region and producing the post-midnight ESF event observed on June 4-5, 2008.

3.3.5 Thermospheric wind effects

The results presented in the previous sections showed that our growth rate values (0.5 e-folds per hour) for the June 4-5, 2008 event at Jicamarca are much smaller than those obtained by *Ajith et al.* (2016) for weakening drifts in the Indonesian sector (2.5 e-folds per hour) and

weaker than the growth rates obtained for typical post-sunset ESF conditions. These results have led to us to explore additional conditions leading to higher growth rates, which could explain the observed post-midnight ESF event of June 4-5, 2008.

Ajith et al. (2016) pointed that, for June solstice conditions, meridional neutral winds converge towards the magnetic equator in the Indonesian sector, based on climatological (HWM93) estimates. For the Peruvian sector, however, we found that the meridional winds are mostly northward across the magnetic equator, between 21:00 and 03:00 LT.

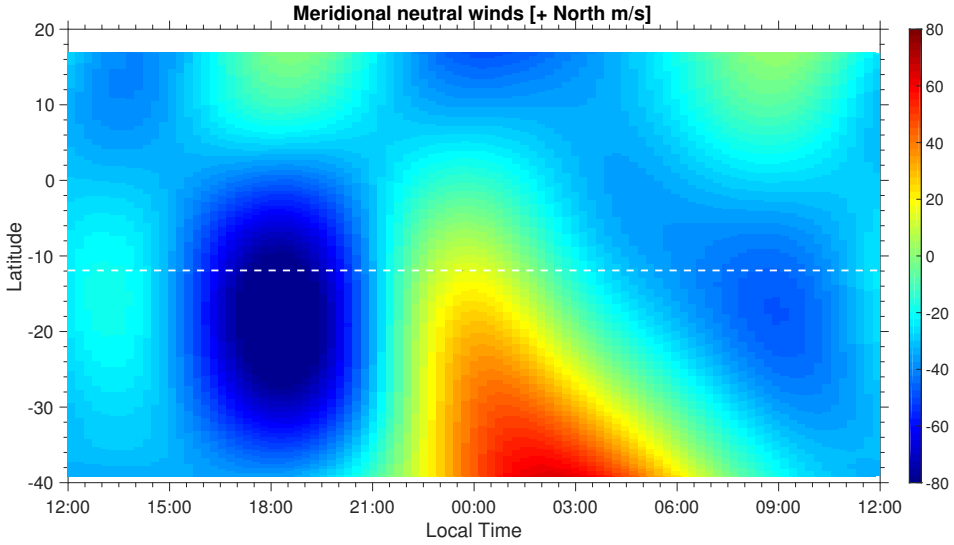

Figure 3.6. HWM93 meridional winds (around 200 km altitude) used in SAMI2 simulations for June 4-5, 2008. The dashed line indicates the latitude of Jicamarca (11.95° S).

This is illustrated in Figure 3.6, which shows the meridional component of neutral winds at 200 km altitude as a function of local time and latitude. This is particularly true for latitudes that are only a few degrees away from Jicamarca (white dashed line) and that have magnetic field lines mapping to the bottomside and main F-region at the magnetic equator. Therefore, we are inclined to suggest that the climatological (trans-equatorial) winds in the American sector might have a stabilizing effect in the calculation of the GRT instability (*Maruyama*, 1988; *Sultan*, 1996).

Next, we consider the effects of departures from the climatological expectations for the meridional winds. We investigate, in particular, the cases of equatorward and poleward wind patterns such as those proposed by *Huba et al.* (2013) in their numerical experiments, but now applied to post-midnight June solstice conditions. The model for the latitudinal variation of the meridional winds proposed by *Huba et al.* (2013) is given by:

$$U_m = U_{m0} \tanh\left(\frac{\theta}{\delta\theta}\right) \tag{3.2}$$

where $U_{m0} = \pm 40$ m/s, θ is latitude and $\delta\theta = 5°$. Positive U_m indicates northward winds, and θ increases in the northward direction. Therefore, $U_{m0} = +40$ m/s is used for poleward (diverging) winds, and U_{m0} = -40 m/s for equatorward (converging) winds. Figure 3.7 shows the latitudinal variation of the modeled winds used in this analysis.

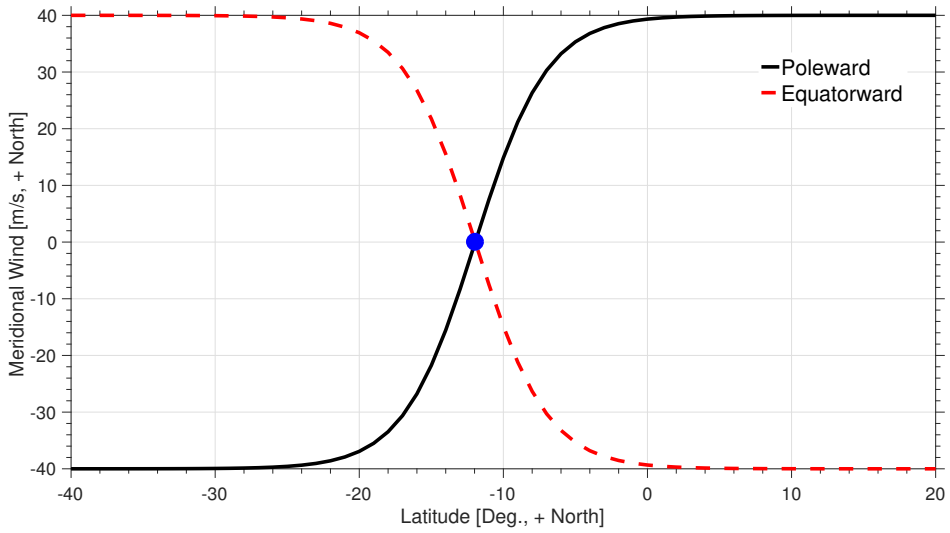

Figure 3.7. Meridional wind patterns (poleward and equatorward) used in the numerical experiments. The blue marker indicates the latitude of Jicamarca (11.95° S).

Figures 3.8, 3.9 and 3.10 show the results of SAMI2 simulation and growth rate analyses for the case of climatological meridional winds (HWM93), poleward winds and equatorward winds, respectively.

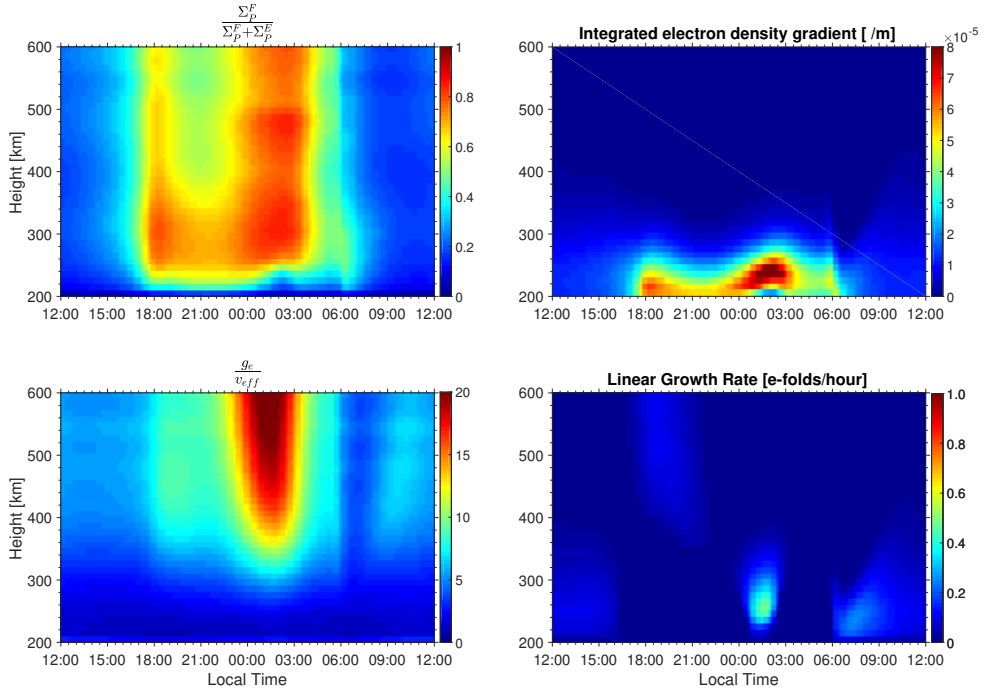

Figure 3.8. Linear growth rate results for June 4-5, 2008 using climatological (HWM93) meridional winds and weakening downward drifts. Top left: ratio of integrated Pedersen conductivity. Top right: integrated electron density gradient (Top-right). Bottom left: $\frac{g_e}{v_{eff}}$. Bottom right: Linear growth rate.

Comparing the results, we found that poleward winds (Figure 3.9) cause the ratio of F-region flux tube integrated Pedersen conductivity to decrease at night compared to climatological wind conditions (Figure 3.8). The electron density gradient, especially in the post-midnight sector, is also severely reduced. Significant changes (decrease) in the $\frac{g_e}{v_{eff}}$ term can also be observed, particularly at topside heights (>300 km). As a result, the estimated linear growth rate is near zero in the post-midnight sector, which indicates the stabilizing effect of poleward meridional winds.

Looking at results for equatorward winds (Figure 3.11), we can see that the conductivity ratio increases in the post-midnight sector, compared to results using climatological winds. The integrated electron density gradient also increases. The equatorward winds cause the $\frac{g_e}{v_{eff}}$ term to increase, specially at apex heights greater than ∼300 km. As a result, the

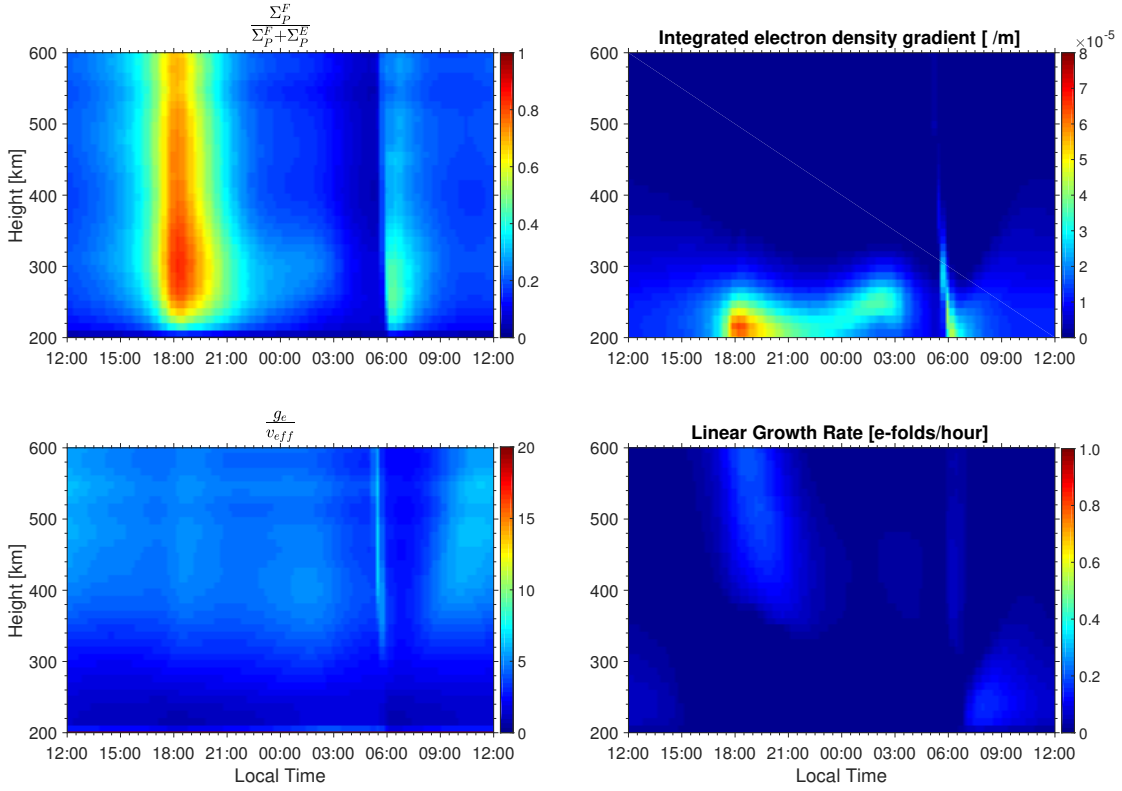

Figure 3.9. Linear growth rate results for June 4-5, 2008 using diverging (poleward) meridional winds and weakening downward drifts. Top left: ratio of integrated Pedersen conductivity. Top right: integrated electron density gradient (Top-right). Bottom left: $\frac{g_e}{v_{eff}}$. Bottom right: Linear growth rate.

equatorward winds cause the linear growth rate to increase substantially reaching about 1.5 e-folds per hour around the time of interest here (01:30 LT), preceding the appearance of ESF.

Finally, we also test whether or not converging winds alone could destabilize the post-midnight equatorial F-region. For that case, we produced simulations without the weakening drifts. Instead, we used climatological drifts from the *Scherliess and Fejer* (1999) model for June 4-5, 2008. The drift pattern is similar to that shown in Figure 3.4, top right panel. The results of the simulations are presented in Figure 3.11, in the same format of Figures 3.8-3.10. They show that the equatorward winds are destabilizing around sunset and sunrise, when

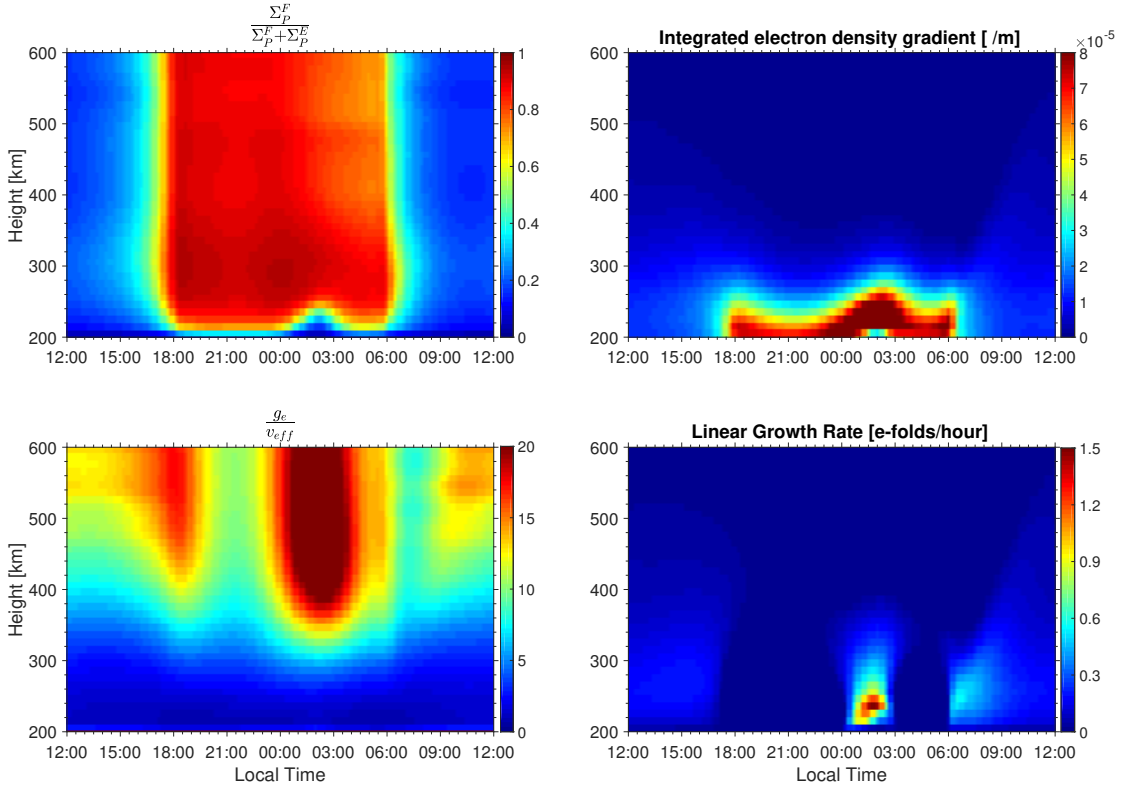

Figure 3.10. Linear growth rate results for June 4-5, 2008 using converging (equatorward) meridional winds and weakening downward drifts. Top left: ratio of integrated Pedersen conductivity. Top right: integrated electron density gradient (Top-right). Bottom left: $\frac{g_e}{v_{eff}}$. Bottom right: Linear growth rate.

drifts are positive. Equatorward winds alone, however, do not create an unstable F-region in the post-midnight sector. Only negative linear growth rates are observed.

Therefore, the simulation results quantify the destabilizing effects of an weakening downward drift. The destabilizing effects are even greater during the occurrence of converging neutral winds. In that scenario, the linear growth rate values are similar to those observed during typical, premidnight ESF conditions, and might explain the June 4-5, 2008 plume event. We suspect that weakening drifts and converging winds are not independent features of the equatorial ionosphere. Recently, using numerical simulations, *Fang et al.* (2016) showed that the converging winds associated with the Midnight Temperature Maximum

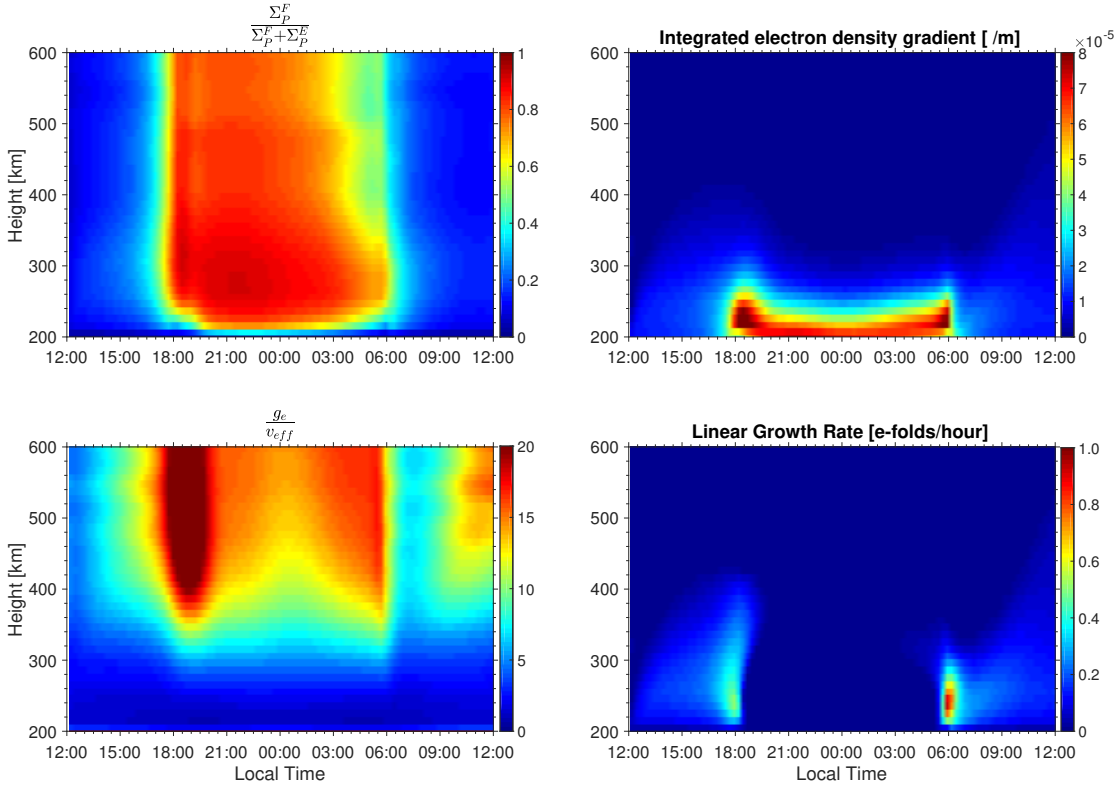

Figure 3.11. Linear growth rate results for June 4-5, 2008 using converging (equatorward) meridional winds and climatological (*Scherliess and Fejer*, 1999) equatorial drifts. Top left: ratio of integrated Pedersen conductivity. Top right: integrated electron density gradient (Top-right). Bottom left: $\frac{g_e}{\nu_{eff}}$. Bottom right: Linear growth rate.

(MTM) are linked to upward drifts in the midnight/post-midnight sector. It is possible that the drifts of June 4-5, 2008 are the result of a similar process.

3.4 Summary and Conclusions

Previous studies have suggested that weakening downward equatorial plasma drifts can explain ionosonde observations of "apparent" F-region uplifts and produce an unstable equatorial post-midnight F-region. In this work we investigated this hypothesis using numerical simulations, aided by incoherent scatter radar (ISR) measurements of equatorial vertical

plasma drifts, in an attempt to explain equatorial spread-F (ESF) events observed in the American sector during June solstice, low solar flux conditions.

We found adequate Jicamarca ISR measurements during a prototypical, quiet-time event observed on June 4-5, 2008 when the downward drifts weakened and a fully developed ESF event was observed. The Jicamarca drifts were used as input for the NRL SAMI2 model of the low and middle latitude ionosphere.

SAMI2 reproduced the "apparent" uplift of the ionosphere that was consistent with expectations and observations. It also provided thermospheric and ionospheric parameters for estimation of the flux-tube linear growth rates of the Generalized Rayleigh-Taylor (GRT) instability associated with the weakening drift event. We found that the weakening drifts do produce unstable conditions with positive linear growth rate values. The growth rates, however, were slower than those obtained for typical, premidnight ESF events. The growth rates were also much weaker than those obtained for June solstice, post-midnight hours, under similar equatorial drift conditions in the Indonesian sector (*Ajith et al.*, 2016).

Following the hypothesis of *Huba et al.* (2013), we investigated the possibility of wind patterns departing from climatological predictions to contribute to the unstable condition responsible for the ESF event observed on June 4-5, 2008. We found that the occurrence of equatorward winds during post-midnight hours, and during an weakening drift event, can produce favorable conditions for instability development.

Finally, we point out that equatorward winds and weakening of the plasma drifts might not be independent phenomena. *Fang et al.* (2016) recently showed that converging winds associated with the midnight temperature maximum (MTM) can even cause reversals in the equatorial plasma drifts, which might explain post-midnight upward drifts observed by C/NOFS and the weakening of the drifts observed by Jicamarca.

CHAPTER 4

ON THE GENESIS OF POST-MIDNIGHT EQUATORIAL SPREAD-F: RESULTS FOR THE AMERICAN/PERUVIAN SECTOR[1]

Authors – Weijia Zhan, Fabiano S. Rodrigues and Marco A. Milla

W. B. Hanson Center for Space Sciences, MS/WT15

The University of Texas at Dallas

800 West Campbell Road

Richardson, Texas 75080-3021

Corresponding author: Weijia Zhan

[1]An edited version of this chapter was published by AGU. Copyright (2018) American Geophysical Union. Zhan, W., Rodrigues, F., & Milla, M. (2018). On the genesis of postmidnight equatorial spread F: Results for the American/Peruvian sector. Geophysical Research Letters, 45, 7354 7361. 2018GL078822. To view the published open abstract, go to https://doi.org/10.1029/2018GL078822.

4.1 Introduction

Equatorial spread F (ESF) is the name given to signatures of ionospheric irregularities observed at equatorial and low-latitudes by a variety of space- and ground-based instruments (e.g. *Kelley et al.*, 1976; *Woodman and La Hoz*, 1976; *McClure et al.*, 1977; *Sobral et al.*, 1980; *Abdu et al.*, 1981). The development of ESF irregularities is commonly explained by the Generalized Rayleigh-Taylor (GRT) instability (*Sultan*, 1996). The main factor controlling the conditions for GRT instability growth is often credited to the upward component of the $\mathbf{E} \times \mathbf{B}$ drifts (e.g. *Fejer et al.*, 1999). A pre-reversal enhancement (PRE) of the upward drifts (*Eccles et al.*, 2015) is observed around sunset hours in most longitude sectors during equinoctial months (e.g. *Gentile et al.*, 2006) and explains, for the most part, the high occurrence rate of ESF events observed in the post-sunset sector (e.g. *Fejer et al.*, 1999; *Smith et al*, 2016).

The Communication/Navigation Outage Forecasting System (C/NOFS) satellite was launched in 2008 with the main objective of studying ESF and the effects of these events on radio propagation and applications (*de La Beaujardiere et al.*, 2004). C/NOFS was launched on a low inclination (13°) elliptical orbit, with an orbital period of ∼97 minutes. The orbit had a perigee of 405 km and an apogee of 853 km at the beginning of the mission. The satellite reentered the Earth's atmosphere on November 28, 2015 after about 7.5 years of nearly uninterrupted observations. One of the first and most interesting findings of the C/NOFS mission is an unexpected behavior in the occurrence of ESF (e.g. *Burke et al.*, 2009; *Su et al.*, 2009; *Heelis et al.*, 2010; *Yizengaw et al.*, 2013).

Heelis et al. (2010), in particular, analyzed ion density perturbations based on measurements made in the deep solar minimum of 2008-2009 by sensors that are part of the Coupled Ion Neutral Dynamics Investigation (CINDI) instrument package on C/NOFS. They pointed out a maximum in the occurrence rate of irregularities across midnight into the post-midnight

hours during June and December solstices. This behavior greatly departed from expectations based on previous observations.

Stoneback et al. (2011) then analyzed low-latitude drift measurements made between 2009 and 2010 by the ion velocity meter (IVM) sensor on CINDI. They found a semi-diurnal component in the variation of the vertical component of the equatorial plasma drifts. While the semi-diurnal variation was observed in all seasons, it was strongest in June and December solstices. This semi-diurnal variation led to downward drifts in the afternoon and upward drifts around midnight. *Stoneback et al.* (2011) pointed out that the upward drifts near midnight correspond to the regions with a high occurrence rate of post-midnight irregularities, which indicates a potential causal relationship between the observed drifts and ESF.

Here, we take advantage of the long-term observations of equatorial F-region irregularities made by the 50 MHz coherent backscatter radar (JULIA) (*Hysell and Burcham*, 1998) of the Jicamarca Radio Observatory to study the response of ESF occurrence to changes in solar flux conditions, including those of the deep solar minimum in 2008-2009 in the American sector. Using these measurements, we produce maps (height versus local time) of irregularity occurrence for different seasons and solar flux conditions between 1996 and 2015. We then use these maps to better understand the genesis, development and decay of ESF irregularities in the American sector under different seasonal and solar activity conditions. We seek, in particular, to use ground-based observations to better understand the origin, in local time, of post-midnight ESF events detected by previous satellite (topside) observations during the 2008-2009 solar minimum.

4.2 Measurements and Analyses

4.2.1 Measurements

The Jicamarca Unattended Long-term Investigations of the Ionosphere and Atmosphere (JULIA) radar is a 50 MHz coherent backscatter ground-based radar system that is part of a set of ground-based instruments located at the Jicamarca Radio Observatory (11.95°S, 76.87°W, ∼1° dip lat) (*Hysell and Burcham*, 1998). In the initial implementation of JULIA, two 30 kW transmitters were used to excite the North and South quarters of the Jicamarca antenna. These transmitters were combined as to maximize the directivity of the combined pattern in the direction perpendicular to the geomagnetic field at F-region heights. This maximizes the sensitivity of the system to field-aligned irregularities. Receivers were also connected to the East and West quarters of the Jicamarca antenna. This setup allowed interferometric analyses of the echoes and the determination of the zonal component of irregularity velocity.

While modifications to JULIA have been made since its first light in 1996, the system continued to be able to make routine (150-200 days per year) coherent backscatter radar observations of daytime and nighttime echoes caused by field-aligned ionospheric irregularities at E- and F-region heights. The measurements used in this study consist of the signal-to-noise ratio (SNR) of the nighttime F-region echoes observed by JULIA. For nighttime F-region observations, the measurements typically start 1800 LT and end at around 0800 LT next day. The measurements made by JULIA cover altitudes ranging from about 90 km to 800 km or above.

Figure 4.1 (top panel) shows the Range-Time-Intensity (RTI) map of the JULIA measurements made on March 2, 2001. The RTI map shows a typical example of an ESF event detected by JULIA. It shows the appearance of first echoes around 1930 LT coming from a bottom-type layer located around 350 km altitude. The bottom-type is then followed by the

appearance of topside echoing layers (plumes) starting at 2000 LT . By 2300 LT very few echoes are detected by JULIA. Departures from this pattern driven by solar flux conditions are addressed in this study.

4.2.2 Analyses

In order to better understand the response in the genesis, development and decay of irregularities to solar flux conditions, we analyzed the RTI maps of JULIA measurements made between 1996 and 2015. Measurements made on 2,470 days during that period were available and used in this study.

In order to obtain information about the morphology of ESF over Jicamarca we created maps of the seasonal occurrence rate of irregularities for each year between (and including) 1996 and 2015. To create these maps, we carefully analyzed each JULIA RTI map and determined the occurrence of irregularities as a function of height and LT. Figure 4.1 illustrates the process.

The top panel shows an example of the RTI SNR values available for this study. The bottom panel shows the locations (in height and time) for which measurements were available (blue or orange regions) and the locations where irregularities were identified (orange regions). The irregularities were identified based on number of echoes above a certain SNR within a time versus height interval. The observations for each day were grouped in a height versus time matrix. The matrix has resolutions of 15 minutes and 20 km in height. Irregularity detection is assigned to a matrix bin when more than 10 echoes with SNR greater than -20 dB were detected. The SNR threshold (-20 dB) and number of echoes (at least 10) was chosen as to minimize the mis-identification of interference and clutter as echoes caused by ESF irregularities. Despite our efforts, we were still forced to remove a number of measurements from our analyses due to strong contamination of the observations by interference from artificial sources. As a result, we were left with 2,457 days of observations for our analyses.

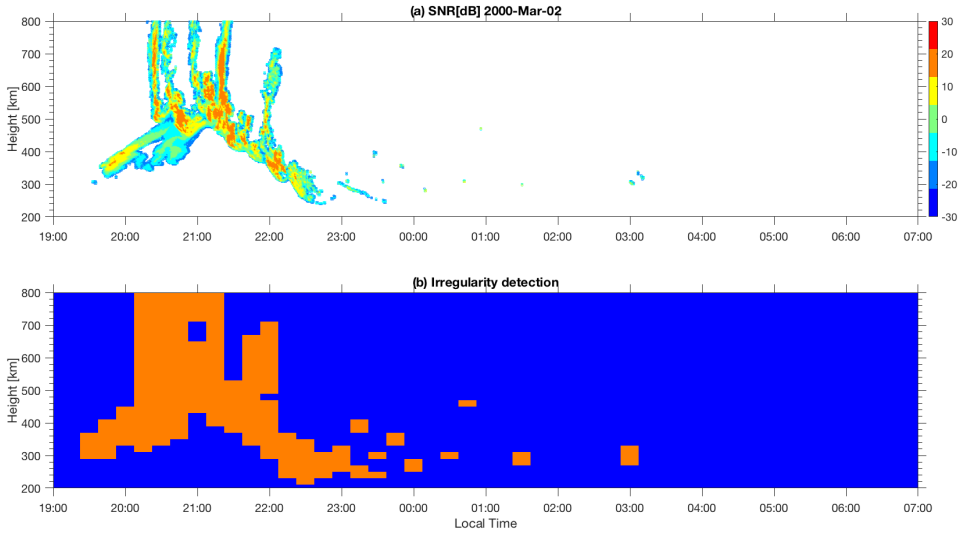

Figure 4.1. The top panel shows an example of the Range-Time-Intensity map of echoes measured by JULIA on March 2, 2000. The bottom panel shows the regions were ESF irregularities were identified based on number of echoes above a certain SNR threshold. Please, see text for more details.

We also only considered measurements made during geomagnetically quiet conditions. Each SNR value was tagged with the geomagnetic Planetary K (Kp) index value at the time of the measurement and the previous four Kp values. Only observations with all the five Kp values less than 4 were considered in our analysis.

The observations available for this study cover a broad range of solar flux conditions, which can be represented by the F10.7 solar flux index. The variation of F10.7 index over the observation period (1996 to 2015) is shown in Figure 4.2. It covers two solar maxima and two minima including the extreme solar minimum of 2008-2009.

4.3 Results and Discussion

Figure 4.3 summarizes the results of our analyses. It shows the response of the seasonal occurrence of radar ESF to varying solar flux conditions. The bottom panel shows the variation of the average solar flux index for each season from 1996 to 2015. The other

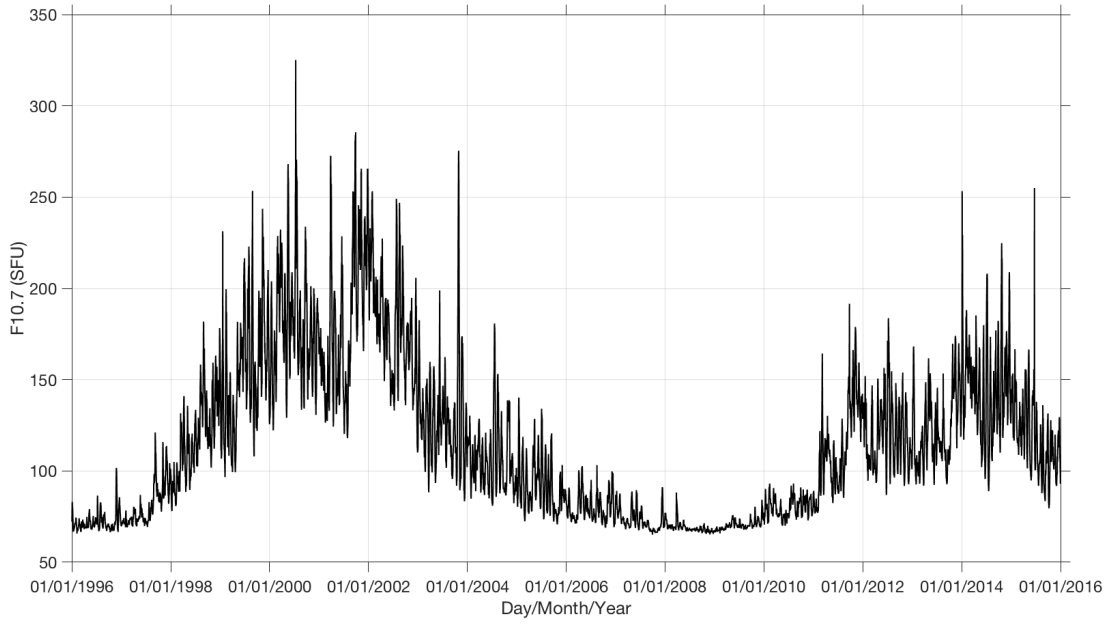

Figure 4.2. Variation of the solar flux index (F10.7) during the period under which JULIA measurements were made.

panels show the occurrence rates of ESF irregularities observed by JULIA for each season from 1996 to 2015. The occurrence rates correspond to number of days where ESF was detected over the total number of observation days. Seasons were also organized based on ±45 days centered around March 21 (March Equinox), June 21 (June Solstice), September 21 (September Equinox) and December 21 (December Solstice). White regions in the panels indicate times when less than 10 observation days are available.

4.3.1 On post-sunset ESF

As expected, our results show a strong seasonal variation in the occurrence rates of post-sunset ESF. ESF is observed to occur, predominantly, during equinox and December solstice when the PRE is well developed (*Fejer et al.*, 1999; *Smith et al*, 2016). During June solstice, however, ESF occurrence rates are severely reduced.

Our results also show that post-sunset ESF starts to be observed at earlier local times during periods of high solar activity, which is in agreement with previous studies (e.g. *Fejer et al.*, 1999; *Hysell and Burcham*, 1999; *Chapagain et al.*, 2009; *Cueva et al.*, 2013; *Smith et al*, 2016). Also in agreement with previous studies is the appearance of the first echoes at higher altitudes during periods of high solar activity. Finally, we also found that during periods of high solar activity the echoes reach a threshold altitude (say, 400 km) more quickly than during periods of low solar flux activity.

Our results also show that post-sunset echoes last longer during periods of low solar flux conditions. This is credited to weaker downward drifts (stabilization) after the PRE during periods of low solar activity (*Fejer et al.*, 1999; *Hysell and Burcham*, 1999; *Smith et al*, 2016). This effect is more pronounced during December solstice but is also observed during equinox.

During equinoctial months significant occurrence rates (say $> 50\%$) are observed until about 2200 LT under moderate to high solar flux conditions, and until midnight during periods of low solar flux. During December solstice, however, significant occurrence rates can be observed until dawn (0050-0600 LT) under low solar flux conditions.

Unfortunately, there is a gap in the JULIA observations of June solstice ESF for periods of high solar flux conditions (years 1996-1998 and 2000-2001). The June solstice measurements available for this study were mostly made under low or moderate solar flux activity (average F10.7 < 130 SFU). While the observations do not allow us to identify an obvious pattern for June solstice, it suggests a reduction in post-sunset events during low solar flux conditions (See years $2007-2010$).

4.3.2 On post-midnight ESF

Of main interest to this study is the occurrence of post-midnight ESF events and the response to seasonal and solar flux variations. As mentioned earlier, C/NOFS found a predominance

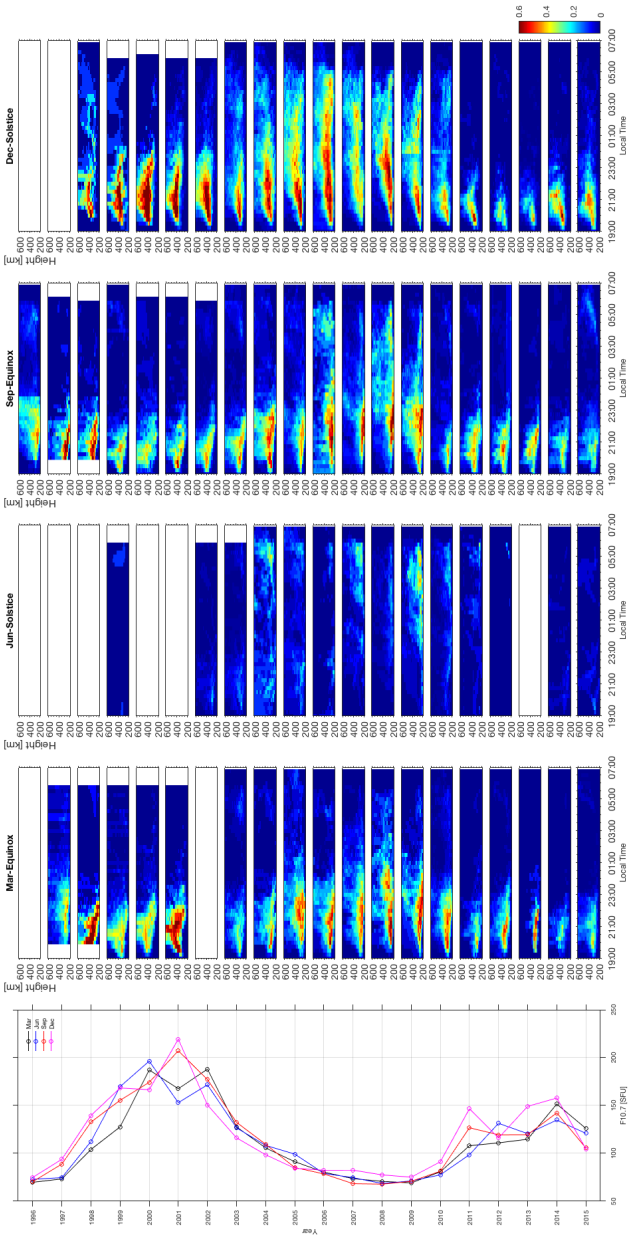

Figure 4.3. Occurrence rates of quiet-time equatorial spread F observed by JULIA between 1996 and 2015. Only seasons with at least 10 days of observations are shown. The bottom panel shows the variation of the average F10.7 index for each year. Curves show the four different seasons: March Equinox, June Solstice, September Equinox, and December Solstice. The top panels show height versus local time maps of the seasonal occurrence rates of ESF for each year.

of ESF occurrence rates in the post-midnight sector during June and December solstices of the 2008-2009 deep solar minimum, which were linked to unusual upward drifts observed around midnight (*Heelis et al.*, 2010; *Stoneback et al.*, 2011).

The results of our analysis (Figure 4.3) indeed show high occurrence rates of ESF in the post-midnight sector during June solstice 2009. The results also show high occurrence rates of ESF during post-midnight hours in December solstice 2009. This is in agreement with C/NOFS satellite observations. The height-versus-local time maps of ESF occurrence created with JULIA measurements, however, provide additional insights on the origin in local time of post-midnight ESF. During June solstice the ESF occurrence rates during premidnight hours were negligible. This indicates that ESF observed by C/NOFS in the American (Peruvian) sector would not have originated in the post-sunset sector near Jicamarca.

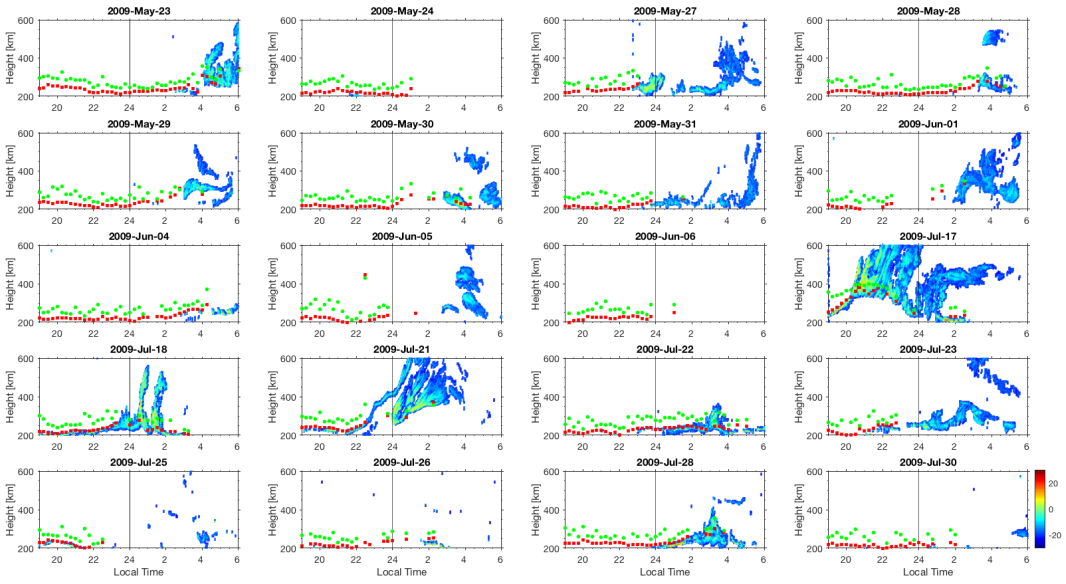

Figure 4.4. Examples of JULIA RTI maps for June solstice 2009. Each panel also shows the variation of h'F (red markers) and hmF2 (green markers) measured by a collocated digisonde.

In order to provide more information about the ESF events observed by JULIA during June solstice 2009, we show 20 RTI maps of full-night observations made during that period

in Figure 4.4. Along with the RTI maps we also provide variations in the height of the F-region peak (hmF2) and in the virtual height of the F-region base (h'F) as measured by a local digisonde.

The radar observations in Figure 4.4 serve to illustrate and confirm that the overwhelming majority of ESF events were first detected in the post-midnight sector. Only one post-sunset ESF event (on July 17) was observed during June solstice 2009. Most of the post-midnight events were observed well after midnight (after 02:00 LT) and could have been the product of upward drifts around midnight as hypothesized by *Stoneback et al.* (2011). This is also in agreement with the results of *Yizengaw et al.* (2013). They used vertical drifts measured by C/NOFS and an assimilative physics-based model of the low-latitude ionosphere - PBMOD (*Retterer et al.*, 2005) to show that the F-region can become unstable in the post-midnight sector during June solstice low solar flux conditions.

On the other hand, one could propose that the observed ESF events could have been generated at an evening sector to the west of the radar site. Under typical ionospheric convection conditions, ESF would then drift to east for several hours where would be detected by JULIA in the post-midnight sector. Assuming development at around 2000 LT, observation by JULIA at 0200 LT and an average zonal plasma drift of 75 m/s, the ESF event would have been originated $\sim 15^{\circ}$ in longitude to the west of Jicamarca.

To better understand the underlying F-region behavior over Jicamarca and potential conditions leading to ESF generation, we also investigated temporal variations in the h'F and hmF2 parameters measured by the Jicamarca digisonde. The digisonde parameters are also shown in Figure 4.4. These parameters do indicate that the layer is lifted, though modestly, prior to the appearance of ESF in most days. The RTI maps for May 23 and July 18 and 28 show, perhaps, some of the most clear examples of the apparent F-region uplifts prior to ESF development during geomagnetically quiet conditions. The uplift associated with the severe ESF event of July 21 occurred during geomagnetically disturbed conditions.

The observations indicate that under extreme conditions of atmospheric contraction of the 2008-2009 solar minimum, apparent uplifts could have led to destabilization of the F-region layer and ESF generation.

Therefore, the RTI maps in Figure 4.4 reinforce our inference from the climatology in Figure 4.3, that is, a predominant occurrence of post-midnight ESF events in June solstice 2009. More importantly, the RTI maps also indicate that the ESF events over Jicamarca were not generated during post-sunset hours in that longitude sector. Collocated digisonde observations provide additional evidence that the post-midnight events were associated with apparent F-region uplifts. Unfortunately, the measurements available do not allow us to determine the source of the observed uplifts. Some of the observed uplifts could result from the unusual, quiet-time midnight vertical drifts measured by C/NOFS during the 2008-2009 solar minimum driven, presumably, by semi-diurnal tides. *Yizengaw et al.* (2013) also summarized that post-midnight upward drifts could be driven by atmospheric gravity waves, traveling ionospheric disturbances, and by electric fields associated with off-equatorial sporadic-E layers. It is also possible that the apparent uplifts are a result of weakening downward drifts as proposed by *Nicolls et al.* (2006) and recently investigated by *Ajith et al.* (2016) and *Zhan and Rodrigues* (2018) with measurements and modeling parameters for the Indonesian and American sector, respectively.

We now turn our attention to observations made during December solstice under the extreme low solar flux conditions. Figure 4.5 shows 20 RTI maps of full-night observations during December solstice 2009. Again, we also show the variations in h'F and hmF2 measured by the Jicamarca digisonde. As indicated by the climatological results of Figure 4.3, an overwhelming number of ESF events during that period start during post-sunset hours. ESF behavior in December follows the expected pattern for typical ESF events. The events start in the post-sunset sector as bottom-type or bottomside layers, and then give place to fully developed (topside) layers later on. The ESF events slowly gain altitude and reach LEO altitudes (say 400 km) typically after 22:00 LT.

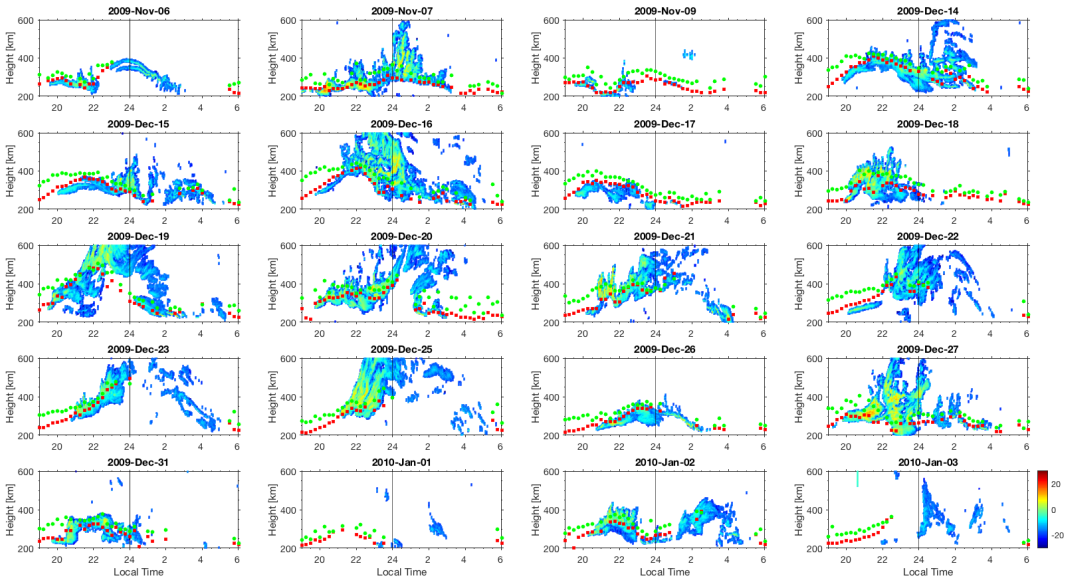

Figure 4.5. Examples of JULIA RTI maps for December solstice 2009. Each panel also shows the variation of h'F (red markers) and hmF2 (green markers) measured by a collocated digisonde.

Unlike June solstice, the layer starts to rise around 1900 LT. In several cases, h'F and hmF2 reach their maximum excursion between 2100 and 2300 LT as a result of the expected variation in the vertical plasma drifts (PRE). The rise of the layer destabilizes the F-region producing post-sunset ESF. In a few other cases, however, the layer is observed to rise until midnight. This midnight rise can be more clearly seen on December 21, 22, 23, and 25. During those days, we hypothesize that the increases in F-region height could be the manifestation of the midnight upward drifts observed by C/NOFS. They would provide favorable conditions (elevated F layer) for ESF development throughout midnight.

More importantly, the RTI maps in Figure 4.5 serve to confirm our initial inference (from Figure 4.3) that December Solstice ESF events start in the post-sunset sector but most of them only reach the topside (or satellite altitudes) around midnight.

4.4 Conclusions

We used coherent backscatter radar (JULIA) measurements made at the Jicamarca Radio Observatory (11.95°S, 76.87°W, ∼1° dip lat) to better understand the origin, in local time, of irregularities observed by C/NOFS. We produce height-versus-local time maps of the occurrence rates of ESF as a function of season for each year between 1996 and 2015. These maps quantify the seasonal variability of ESF and the response of ESF morphology to solar flux conditions.

Of particular importance to this study is a better understanding of ESF occurrence and development during the deep solar minimum of 2008-2009, when sensors on the C/NOFS satellite showed an unexpected predominance of equatorial spread F (ESF) events in the post-midnight sector (*Heelis et al.*, 2010). It has been suggested that these events might have been driven by the unusual behavior of the equatorial plasma drifts, which showed an abnormal upward peak around midnight during the same period (*Stoneback et al.*, 2011).

JULIA observations for June solstice 2009 showed an overwhelming dominance of ESF events that started around midnight or later. Collocated digisonde measurements confirm the absence of favorable conditions for post-sunset ESF development during that period near the Jicamarca site (American Peruvian sector). More importantly, the digisonde observations showed apparent F-region uplifts preceding the appearance of post-midnight ESF structures. We hypothesize that these uplifts contribute to destabilization of the F-region and generation of post-midnight ESF. The set of observations available for this study does not allow us to determine the exact source (or sources) of the apparent uplifts.

JULIA observations for December solstice 2009, on the other hand, showed that ESF events and conditions for their development started in the post-sunset sector and continued through midnight. Digisonde observations indicate contributions from the well-known PRE and, in at least some cases, from apparent uplifts that continued until midnight. We interpret these uplifts as signatures of the abnormal drifts detected by C/NOFS.

The increased occurrence rate of post-midnight ESF seen by C/NOFS can be explained by the height coverage of the satellite. In general, ESF structures only reaches the topside (and satellite altitudes) after 22:00 LT (Figure 4.5), and showed significant occurrence rates around midnight (Figure 4.3).

CHAPTER 5

MELISSA: SYSTEM DESCRIPTION AND SPECTRAL FEATURES OF PRE- AND POST-MIDNIGHT F-REGION ECHOES[1]

Authors – Fabiano S. Rodrigues, Weijia Zhan, Marco A. Milla, Bela G. Fejer, Eurico R. de Paula, Acacio C. Neto, Angela M. Santos, and Inez S. Batista

W. B. Hanson Center for Space Sciences, MS/WT15

The University of Texas at Dallas

800 West Campbell Road

Richardson, Texas 75080-3021

Corresponding author: Fabiano S. Rodrigues

[1]Accepted for publication in Journal of Geophysics Research: Space Physics. Copyright (2019) American Geophysical Union. Further reproduction or electronic distribution is not permitted.

5.1 Introduction

Equatorial spread F (ESF) is the general name often used when referring to the manifestation of electron density irregularities in the low-latitude ionosphere. ESF was first observed as diffuse radio echoes from the ionospheric F layer in the equatorial region (*Booker and Wells*, 1938). Since then, it has been studied theoretically and experimentally using different types of techniques (e.g. *Woodman*, 2009). Study of ESF is motivated by a better understanding of fundamental physical processes in the ionosphere-thermosphere (IT) system at low latitudes (e.g. *Abdu*, 2016). The study of ESF is also motivated by the impact of ESF irregularities on the performance of radio-based systems used for communication, navigation and remote sensing (e.g. *Basu et al.*, 1988; *Kintner et al.*, 2007; *Carrano et al.*, 2012).

It is well recognized that the so-called Generalized Rayleigh-Taylor (GRT) instability is responsible for plasma structuring and ESF (*Zalesak et al.*, 1982; *Sultan*, 1996). More recently, however, the collisional shear instability (CSI) was also proposed to play a role in ESF development and morphology (e.g. *Aveiro and Hysell*, 2010). The vertical plasma drift is one of the main drivers of the GRT instability, and the pre-reversal enhancement (PRE) of the drifts near sunset can explain most of the climatological features in ESF, including its high occurrence rate in the evening sector (*Fejer et al.*, 1999; *Huang and Hairston*, 2015; *Smith et al*, 2016). Current research has focused on better understanding the sources of day-to-day variability in ESF development, including the sources of seed waves required for underlying instabilities (*Tsunoda et al.*, 2010; *Kherani et al.*, 2012; *Abdu*, 2019). Another topic of current interest is related to better understanding of ESF events observed in the post-midnight sector (*Candido et al.*, 2011; *Yizengaw et al.*, 2013; *Otsuka et al.*, 2018).

Significant advances in our understanding of ESF have come from incoherent and coherent backscatter radar observations made at the Jicamarca Radio Observatory (JRO) located near Lima, Peru in the western American sector (e.g. *Woodman and La Hoz*, 1976; *Hysell and Burcham*, 2002). Coherent scatter radar (CSR) observations, in particular, have a number of

advantages over other techniques for studies of F-region irregularities. Conventional, single-antenna CSR observations allows us to determine the height profile of ESF irregularities as a function of time. Conventional CSR observations also provide information about the Doppler velocity of the irregularities responsible for the echoes. Observations made with multiple antenna baselines and interferometric techniques can provide high resolution (in time and space) information about the two-dimensional (height versus zonal distance) distribution of irregularities within the radar field-of-view (e.g. *Hysell and Chau*, 2006; *Harding and Milla*, 2015; *Rodrigues et al.*, 2017).

The success of the observations at Jicamarca led to the use of existing radar systems for ionospheric irregularity observations and to the deployment of new radar systems at various longitude sectors. For instance, *Tsunoda et al.* (1979) used a high-power, tracking radar (ALTAIR) located at the Kwajalein Atoll in the Marshal Islands (8.8° N, 167.5° E) to observe and study the evolution of ESF structures. The Middle and Upper atmosphere (MU) radar in Japan (34.8° N, 136.1° E) was also used for ionospheric studies and produced the first VHF radar observations of mid-latitude F-region irregularities (*Fukao et al.*, 1988). In the Indian sector, the Gadanki MST radar (13.5° N, 79.2° E) was used to observe F-region irregularities associated with ESF (e.g. *Patra et al.*, 1995). More recently, smaller radar systems have been deployed for dedicated ionospheric studies. For instance, *Otsuka et al.* (2009) reported results of continuous observations of F-region irregularities made by a 20-kW peak-power VHF radar system deployed in Kototabang (0.2° S, 100.3° E) in Indonesia. *Ning et al.* (2012) also reported the first observations of ionospheric irregularities made by a 24-kW peak power ionospheric radar deployed in Sanya, China (18.4° N, 109.6° E).

In the American sector radar observations were limited to Jicamarca (11.95° S, 76.87°W) for several decades. The 1994 NASA Guará rocket campaign led to temporary deployment and observations made with the 50 MHz CUPRI radar near the Alcantara rocket launching base (2.3° S, 44.4° W) in Brazil (*Swartz and Woodman*, 1998). In the late 1990s, the RESCO

50 MHz radar started operations but only made observations of E-region irregularities (*Abdu et al.*, 2002). In 2001, the FAPESP-Clemson-INPE (FCI) 30 MHz radar was deployed and was capable of observing E- as well as F-region irregularities including those associated with 150-km echoes (*de Paula and Hysell*, 2004).

While the FCI radar was capable of making observations of F-region echoes in the Brazilian sector, the observations were mostly limited to pre-midnight hours due to technical reasons. In 2014, an upgrade of the radar system was carried out, which allowed full-night observations and proper acquisition of the raw voltages for posterior analyses. The new system is referred to as Measurements of Equatorial and Low-latitude Ionospheric irregularities over São Luís , South America (MELISSA). In this chapter, we provide a description of the system and present and discuss results of ESF observations made by this radar, including those made during post-midnight hours. Additionally, we determine the spectral features of ESF echoes, which had not been investigated in previous radar observations in São Luís. More specifically, we compare the spectral features of post-midnight irregularity events with those of typical, pre-midnight ESF. We investigate the usefulness of the spectral features in distinguishing echoes caused by old ("fossil") F-region structures from those associated with new ("fresh") events, that is, structures generated near the radar site and around the time of the observations.

This chapter is organized as follows: In section 2 we describe the MELISSA radar system and the mode used for F-region observations. In section 3, we present examples of observations and discuss the main results of our analysis of pre- and post-midnight F-region echoes detected by MELISSA. Finally, in section 4, we summarize the main results and findings of this study.

5.2 Instrumentation, Observations and Analysis

5.2.1 Instrumentation: MELISSA

The Measurements of Equatorial and Low-latitude Irregularities over São Luís in South America (MELISSA) is a small, low-power 30 MHz coherent backscatter radar system deployed in São Luís , Brazil (2.59°S, 44.21°W, 3.25°S dip latitude). The design, deployment, and operation of this system is a scientific collaboration between the University of Texas at Dallas (UTD), the Brazilian National Institute for Space Research (INPE) and the Jicamarca Radio Observatory (JRO) in Peru. Figure 5.1 shows a map of South America and the location of São Luís. The isolines indicate the magnetic inclination of the geomagnetic field at 350 km altitude for March 2014. The location of Jicamarca Radio Observatory is also indicated for reference.

The receiver of the MELISSA radar is formed by a digital acquisition system, a radar controller, and a DDS (direct digital synthesizer), which were developed at Jicamarca. MELISSA also uses a 16 kW peak power, dual output solid-state transmitter, which was designed and developed by ATRAD atmospheric radar systems. The transmitter allows a maximum duty cycle of 10%. The nominal operating frequency of the system is 29.795 MHz. MELISSA used the same antenna system deployed for the FCI radar system previously deployed in São Luís (*de Paula and Hysell*, 2004). The antenna system is formed by four independent sets of antenna modules (or arrays) aligned in the zonal magnetic direction. Each module is formed by a 4×4 array of Yagi antennas. The HPBW (half-power beam width) of each module is approximately 16° in both EW (east-west) and NS (north-south) directions. Two modules are used for transmission while all the four modules are used for reception.

Having the four antenna arrays in full operation allowed interferometric imaging analyses to be done (*Rodrigues et al.*, 2008). Unfortunately, for the period between 2014 and 2018, one and sometimes two antenna arrays were not operating due to technical issues. In this

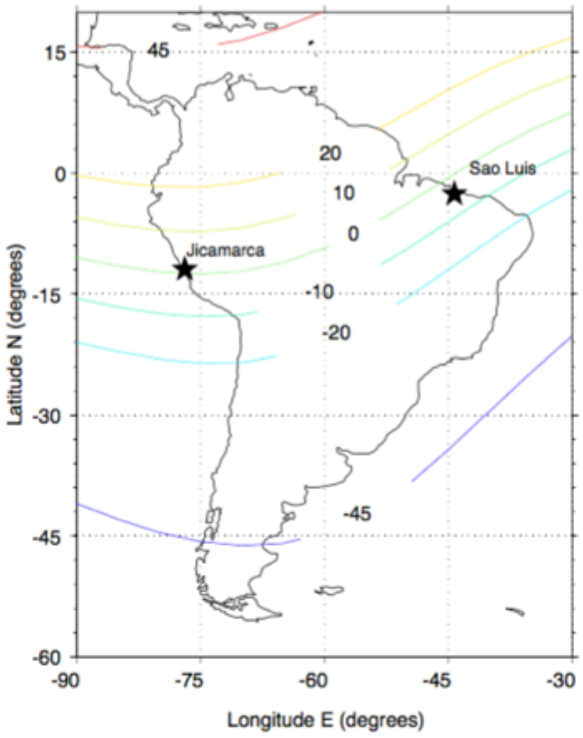

Figure 5.1. Map of South America showing the location of the São Luís site where the MELISSA radar system is located. The location of the Jicamarca Radio Observatory is also shown for reference.

study, measurements from only one of the four antenna arrays are used. The study focuses on estimating the SNR (signal-to-noise ratio) of the echoes and identifying F-region irregularities associated with ESF. We also focus on estimating Doppler spectra for the measured echoes.

The main radar parameters used for F-region observations and analysis are listed in Table 5.1. Typically, the F-region mode started around sunset hours ($\sim$ 18:00 LT) and continued to make observations until morning the next day ($\sim$ 08:00 LT) for most weekdays. Gaps in the observations were caused by power outages, technical issues with the radar, and lack of operators.

Table 5.1. Radar parameters for the F-region observation mode used by MELISSA.

Frequency	30 MHz
Peak Power	16 kW
IPP	1401.6 km
Code	28-bit
Baud length	2.4 km
Coherent integration	None
Number of FFT points	64
Number of FFT spectra averaged	25
Doppler Velocity	[-267 267] m/s

5.2.2 Observations

Figure 5.2 shows an example of F-region observations made by MELISSA on March 22, 2014. It shows the Range-Time-Intensity (RTI) map of the observed echoes. This example serves to illustrate the coverage of the observations for one day, and the typical behavior of F-region echoes associated with a post-sunset equatorial spread F (ESF) event. No echoes were observed in the post-midnight sector (00:00 - 08:00 LT) on this day. Cases of post-midnight echoes will be shown and discussed later on.

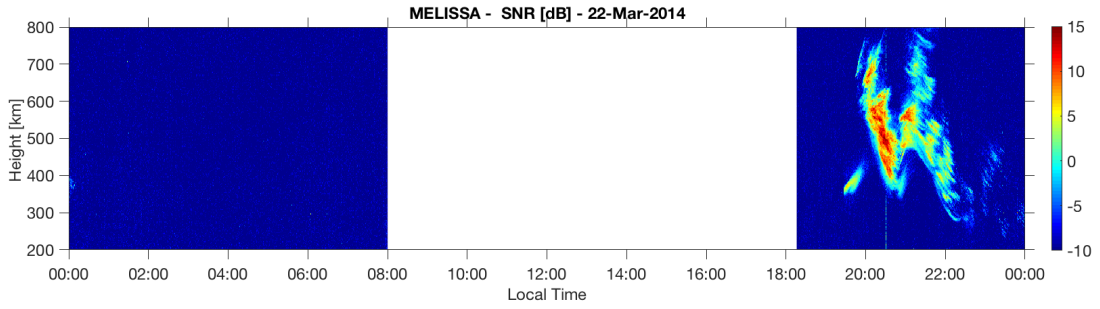

Figure 5.2. Range-Time-Intensity (RTI) showing an example of F-region observations made by MELISSA on March 22, 2014. The RTI map shows that F-region irregularities were not detected in the early nighttime hours (00:00-08:00 LT) but were observed in the post-sunset hours (18:00 - 24:00 LT).

We have also created and examined the RTI maps for all the observations made between 2014 and 2018. Table 5.2 provides an overview of the number of observations made

since 2014, and the number of observations when F-region echoes were visually identified in the RTI maps. Only cases when full pre-midnight (or full post-midnight) observations were available were considered for Table 5.2. The seasons are defined as March Equinox (February-April), June solstice (May-July), September Equinox (August-October), and December Solstice (November-January). For each season, we indicate the number of observations made during pre- and post-midnight hours. We also indicate the number of cases when F-region echoes were detected in each local time sector.

Table 5.2 shows that observations were not made continuously nor uniformly throughout all the seasons. This is, in most part, due to technical difficulties in the operation of the system, which requires human intervention, and the occurrence of power outages. Nevertheless, it can be seen that pre-midnight F-region echoes occur with significant occurrence rates during Equinox and during December Solstice, which is the ESF season in Brazil (*Sobral et al.*, 2002). A significant number of observations were made in June solstice but only a limited number of F-region echo events were identified in the RTI maps.

For the present study, we limit our spectral analyses to observations made during December Solstice 2015 when a significant number of both pre- and post-midnight ESF radar events were identified. Figure 5.3 presents RTI maps showing ESF irregularities observed during the selected period. The RTI maps on the left hand side column show examples of quiet-time pre-midnight events. To illustrate the behavior of typical ESF events, we only show cases when the geomagnetic Kp index did not exceed 3 for the day in consideration. The RTI maps on the right hand side column show all the post-midnight ESF events observed during Fall 2015.

5.2.3 Spectral Analysis

We focus on determining features of the Doppler spectra of F-region echoes associated with pre- and post-midnight ESF observed by the 30 MHz MELISSA system. In order to analyze

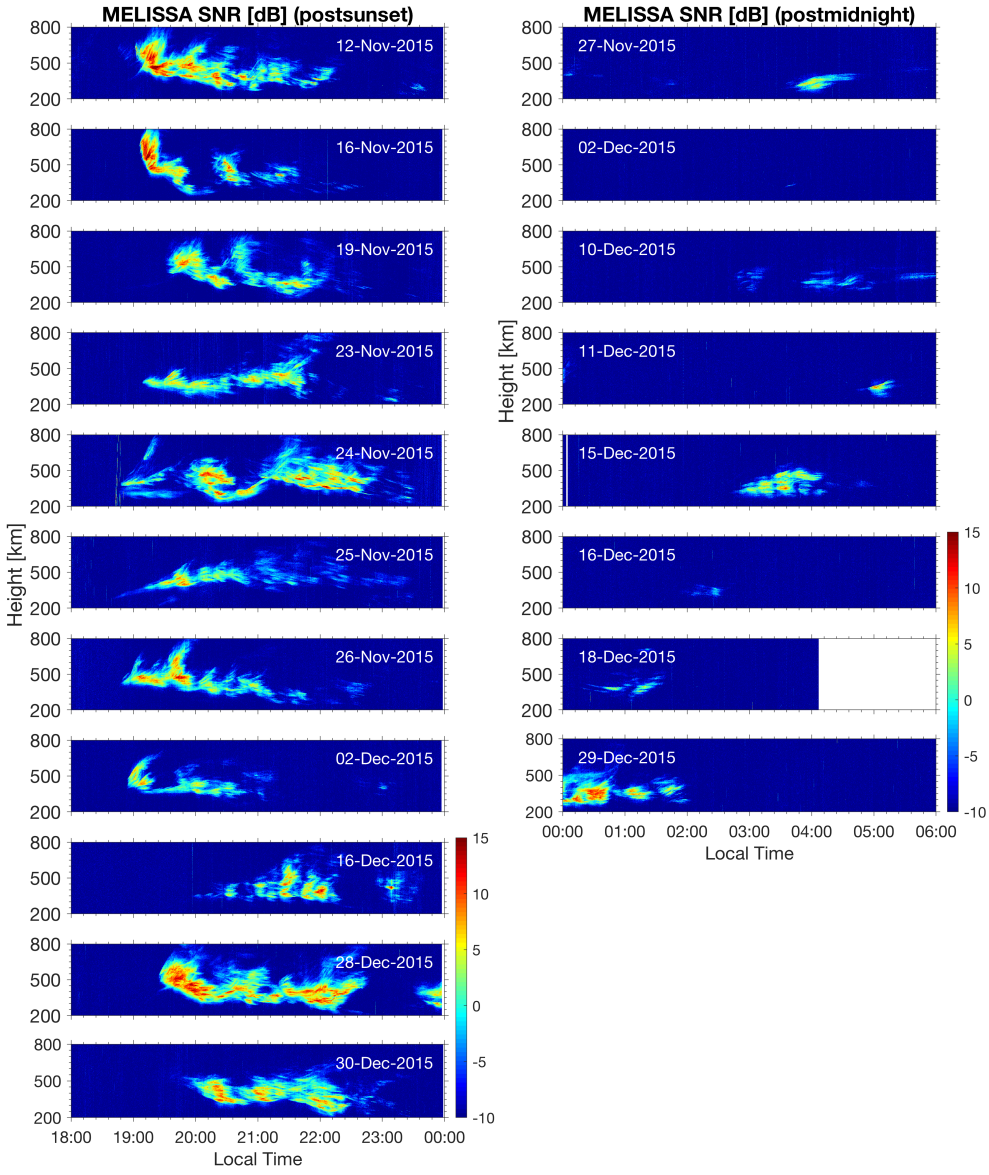

Figure 5.3. The panels on the left hand side show examples of RTI maps of post-sunset ESF events observed by MELISSA during December Solstice 2015. The panels on right hand side show the post-midnight events observed by MELISSA.

Table 5.2. Summary of the F-region observations made by MELISSA between 2014 and 2018. The observations are grouped into seasons. Each season is sub-divided into PRE- and POST-midnight observations. The first value in each group indicates the total number of observations, while the value in parentheses indicates the number of observations where echoes were identified. Finally, N/A indicates that observations were not available.

Year	Mar. Equinox		Jun. Solstice		Sep. Equinox		Dec. Solstice	
	PRE	POST	PRE	POST	PRE	POST	PRE	POST
2014	20(19)	18(4)	22(8)	19(1)	8(2)	4(0)	N/A	N/A
2015	6(5)	7(0)	21(2)	27(1)	35(20)	36(2)	26(25)	25(8)
2016	23(16)	24(0)	38(6)	37(0)	46(27)	46(11)	15(14)	16(9)
2017	N/A	1(1)	N/A	N/A	26(14)	30(10)	21(17)	21(5)
2018	12(5)	12(3)	26(1)	20(0)	26(10)	24(6)	3(3)	5(4)

the features of the spectra, we determined two main parameters: the mean Doppler velocity ($\hat{v}$) and the mean spectral width (σ_v). These two spectral features are commonly used as indicators of the mean velocity and level of turbulence of the ionospheric irregularities within the volume illuminated by the radar (*Woodman*, 1985; *Patra at al.*, 1997; *Hysell and Burcham*, 2002).

Doppler velocity spectra are obtained from the observed complex voltages using the FFT (Fast Fourier Transform) algorithm. As listed in Table 5.1, 64 points are used in the FFT estimates. Therefore, unaliased Doppler spectra with velocities between -267 and +267 m/s are obtained. Then, 25 Doppler spectra are averaged leading to a mean Doppler spectra every ∼15 seconds. Finally, the mean spectral velocity and width are obtained by least-square fitting a Gaussian model to the measured spectra.

5.3 Results and Discussion

We now present additional details of the observations made by the MELISSA system. As mentioned earlier, we focus on presenting and discussing the spectral features of F-region echoes observed in the pre- and post-midnight sector.

We start by presenting and discussing an example that illustrates the behavior of the F-region echoes observed during a typical post-sunset ESF event (Figure 5.4) followed by examples of post-midnight events (Figures 5.5 - 5.8). We present and discuss the spectral features seen on three distinct types of post-midnight echo signatures identified in the RTI maps of December Solstice 2015 (see Figure 5.3). The RTI maps of the selected post-midnight examples represent the following cases: (a) F-region echoes detected near midnight (Figure 5.5). (b) Strong echoes detected in the post-midnight sector (Figures 5.6 and 5.7). The intensity of those echoes would suggest the detection of a new ("fresh") ESF event. Finally, we also show an example of (c) weak echoes detected during post-midnight hours (Figure 5.8). The weak echoes would suggest the detection of an old ("'fossil") ESF event.

Also, in order to aid our presentation and discussion of the post-midnight observations we evaluated the behavior of the F-region over the radar site using collocated observations made by a digisonde. The variation of the virtual height of the F-layer base (h'F) and true height of the F-region peak (hmF2) are shown in Figure 5.9 for the example days of post-midnight ESF. The digisonde parameters are superimposed to the RTI maps.

5.3.1 Pre-midnight F-region echoes

Figure 5.4 shows the first example of results obtained with our spectral analyses. It illustrates how the overall behavior of the spectra, observed during a typical post-sunset (pre-midnight) ESF event, varies with time. The top panel shows the RTI map, from 18:00 LT to 24:00 LT, for the measurements made on the evening of December 02, 2015 when the event was detected. Echoes from four stages (times) of the ESF event have been selected based on the RTI map. The time and height for each of these selections is indicated as markers (red stars) on the RTI map. Note that the selected heights were chosen based on echo intensity. Echoes with low SNR are too noisy for spectral analyses.

The first selection comes from a topside scattering layer (plume) observed around 19:00 LT. The second selection comes from what seems to be a second, smaller plume detected

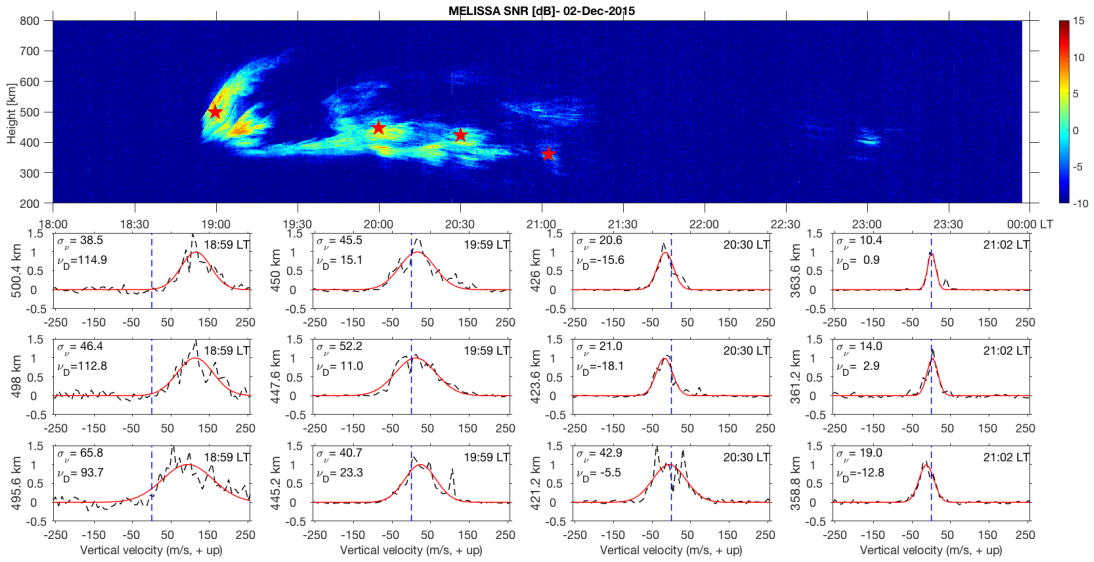

Figure 5.4. Top panel: Range-Time-Intensity (RTI) map of F-region echoes observed on December 2, 2015. Bottom panels: Each column shows examples of spectra observed at four different times during the irregularity event shown in the RTI map. Examples from three consecutive range gates are shown for each time. Times and heights are indicated in each panel, and by markers (red stars) in the RTI map. Estimated mean Doppler velocities (v_D) and spectral widths (σ_v) are also provided in each panel (in m/s).

around 2000 LT. The third selection comes from a third, late-night scattering structure observed around 20:30 LT. Finally, the fourth selection comes from the last bottomside echoes observed around 21:05 LT .

Below the RTI map, each column of panels shows three Doppler spectra for the selected regions described above. Doppler spectra for consecutive range gates are shown. The range gate heights are indicated on the left hand side of each panel. The convention for the plots is that positive velocities indicate irregularities moving away from the radar (upward direction). The black dashed curves are the measured Doppler velocity spectra and the red solid curves are the best-fit model results. The main parameters, mean Doppler velocity (v_D) and spectral width (σ_v) obtained from the fit routine are also indicated in each panel.

Figure 5.4 shows that echoes from the early evening plume have broad spectral widths and positive (upward) Doppler velocities. For the selected plume echoes, the widths vary

between 38.5 and 65.8 m/s, and the mean velocities vary between 93.7 and 114.9 m/s. The spectral features vary noticeably from range-gate to range-gate, and suggest a turbulent, upward flow of irregularities, which would be expected from the early, developing phase of ESF structures.

In our analyses of the spectra, we did not identify cases that could be affected by frequency aliasing, that is mean Doppler velocities that would exceed $\sim$ 267 m/s. We found, however, cases where the Doppler spectrum does not follow the shape of a single Gaussian function. It has, instead, multiple peaks similar to observations made at Jicamarca (*Woodman and La Hoz*, 1976).

The second selection (second column of spectra) comes from a region of echoes that seemed to be caused by the passage of a second radar plume. In this case, however, the echoes have spectral widths that are comparable to or somewhat narrower than those observed during the first plume. The echoes continue to have positive mean Doppler velocities but with smaller amplitudes than those observed in the first case. The spectral widths now vary between 40.7 and 52.2 m/s and the mean Doppler velocities vary between 11.0 and 23.3 m/s. The spectral features suggest the occurrence of a plume outside its main phase of development, older than the first plume but still evolving.

The third selection (third column of spectra) was from a echoing structure that is not as developed vertically as the first two cases. In this case the spectral widths of the echoes are much narrower than those observed in the first plume, and the mean Doppler velocities are now negative indicating a downward mean flow of irregularities. The spectral widths vary between 21.0 and 42.9 m/s and the mean Doppler velocities vary between -5.5 and -18.1 m/s. We interpret the spectral features as being those of a decaying ESF structure originated much earlier, presumably, to the west of the observation site.

Finally, the last selection of echoes (fourth column of spectra) show spectra that are, in general, very narrow and with negligible or negative (downward) mean Doppler velocities.

Spectral widths vary between 10.4 and 19.0 m/s and the mean Doppler velocities vary between 2.9 and -26.7 m/s. The spectral widths indicate reduced levels of turbulence. The occurrence of weak and negative mean Doppler velocities are interpreted as indicators of the background plasma flow, which is expected to be weak or downward around those times. Again, we associated these echoes to late-night, decaying ESF structures.

5.3.2 Post-midnight F-region echoes

We now turn our attention to spectral features of F-region echoes observed in the post-midnight sector. As mentioned earlier, we selected a few cases that illustrate three different types of echoing layers detected during Dec. Solstice 2015.

Near midnight F-region irregularities

Figure 5.5 shows an example of post-midnight echoes that seemed to be the result of an ESF event that started in the pre-midnight sector and continued throughout midnight. Data presentation follows the same format of Figure 5.4. The post-midnight event was observed by MELISSA on December 29, 2015. Looking at Figure 5.3, we can see MELISSA observations for December 28 as well. These observations show that F-region echoes started to be observed around 19:30 LT on Dec. 28, and ended at about 22:45 LT. Then, they started again around 23:30 LT and continued throughout midnight producing the post-midnight echoes seen on Dec. 29 (Figure 5.5).

Similar to Figure 5.4, the bottom panels of Figure 5.5 show the spectra of echoes selected from different times. The first two selections come from the region of intense echoes observed around 00:15 LT and 00:30 LT. The spectra show echoes with somewhat broad widths, between 27 and 37 m/s, and with small mean Doppler velocities. The spectra are broader than those of echoes observed late in the evening during typical ESF events. The spectral features combined with the intensity of the echoes (SNR $\sim$ 10 dB) indicate that the structures

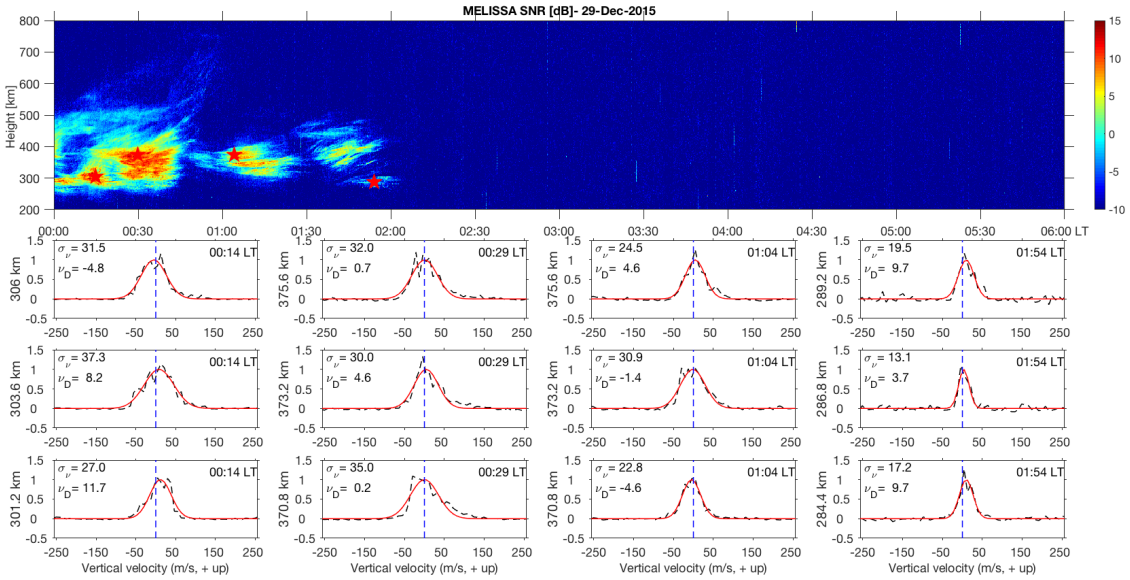

Figure 5.5. Same as Figure 5.4 but for December 29, 2015.

have recently developed. They resemble, for instance, the echoes observed around 20:00 LT in our first example of pre-midnight ESF (Figure 5.4).

The last two columns of spectra in Figure 5.5 show examples of echoes seen later at night, around 01:00 LT and 02:00 LT, respectively. Around 01:00 LT, echoes with moderate intensity are still observed but the spectra has narrower widths than what was observed earlier. The mean Doppler velocities continue to be small. Around 02:00 LT, the echoes are weak and suggest the occurrence of fossil structures, which were created much earlier. The spectra (last column) show very narrow echoes, with spectral widths that are similar to those associated with decaying pre-midnight ESF (see Figure 5.4, fourth column of spectra). However, unlike the pre-midnight case, the mean Doppler velocities are near zero suggesting weak vertical background plasma drifts.

The digisonde data for this event, shown in Figure 5.9(a), supports the idea of destabilizing conditions around midnight, which could have led to a "fresh" ESF structure and the radar echoes seen around midnight. The digisonde data (h'F) shows an apparent uplift of the F-layer starting around 23:00 LT on Dec. 28, about 30 minutes before the second

group of late-night echoes start to be observed by MELISSA (see Figure 5.3). The base of the F-layer only descends around 02:00 LT. At that time radar echoes also ceased to be observed.

Strong post-midnight F–region echoes

Figure 5.6 now shows the second type of post-midnight echoes observed by MELISSA. The example is from observations made on December 15, 2015. Unlike the previous case, these post-midnight echoes appear away from the midnight sector. The intensity of the echoes (SNR) suggest that irregularities have recently been generated but, as proposed by this study, the spectral analyses can provide additional evidence of such a scenario.

Again, spectra for four distinct regions of the RTI map are shown in the bottom panels of Figure 5.6. In the first selected region, around the beginning of the event at 03:00 LT, the echoes have moderate spectral widths (20 - 30 m/s) and positive mean Doppler velocities. In the second region, from around 03:30 LT and a more developed echoing layer in the RTI map, the echoes show broader spectral widths ($\sim$ 40 - 50 m/s) and again, positive Doppler velocities. Mean Doppler velocities near 50 m/s can be observed. The last two selections come from the late phases of the event, around 04:00 and 04:05 LT. During that time, the echoes are weak and seemed to come from decaying irregularities. The spectra of these echoes show narrow widths (15 - 30 m/s) and negative (downward) mean Doppler velocities indicating the same conditions of echoes seen in the late phases of post-sunset ESF events.

The spectral features of this event suggest a structure developing over or near the São Luís site in the post-midnight hours. Similar to post-sunset events, the echoes start with positive mean Doppler velocities and broad spectral widths. Then, the late echoes are narrow and show negative Doppler velocities following the expected behavior of the background plasma drifts based on climatological models.

Looking at the digisonde data for this day (Figure 5.9(b)) we can notice, again, an apparent uplift of the F-region starting around 02:00 LT, about 45 minutes before the first

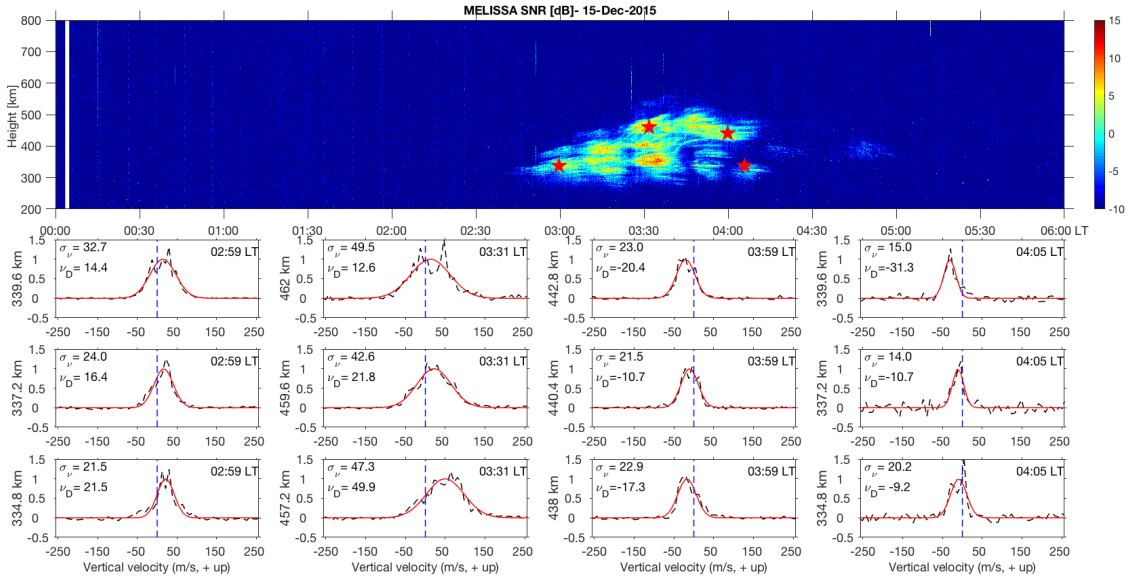

Figure 5.6. Same as Figure 5.4 but for December 15, 2015.

post-midnight echoes are detected. This uplift supports the idea of destabilizing conditions in the post-midnight sector and the generation of new irregularities causing the echoes that start to be seen around 02:45 LT.

Another example of observations showing relatively strong echoes in the post-midnight sector is shown in Figure 5.7. Analyses of the echoes show again cases of wide spectra in at least some of the range gates of the first two selected regions, from around 03:50 and 04:00 LT (first and second columns). The mean Doppler velocities are also positive. Later, around 04:10 and 04:30 LT the echoes are much narrower and with mean Doppler velocities much closer to 0 m/s. Again, the digisonde data (Figure 5.9(c)) shows small, but noticeable increases in h'F and hmF2 starting around 03:00 LT preceding the appearance of the echoes and irregularities by approximately 40 minutes.

Weak post-midnight F-region echoes

Finally, Figure 5.8 shows an example of very weak post-midnight echoes that one would be inclined to associate with fossil ESF structures, that is, with F-region irregularities that

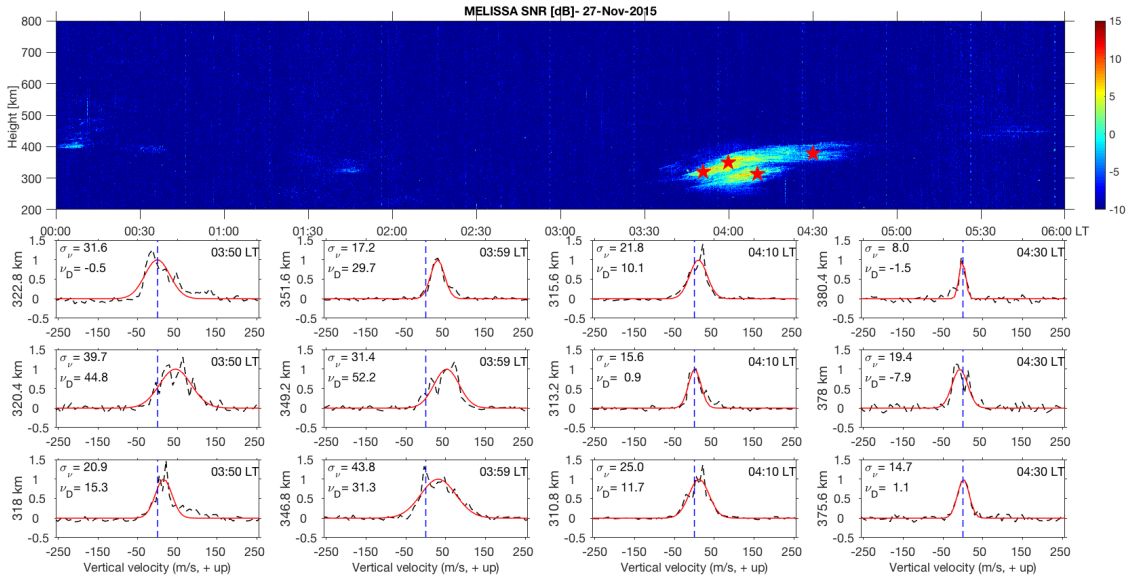

Figure 5.7. Same as Figure 5.4 but for November 27, 2015.

were generated at earlier times and outside the field-of-view of the radar, and that drifted into the field-of-view as they moved zonally with the background plasma. The first echoes start to be observed around 03:00 LT.

Our observations show, however, that the spectral features of the observed echoes do not match those of decaying irregularities, that is, mostly narrow widths and negative Doppler velocities. Instead, a number of the echoes show wide spectral widths (as large as 35.7 m/s) and spectra with positive mean velocities. See the examples of spectra shown in Figure 5.8.

The digisonde data (Figure 5.9(d)) confirms an F-region behavior that might favor the GRT instability growth. The bottomside F-region starts to increase around 01:30 LT, about 90 minutes prior to the appearance of the first echoes. At about 02:45 LT, the layer peak has reached ∼275 km altitude and the first echoes are seen in the RTI map. The layer remains high for the rest of the night, and the echoes continue to be observed.

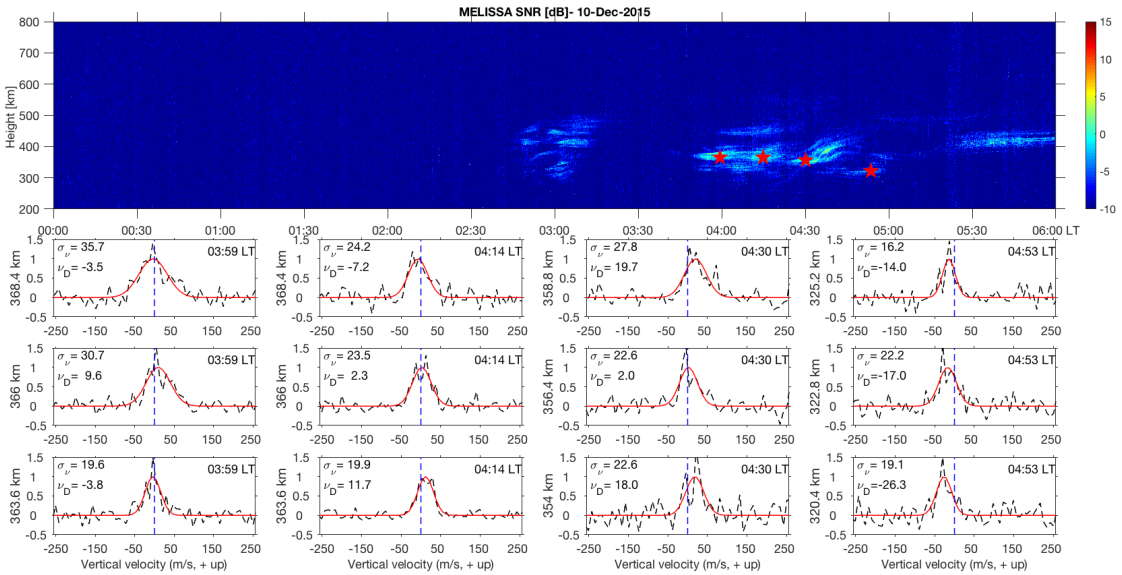

Figure 5.8. Same as Figure 5.4 but for December 10, 2015.

5.3.3 Potential origin of the observed post-midnight uplifts

While not the main goal of this study, we also investigated a potential explanation for the occurrence of the F-region uplifts preceding the post-midnight irregularity events detected by the radar. We looked, particularly, on the role of disturbance electric fields of solar wind-magnetospheric origin.

Disturbances in the equatorial zonal electric fields (vertical $\mathbf{E}\times\mathbf{B}$ drifts) with time scales of a few hours have been attributed to the occurrence of nearly simultaneous enhancements in the electric fields observed at high latitudes (*Fejer*, 1981). These "prompt penetration" electric fields have been shown to oppose the regular pattern of equatorial upward drifts during the day and downward drifts at night. Additionally, large and long-lasting enhancements in the high-latitude electric fields have been observed to affect equatorial vertical drifts as well (*Fejer*, 1991). These high-latitude electric fields drive enhanced currents and Joule heating, which in turn affect the global circulation of thermospheric neutral winds as well as the ionospheric current system at mid- and low-latitudes. As a result, disturbances in the

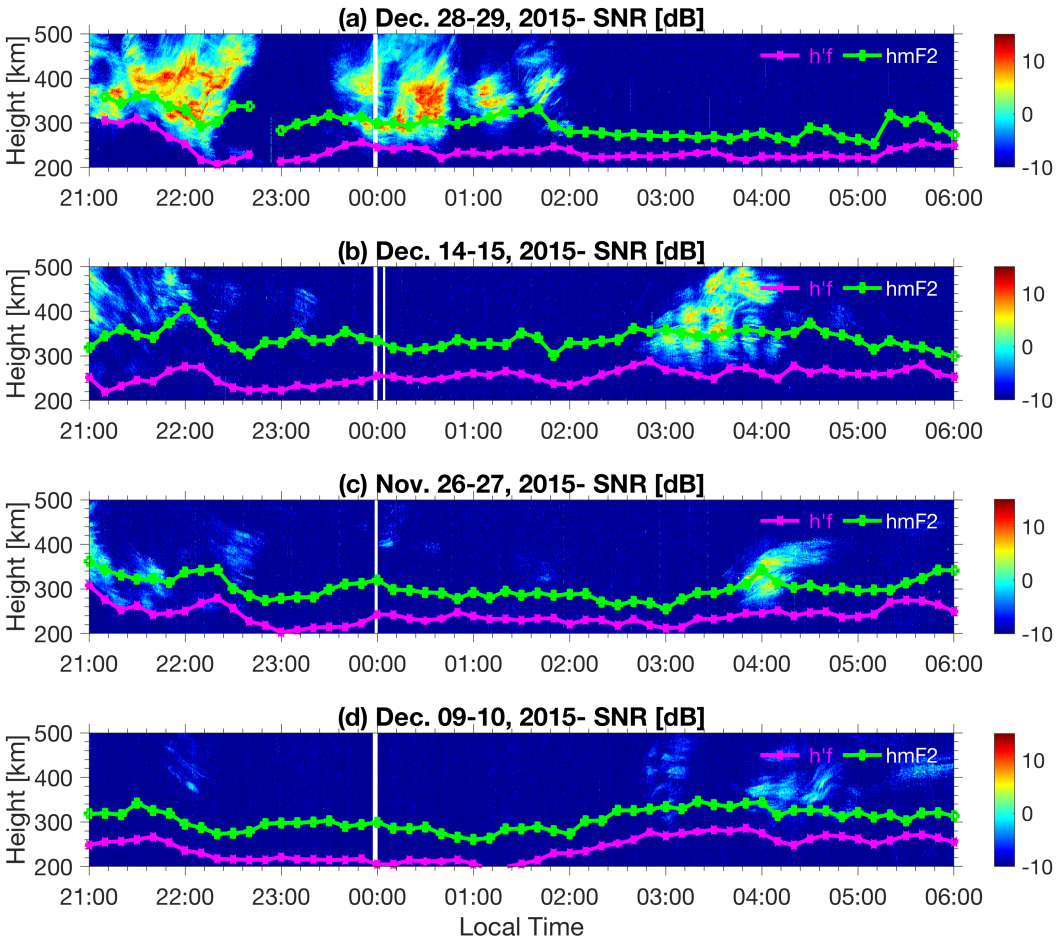

Figure 5.9. The local time variation of h'F and hmF2 for the ESF events discussed in this chapter. The digisonde parameters are superimposed on the RTI map for each case.

equatorial vertical plasma drifts are observed from a few to several hours after the beginning of the high-latitude enhancements.

In our previous study (*Zhan and Rodrigues*, 2018), we focused on the mid-latitude Kp index to isolate geomagnetically quiet days. Here, to investigate the potential of disturbance electric fields, we followed the approach described and used by *Scherliess and Fejer* (1997) and more recently by *Navarro et al.* (2019). In that approach, the auroral electrojet (AE)

index was used as a proxy of the magnitude of the electric fields (and currents) at high latitudes and its time variation has been shown to correlate very well with disturbances in the equatorial drifts.

Figure 5.10 shows the local time variation of the AE index for each example discussed in the previous sections. The most striking feature is that the AE index shows significant high-latitude activity starting several hours prior to the occurrence of all the ESF events except the case when ESF was observed around midnight (top RTI map of Figure 5.10). This suggests the occurrence of significant Joule heating and disturbed dynamo winds that could have contributed to the generation of abnormal equatorial plasma drifts for the cases when irregularities were observed well after midnight.

It has been shown that the disturbed dynamo is very effective in driving upward drifts during nighttime hours, with the largest disturbed vertical drifts occurring around 03:00 LT (*Navarro et al.*, 2019). Then, the expected timing of disturbed drifts driven by high-latitude activity is in good agreement with our observations of post-midnight ESF, which started around 03:00 LT. Therefore, given the observations we are inclined to suggest that the F-region uplifts detected well after midnight were driven by disturbed dynamo electric fields (vertical drifts). Despite being modest at most times, these drifts and F-region uplifts could have created conditions favorable to the GRT instability, and to the development of the observed ESF events. This hypothesis is certainly more plausible during the low solar flux conditions under which our measurements were made. During those conditions the neutral atmosphere is more contracted, and even small uplifts might cause significant changes in the g/ν_{ni} term (where g is the gravitational acceleration and ν_{ni} is the ion-neutral collision frequency) in the linear growth rate of the GRT instability (*Basu*, 2002).

On Dec. 28-29, 2015, when post-midnight echoes started to be detected around midnight, AE index variations were substantially smaller than those observed in the other examples (see Figure 5.10(a)). Nevertheless, the digisonde data (h'F) shows an apparent uplift of

the F-layer starting around 23:00 LT on Dec. 28, about 30 minutes prior to echoes being observed by MELISSA. For this case, we are left to suggest that quiet time variations in the vertical drifts led to destabilizing F-region conditions. An apparent F-region uplift and conditions favorable to the GRT instability growth can be produced, for instance, from weakening vertical drifts as suggested by *Nicolls et al.* (2006). Recent studies provide experimental evidence that weakening drifts can produce apparent uplifts starting in the pre-midnight sector and F-region irregularities during post-midnight hours (*Ajith et al.*, 2016; *Zhan and Rodrigues*, 2018). Additional, concurrent conditions such as those of converging (equatorward) thermospheric winds, however, might also be necessary to create conditions capable of producing significant ESF events (*Zhan and Rodrigues*, 2018).

5.4 Summary

We presented a description of a 30 MHz coherent backscatter radar system that operated in the low-latitude site of São Luís (2.59°S, 44.21°W, 3.25°S dip latitude) in Brazil between March 2014 and December 2018. The system is referred to as Measurements of Equatorial and Low-latitude Ionospheric irregularities over São Luís, South America (MELISSA), and allowed observations of the F-region during pre- and post-midnight hours. The description of the system is followed by a quick summary of F-region measurements and presentation and discussion of observation examples.

We focused on presenting the spectral features of equatorial spread F (ESF) events observed by MELISSA. Despite the operation of the 30 MHz FCI radar in São Luís between 2001 and 2012, observations past local midnight were limited. Additionally, the spectral features of F-region echoes had yet to be presented. We showed examples of echoes observed by MELISSA during December Solstice 2015 when F-region irregularities were observed during pre- and post-midnight hours.

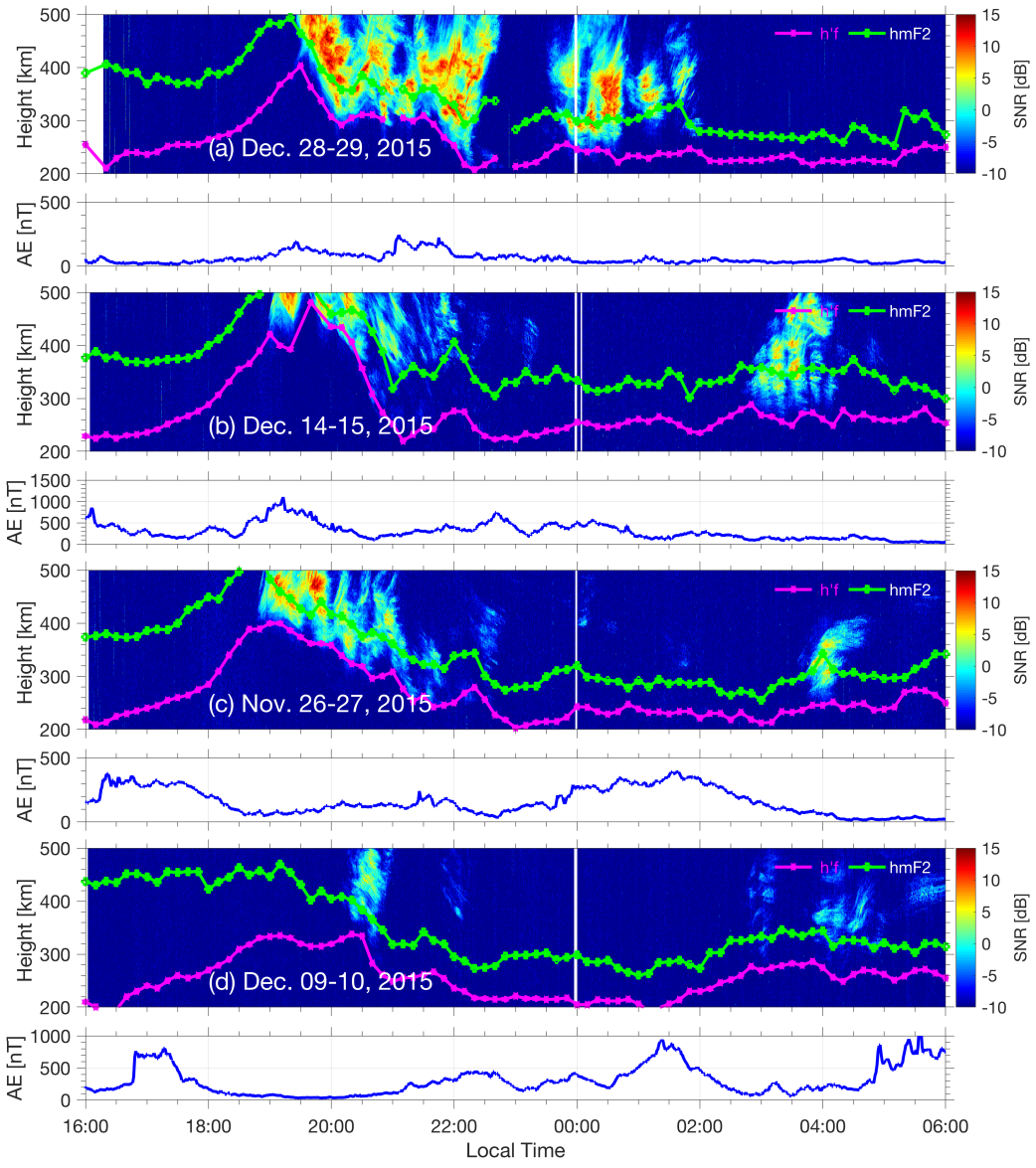

Figure 5.10. RTI maps of the post-midnight events examined in this study. On the RTI maps we also show again the behavior of h'F and hmF2. Below each RTI map we show the behavior of the Auroral Electrojet (AE) geomagnetic index several hours before the beginning of the post-midnight ESF events. Note that the range of the vertical axis for the AE index varies from case to case.

In addition to presenting the main features of the Doppler spectra of the echoes, we also investigated the potential of these features to provide additional information on the local time origin of the irregularities causing the echoes. Conventional (single beam) radar observations have been used to detect the occurrence of post-midnight ESF. While one is inclined to relate weak echoes to decaying irregularity structures, the signal intensity does not permit to determine, unambiguously, if echoes were caused by "fresh" or "fossil" ESF events. In order to better understand the lifetime stage of the observed echoes, we compared the spectral features of post-midnight ESF events to spectral features of typical, post-sunset ESF events. Similar to previous studies (e.g. *Woodman and La Hoz*, 1976), MELISSA observations show spectra that varies significantly from range gate to range gate specially during the early, developing stage of typical ESF events. The echoes are typically wide ($>$ 30 m/s) and with positive mean Doppler velocities. As time progresses and turbulence levels decrease, narrower echoes were observed accompanied by negative mean Doppler velocities.

A comparison of the spectral features of post-midnight echoes with those of post-sunset events suggests that the observed post-midnight F-region irregularities developed outside the evening sector, that is, in the late evening and post-midnight hours. This finding also includes cases where the echoes are weak and that could have been associated with "fossil" ESF events. Collocated digisonde observations support the inference from the radar observations. The digisonde observations indicate modest but noticeable apparent F-region uplifts preceding the ESF events. For most of the cases, the uplifts have been associated with abnormal vertical drifts driven by disturbed dynamo conditions. The observations indicate that during low-solar flux conditions such as those under which the measurements were made, even modest uplifts might create favorable conditions for instability growth and ESF development.

CHAPTER 6

CONCLUSIONS

This dissertation focused on a better understanding of post-midnight ESF in the American sector. More specific topics of study included the role of weakening downward plasma drifts in the generation of postmidnight ESF, the morphology of postmidnight ESF in June and December solstice during the extended solar minimum of 2008-2009, and the spectral features of pre- and post- midnight ESF radar events. Here, we summarize some of the main results of our studies and present suggestions for future work.

6.1 On the role of weakening downward drifts in the generation of postmidnight ESF

In Chapter 3 we showed results related to Jicamarca ISR measurements during a prototypical, quiet-time event observed on June 4-5, 2008 when the downward drifts weakened and a fully developed ESF event was observed. Then, in numerical simulations, SAMI2 reproduced the "apparent" uplift of the ionosphere that was consistent with expectations and observations. Also using SAMI2 simulations, we estimated the flux-tube linear growth rates of the Generalized Rayleigh-Taylor (GRT) instability associated with the weakening drift event. We found that the weakening drifts do produce unstable conditions with positive linear growth rate values. The growth rates, however, were much slower than those obtained for typical, pre-midnight ESF events. The growth rates were also much weaker than those obtained for June solstice, post-midnight hours, under similar equatorial drift conditions in the Indonesian sector (*Ajith et al.*, 2016). Following the hypothesis of *Huba et al.* (2013), we investigated the possibility of wind patterns, departing from climatological predictions, to contribute to the unstable condition responsible for the ESF event observed on June 4-5, 2008. We found that the occurrence of equatorward winds in combination with a weakening drift event, could produce favorable conditions for instability development.

6.2 On the genesis of postmidnight ESF

In Chapter 4 we quantified the seasonal variability of ESF and the response of ESF morphology to solar flux conditions using long-term measurements made by the JULIA radar system. The focus of our analyses was given to the extended 2008-2009 solar minimum.

We found that JULIA observations for June solstice 2009 showed an overwhelming dominance of ESF events that started around midnight or later. Collocated digisonde measurements confirm the absence of favorable conditions for post-sunset ESF development during that period near the Jicamarca site (American Peruvian sector). More importantly, the digisonde observations showed apparent F-region uplifts preceding the appearance of post-midnight ESF structures. We hypothesize that these uplifts even though modest contribute to the destabilization of the F-region and generation of post-midnight ESF.

JULIA observations for December solstice 2009, on the other hand, showed that ESF events and conditions for their development started in the post-sunset sector and continued through midnight. Digisonde observations indicate contributions from the well-known PRE and, in at least some cases, from apparent uplifts that continued until midnight. We interpret these uplifts as signatures of the abnormal drifts detected by C/NOFS.

Lastly, we pointed out that the increased occurrence rate of post-midnight ESF seen by C/NOFS can be explained by the height coverage of the satellite. In general, ESF structures only reaches the topside (and satellite altitudes) after 22:00 LT (Figure 4.5), and showed significant occurrence rates around midnight (Figure 4.3).

6.3 On the spectral features of pre- and post-midnight ESF

In Chapter 5 we presented a description of a 30 MHz coherent backscatter radar system MELISSA that operated in the low-latitude site of São Luís (2.59°S, 44.21°W, 3.25°S dip latitude) in Brazil between March 2014 and December 2018. We focused on presenting the

spectral features of equatorial spread F (ESF) events observed by MELISSA. We showed examples of echoes observed by the system during December Solstice 2015 when F-region irregularities were observed during pre- and post-midnight hours.

In addition to presenting the main features of the Doppler spectra of the echoes, we also investigated the potential of these features to provide additional information on the local time origin of the irregularities causing the echoes. Conventional (single beam) radar observations have been used to detect the occurrence of post-midnight ESF. While one is inclined to relate weak echoes to decaying irregularity structures, the signal intensity alone does not permit to determine, unambiguously, if echoes were caused by "fresh" or "fossil" ESF events. In order to better understand the lifetime stage of the observed echoes, we compared the spectral features of post-midnight ESF events to spectral features of typical, post-sunset ESF events. Similar to previous studies (e.g. *Woodman and La Hoz*, 1976), MELISSA observations show spectra that varies significantly from range gate to range gate specially during the early, developing stage of typical ESF events. The echoes are typically wide (> 30 m/s) and with positive mean Doppler velocities. As time progresses and turbulence levels decrease, narrower echoes were observed accompanied by negative mean Doppler velocities.

A comparison of the spectral features of post-midnight echoes with those of post-sunset events suggests that the observed post-midnight F-region irregularities developed outside the evening sector, that is, in the late evening and post-midnight hours. This finding also includes cases where the echoes are weak and that could have been associated with "fossil" ESF events. Collocated digisonde observations support the inference from the radar observations. The digisonde observations indicate modest but noticeable apparent F-region uplifts preceding the ESF events. For most of the cases, the uplifts have been associated with abnormal vertical drifts driven by disturbed dynamo conditions. The observations indicate that during low-solar flux conditions such as those under which the measurements were made, even modest uplifts might create favorable conditions for instability growth and ESF development.

6.4 Future work

Our work has led us to identify that it would be important to better understand to what degree the day-to-day variability of quiet-time vertical drifts would affect the GRT instability. Focus is to be given to scenarios that could lead to postmidnight ESF during June solstice and low solar flux conditions. Since routine measurements of vertical drifts during the period of interest are not available and the relationship between observed drifts and geomagnetic activity is complex, we suggest a numerical modeling approach. We would use a state-of-the-art numerical model of the atmosphere and ionosphere (WACCM-X) to derive short-term (day-to-day), physics-based variabilities of the vertical drifts. Aided by climatological models of the drifts, we would then create synthetic drift curves that could emulate the day-to-day variabilities of the drifts for the Peruvian sector. These synthetic curves could then be used to drive the SAMI2 model whose outputs will be used to evaluate the stability of the nighttime equatorial F-region. Salient day-to-day variabilities in the ionosphere are believed to be caused by geomagnetic forcing, lower atmospheric forcing and solar radiation changes (*H.-L. Liu et al.*, 2018). The proposed numerical approach would allow us to isolate the effects of the lower atmospheric forcing by fixing the geomagnetic (high latitude) activity and solar radiation. Initial results related to the study described above are provided in Appendix A.

APPENDIX

ON THE QUIET-TIME DAY-TO-DAY VARIABILITY OF VERTICAL DRIFTS AND POSTMIDNIGHT ESF

A.1 Introduction

As examined in this dissertation, recent reports indicate that ESF is observed with high occurrence rates during late night, post-midnight hours under June solstice and low solar flux conditions (*Patra et al.*, 2009; *Yokoyama et al.*, 2011; *Yizengaw et al.*, 2013). The generation of postmidnight ESF under disturbed geomagnetic conditions has been associated with disturbance dynamo electric fields and prompt-penetration electric fields (*Fejer et al.*, 1999; *Martinis et al.*, 2005; *Abdu* , 2012). However, it has been hypothesized that post-midnight ESF events could also be associated with quiet-time electric fields (*Yizengaw et al.*, 2013; *Zhan and Rodrigues*, 2018). Isolating geomagnetic effects, however, can be less than straightforward.

Nevertheless, the hypothesis around the effects of quiet-time drifts is motivated by observations of equatorial vertical drifts such as those shown in Figure A.1 for the Jicamarca Radio Observatory (JRO) in the Peruvian sector. Figure A.1 shows the average of the Jicamarca incoherent radar measurements (markers) with error bars indicating the variability of the drift values used in the averages. It also shows the predictions of the *Scherliess and Fejer* (1999) model for the same sector (solid thin curves). The curves are for different seasons and solar flux conditions and contain a wealth of information. Here we point out that the drifts after sunset reversal are much weaker during low solar flux conditions ($S_a = F_{10.7} =$ 80 SFU) than during periods of high solar activity ($S_a = 200$ SFU). This is, perhaps, more evident for June solstice conditions, a period when post-midnight ESF is reported to occur more frequently (*Patra et al.*, 2009; *Li et al.*, 2011). The variability for June solstice solstice is about 5-10 m/s, and suggests that cases of positive (upward) drifts might occur in the midnight-postmidnight sector.

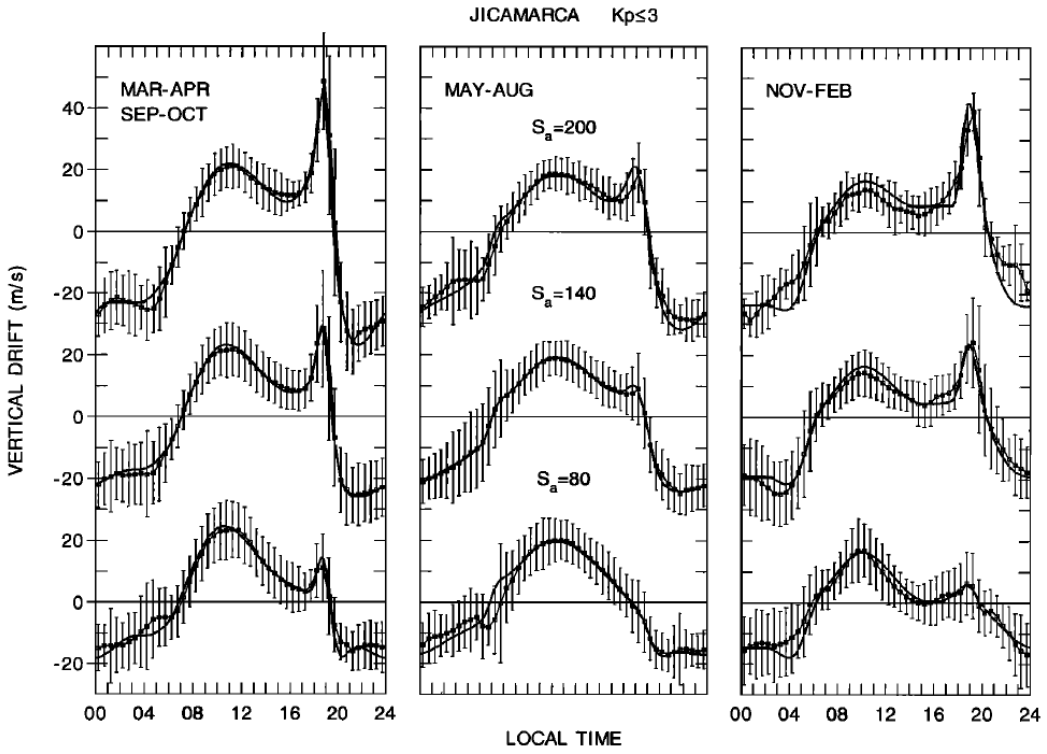

Figure A.1. Climatology of the equatorial vertical drifts estimated from the Jicamarca incoherent incoherent scatter radar measurements (thick line). The error bars represent the variability of the drifts used in the averages. Predictions of the *Scherliess and Fejer* (1999) model (think solid line) are also shown for each season and solar flux condition.

The occurrence of upward drifts near midnight or in the post-midnight sector has been reported to be associated with the observations of post-midnight ESF (*Yizengaw et al.*, 2013). As seen in this dissertation, weakening drifts, that is, drifts that are negative but weaken with time have also been suggested to be related to the occurrence of post-midnight ESF events (*Nicolls et al.*, 2006; *Ajith et al.*, 2016; *Zhan and Rodrigues*, 2018).

In this analysis, we take a numerical experiment approach to evaluate the potential of quiet-time vertical drifts alone on producing conditions that could lead to ESF development. The approach consists of generating vertical drift that resemble experimental curves to represent the day-to-day variability of the equatorial drifts for the Jicamarca longitude sector

and estimating the linear growth rates of GRT instability from the outputs of SAMI2 driven by the the synthetic vertical drift curves.

The numerical approach is motivated by the lack of adequate measurements of nighttime drifts, particularly during June solstice. The physics-based day-to-day variability of the drifts is estimated by the Whole Atmosphere Community Climate Model with Thermosphere and Ionosphere Extension (WACCM-X) with guidance from the *Scherliess and Fejer* (1999) model. The stability of the equatorial ionosphere is estimated following the approach of *Ajith et al.* (2016) and *Zhan and Rodrigues* (2018). That is, the drifts are used to drive SAMI2 whose outputs are used to compute the linear growth rate of the Generalized Rayleigh-Taylor (GRT) instability.

A.2 Methodology

In order to better understand and quantify the effects of realistic, quiet-time vertical drifts and their variability in the stability of the low-latitude ionosphere, we followed the data-driven procedure described by *Ajith et al.* (2016) and *Zhan and Rodrigues* (2018). We used time-dependent curves of the equatorial vertical drifts as inputs to the SAMI2 model of the low and mid-latitude ionosphere.

A.2.1 SAMI2

SAMI2 is Another Model of the Ionosphere is a physics-based numerical model of the low- and mid-latitude ionosphere (*Huba et al.*, 2000). It describes the dynamics and chemical evolution of seven ion species (H^+, He^+, N^+, O^+, N_2^+, NO^+ and O_2^+) in the altitude range between about $\sim$100 km to several thousand kilometers. It models the plasma along the geomagnetic field lines from hemisphere to hemisphere including ion inertia in the ion momentum equation for motion along the dipole field line. The neutral species are specified by the NRLMSISE00

model (*Hedin*, 1996). Thermospheric winds are specified by HWM93 model (*Picone et al.*, 2002).

In the present study, we target evaluating the effects of the quiet-time day-to-day variability of the drifts and their ability to create conditions favorable to the development of GRT irregularities in the post-midnight sector. While Jicamarca ISR can produce accurate measurements of vertical drifts as a function of local time, the observations are extremely limited, and do not allow a proper evaluation of its day-to-day variability. Only a few days (20-40) of observations are available per year and measurements during the period of highest interest (June solstice, low solar flux) are only a few.

In order to obtain realistic, physics-based estimates of the drift curves and their short-term (day-to-day) variability, we used simulation outputs of the WACCM-X, an state-of-the-art model of the Earth's atmosphere and ionosphere.

A.2.2 WACCM-X

The Whole Atmosphere Community Climate Model with Thermosphere and Ionosphere Extension (WACCM-X) is a comprehensive numerical model, spanning the range of altitude from the Earths surface to the upper thermosphere. It resolves the dynamical, physical and photochemical processes in the whole atmosphere domain. The top boundary of the model is located between ∼500 and ∼700 km, depending on the solar and geomagnetic activity. WACCM-X 2.0 is an updated version of WACCM-X in which several new features have been included since its first release. The new features include a self-consistent electrodynamics module that solves the ionospheric electric potential driven by the neutral wind dynamo. More details of the model can be found in *H.-L. Liu et al.* (2018).

It has already been shown that WACCM-X can produce realistic predictions of the behavior of equatorial vertical plasma drifts (*H.-L. Liu et al.*, 2018; *J. Liu et al.*, 2018). The initial results indicated that WACCM-X can produce most of the features in the equatorial drifts including the PRE. *H.-L. Liu et al.* (2018), however, already pointed that the

climatology (average behavior) of the drifts produced by WACCM-X do not exactly match the climatology of drifts derived from Jicamarca measurements. Of particular importance for this study is that the model produces results that resemble the quiet-time day-to-day variability of drifts.

While ionospheric variability can also be caused by geomagnetic and solar forcing, we used the WACCM-X to derive physics-based, curves of the equatorial vertical drifts that contained variability due to lower atmospheric forcing alone. A total of 120 days of WACCM-X simulations were analyzed in this study. These simulations were composed of 4 subsets of 30 simulation days for each season (June Solstice, December Solstice, March Equinox and September Equinox). The simulations were performed for low solar flux conditions (F10.7 = 70 solar flux units) and under quiet geomagnetic conditions (Kp = 1.0) to avoid effects of high-latitude electric fields and capture the quiet-time day-to-day variability only. The initial simulations have a temporal resolution of 1 hour. A linear interpolation is carried out to derive drift curves with points spaced by 15 minutes and to match the *Scherliess and Fejer* (1999) (SF99) model outputs used in SAMI2.

A.2.3 Climatological Drift Model (SF99)

Since *H.-L. Liu et al.* (2018) already indicated discrepancies between mean WACCM-X drifts and measurement-based climatological model predictions, we also used the SF99 climatological model of the vertical drifts to evaluate the WACCM-X outputs as well as to guide our SAMI2 simulations. The SF99 model was based on 502 days of ISR measurements made from 1968 to 1992 at Jicamarca. Furthermore, the model used in-situ satellite measurements from the Atmospheric Explorer-E (AE-E) satellite to expand the model to longitudes outside the Peruvian sector. The SF99 has been extensively tested and represents well the conditions observed over Jicamarca outside the 1968-1992 period. For instance, an excellent agreement was recently found between SF99 predictions and new observations made between 1986 and 2017 (*Shidler et al.*, 2019).

A.2.4 GRT Linear Growth Rate

To estimate the impact of the vertical drifts on the stability of the nighttime equatorial ionosphere, we used the outputs of the SAMI2 model and the flux-tube integrated formulation of the linear growth rate described by *Sultan* (1996):

$$\gamma_{RT} = \frac{\Sigma_P^F}{\Sigma_P^E + \Sigma_P^F}(V_p - U_L^P + \frac{g_e}{\nu_{eff}})K^F \tag{A.1}$$

where Σ_P^E and Σ_P^F are flux-tube integrated E- and F-region Pedersen conductivities, respectively. V_p is the equatorial vertical drift velocity. U_L^P is the Pedersen conductivity weighted, flux-tube integrated thermospheric meridional winds perpendicular to field line. g_e is the local gravitational acceleration defined as $\frac{g_0}{L^2}$ (where g_0 is the gravitational acceleration on the equatorial surface of earth, and L is the distance from the center of the Earth in Earth radii). ν_{eff} is the flux-tube integrated effective F-region ion-neutral collision frequency. K^F is defined by $\frac{1}{N_e}\frac{\partial N_e}{\partial h}$ (where N_e is the flux-tube integrated electron density, and h is the height in the equatorial plane).

A.3 Results and Discussion

A.3.1 On WACCM-X drifts

Figure A.2 shows a summary of the vertical drifts simulated by WACCM-X for the coordinates of the Jicamarca Radio Observatory during quiet, low solar flux conditions. It shows the 30 daily curves (gray solid lines) of the vertical drifts predicted by WACCM-X for each season (around Mar. 21, Jun. 21, Sep. 21, and Dec. 21) as well as the mean variation of the curves (red solid lines). The drifts are for an altitude of 250 km. It also shows the SF99 model predictions of the drifts for each season (blue solid lines).

The WACCM-X curves show significant day-to-day variability. Considering a specific local time, drifts from different days can differ by over 10 m/s. The average variation

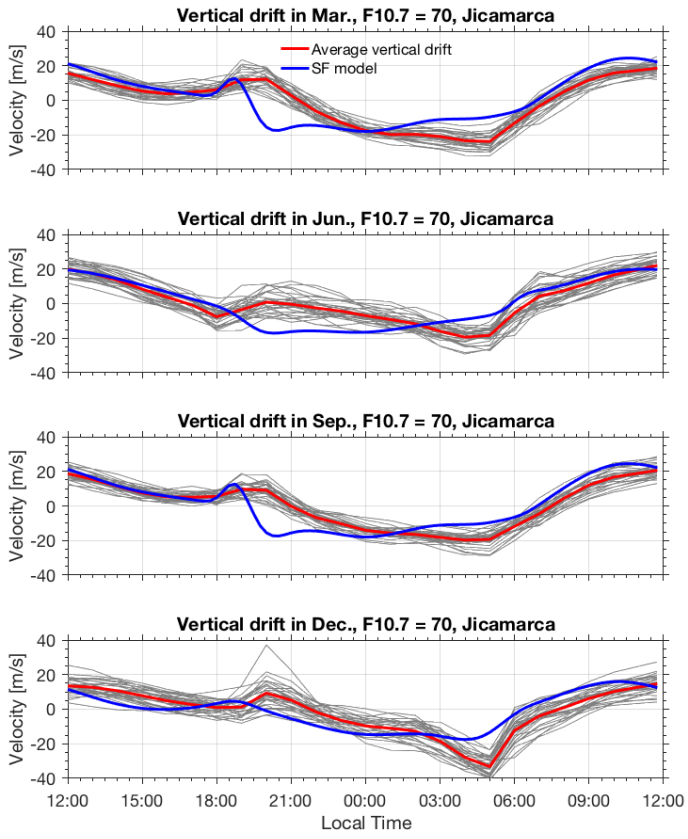

Figure A.2. Equatorial vertical plasma drifts simulated by the WACCM-X model for 30 days (gray line curves) around each season (Mar. 21, Jun. 21, Sep. 21, and Dec. 21) and their average (red curves). The curve is the SF99 model prediction for each season.

(standard deviation) of the drifts is 3.3 m/s for March Equinox, 4.6 m/s for June Solstice, 3.2 m/s for September Equinox and 4.9 m/s for December Solstice. The magnitude of the WACCM-X drift variabilities are smaller than those seen in Figure A.1. This is, at least in part, because the drifts in Figure A.1 have contributions from solar forcing, geomagnetic activity and measurement errors. The observations in Figure A.1 come from a range of solar flux conditions. Additionally, the Jicamarca measurements were made over a small range of geomagnetic conditions (Kp $\leq$ 3).

WACCM-X produces curves with the overall features expected for the equatorial plasma drifts. The drifts are predominately upward during the day, and downward at night. WACCM-X is also able to produce the peaks in the upward drifts associated with the PRE. There are, however, significant differences between the drifts produced by WACCM-X and climatological values. Some of them were already pointed out by *H.-L. Liu et al.* (2018) and include differences in the timing of the PRE.

Of particular importance here are the nighttime drifts during June solstice. During that period, there seems to be a large discrepancy between SF99 predictions and WACCM-X outputs. WACCM-X overestimates the drifts around the terminator sectors. It shows weakening of the drifts starting at around 18:00 LT and cases of weak or upward drifts near midnight. Additionally, WACCM-X shows large downward drifts near dawn.

Here, we must point out that while June solstice drifts depart from SF99 predictions, they resemble observations made by C/NOFS during the 2008/2009 solar minimum. During that period C/NOFS observed upward drifts near midnight (*Stoneback et al.*, 2011). In fact, *Stoneback et al.* (2011) suggested that these abnormal upward drifts near midnight could be responsible for the high occurrence rate of midnight/post-midnight ionospheric irregularities observed by C/NOFS during 2008/2009.

A.3.2 On SF99 Drifts with WACCM-X Variabilities

As mentioned earlier, our objective is to evaluate day-to-day variabilities in the stability of the equatorial F-region that result directly from quiet-time, day-to-day variability in the drifts. The mean variation of the WACCM-X drifts, however, depart from our expectation for the drifts based on well-tested climatological model predictions. The results in Figure A.2 suggest, nevertheless, that WACCM-X is capable of producing realistic variations of the drifts. Additional comparisons, nevertheless, can be done with daily daytime measurements of 150-km echoes drifts made by the JULIA system at Jicamarca.

For our numerical experiments, we chose to use the WACCM-X day-to-day variabilities, that is, departures of daily drift curves from the mean value to create synthetic curves of the drifts for Jicamarca sector. Then, we added the WACCM-X daily variabilities to the SF99 model predictions of the drifts. The resulting synthetic curves of the drifts are shown in Figure A.3. Similar to Figure A.2, 30 daily curves are shown for each season (solid gray lines). We also show the SF99 climatological predictions for each season. The most striking feature in Figure A.3 is that the new curves, now, reverse from upward to downward much earlier and much more quickly than the curves predicted by WACCM-X. As expected, the curves also better resemble Jicamarca measurements such as those shown in Figure A.3.

A.3.3 Linear Growth Rate Results

Now that we have created synthetic daily curves of realistic drifts for the Jicamarca sector, we can evaluate the effects of those drifts in the stability of the midnight and postmidnight equatorial F-region. As described in section A.2, the curves were used to drive SAMI2 simulations, and SAMI2 outputs were used to evaluate the linear growth rate of the GRT instability. The results for March equinox, June solstice, September equinox and December solstice are shown in Figures A.4 - A.7, respectively.

With respect to results for Equinox and December solstice, we only mention that, as expected, growth rates with positive magnitudes around 2-3 e-folds/hour are commonly observed. These values are consistent with estimates obtained in previous studies (*Zhan et al.*, 2018). There is some significant variability in the growth rate maximum values more clearly seen, perhaps, during December solstice. Growth rate values in December solstice seem to be relatively smaller than those observed during Equinox but continue over a longer period of time. This is consistent with longer-lasting occurrence rates of ESF observed in our previous studies (*Zhan et al.*, 2018), and it is related to time history of the drifts. Drifts in December take longer to reverse than drifts during equinox (*Fejer et al.*, 1999).

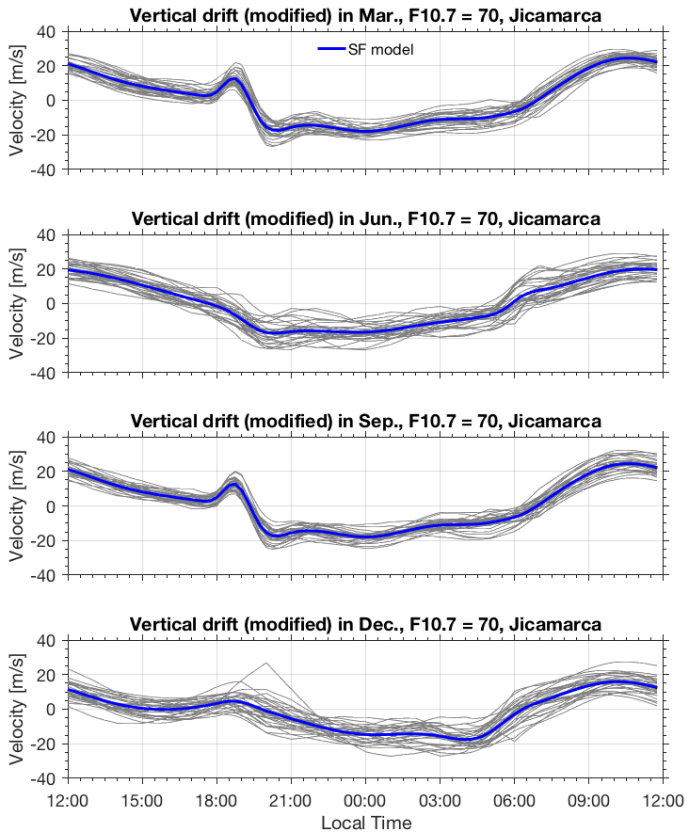

Figure A.3. Synthetic vertical plasma drifts created using SF99 climatological predictions (blue curves) and WACCM-X drift variabilities for 30 days (gray line curves) around each season (Mar. 21, Jun. 21, Sep. 21, and Dec. 21).

Of particular importance here are the results for June solstice when post-midnight ESF are reported to occur during low solar flux conditions. The results (Figure A.5) do not show any significant growth rate values, even during the evening. Based on the drifts, this is not surprising. There is no significant PRE or noticeable increases in upward drifts in the midnight/post- midnight sector. The results suggest that quiet-time drifts alone do not destabilize F-region enough to explain the observed occurrence rates of post-midnight ESF. Additional factors, such as disturbance electric fields of magnetospheric origin (*Fejer et al.*, 1999) or converging neutral winds (*Yokoyama et al.*, 2011; *Huba et al.*, 2013; *Zhan*

et al., 2018) would be needed to create destabilizing conditions that could produce ESF irregularities.

For completeness, we also computed the growth rates for SAMI2 simulations driven by WACCM-X drifts (Figure A.2). The results for March Equinox, June Solstice, September Equinox, and December Solstice are shown in Figures A.8 - A.11, respectively.

Again growth rates with peak values of about 2-3 e-folds/hour are commonly seen in the evening sector. The morphology of the linear growth rate as a function of local time and height, however, is different from what was obtained with the synthetic drift curves. For Equinox and December solstice, in general, the growth rates start to increase around sunset and continue with significant values for several hours.

Again, of particular interest to this study are the results for June solstice. The results show a large day-to-day variability. More importantly, it shows several cases when large ($\sim$ 2 e-folds/hour) growth rates are produced with peak values near midnight. This large positive growth rates indicate a destabilized ionosphere which could provide favorable enough conditions to generate strong ESF events near midnight. It remains, however, to be seen if curves such as those produced by WACCM-X could indeed be observed.

A.4 Concluding Remarks

We provided preliminary results related to a study of the effects of the quiet-time day-to-day variability of vertical drifts on postmidnight ESF during solar minimum using numerical simulation analyses. With the help of WACCM-X and the SF99 climatological model, we produced realistic curves of the equatorial vertical drifts with quiet-time, day-to-day variabilities for each season during solar minimum. Then, using the outputs of SAMI2 driven by modified climatological drift curves and WACCM-X drift curves in each season, respectively, we estimated the day-to-day variability of the linear growth rates for the GRT instability. The modified climatological drift curves did not produce any significant growth rate values

in the midnight-postmidnight sector. Therefore, the results indicate that lower atmospheric forcing alone cannot explain the observed occurrence of postmidnight ESF during June solstice in the American sector. The results also reinforce the importance of additional factors such as geomagnetic activity and converging winds for postmidnight ESF generation. Interestingly, however, WACCM-X drifts produce weak and upward drifts near midnight and significant ($\sim$ 2 e-folds/hour) growth rate values at times. Efforts to better characterize the nighttime drifts (including its short-term variability) in the American sector during June solstice should be attempted to support the numerical findings.

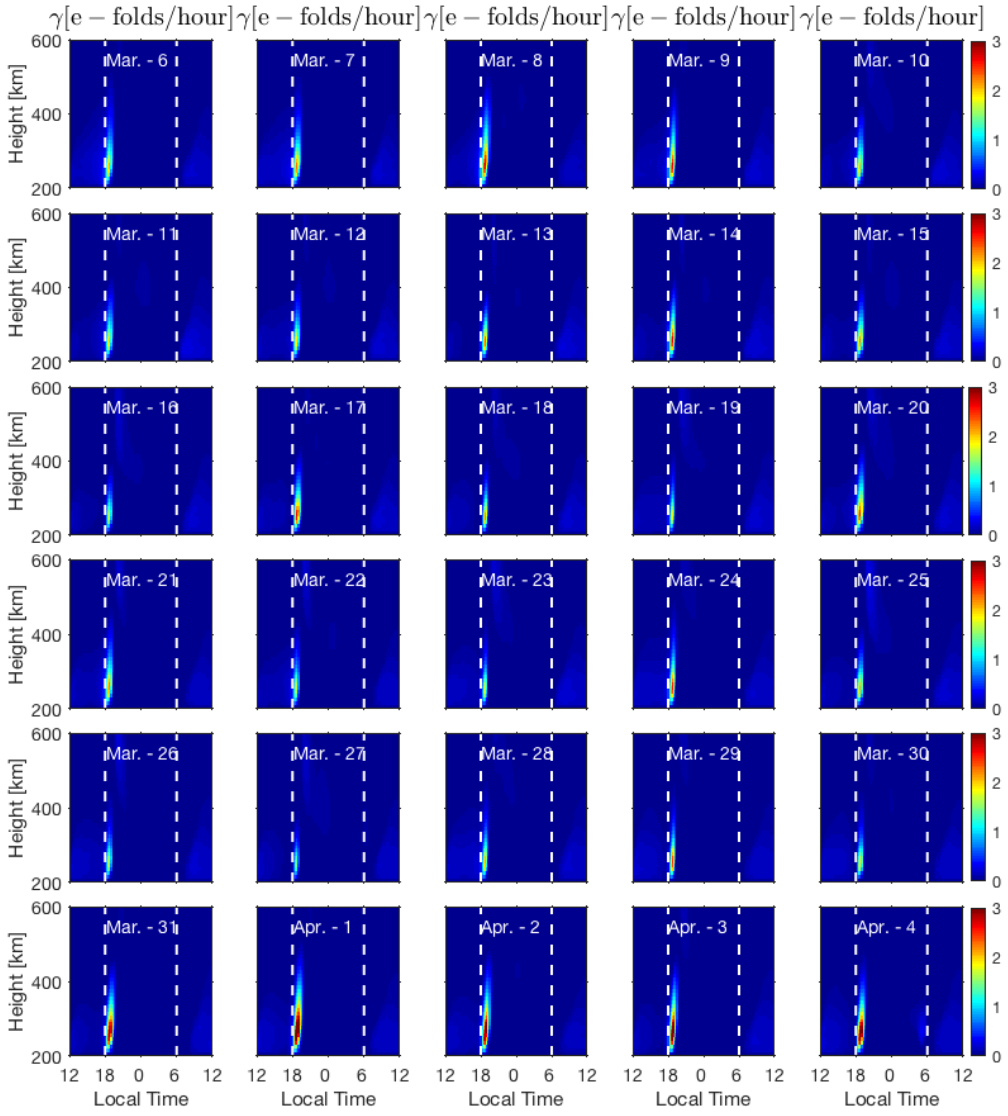

Figure A.4. Results of the linear growth rate estimates for March Equinox. The growth rates were estimated from SAMI2 outputs driven by the synthetic drift curves (Figure A.3).

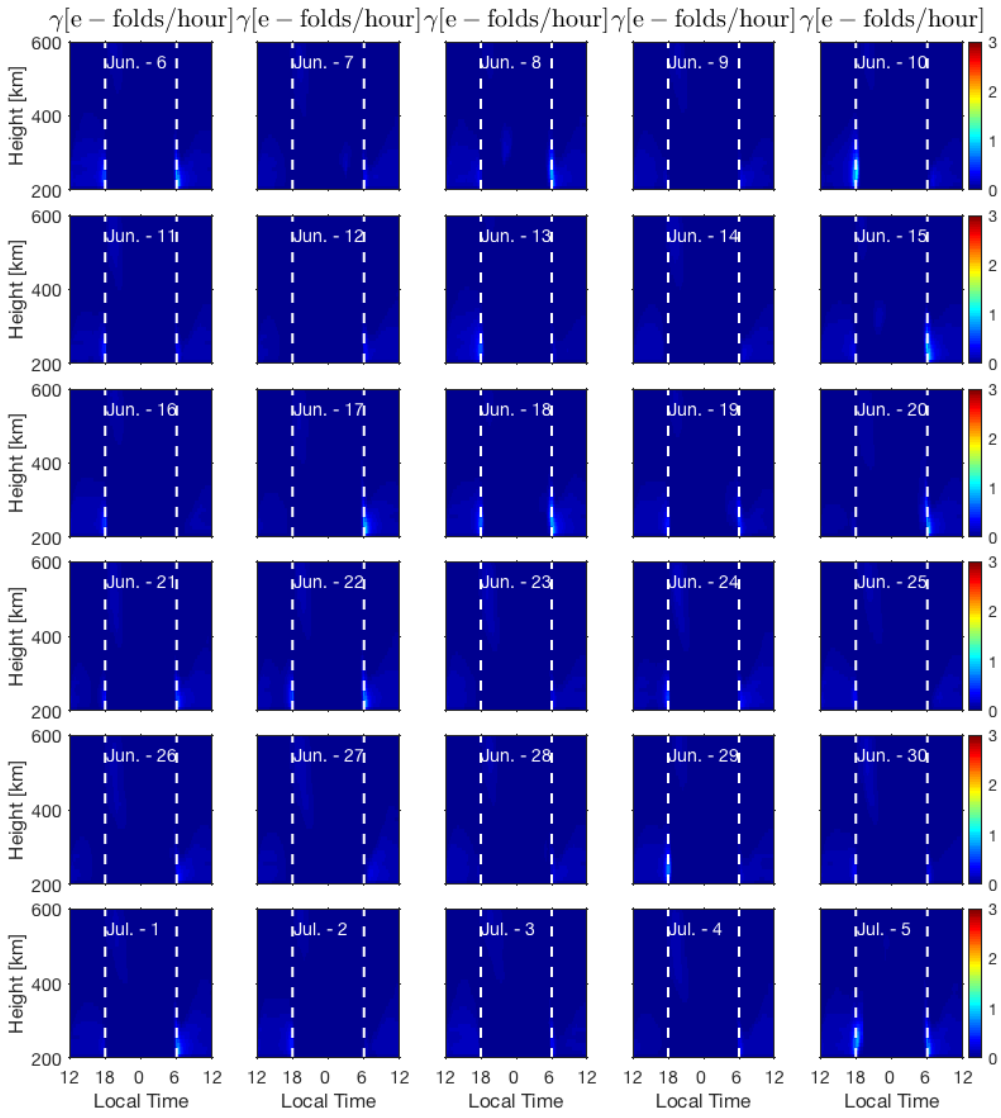

Figure A.5. Results of the linear growth rate estimates for June Solstice. The growth rates were estimated from SAMI2 outputs driven by the synthetic drift curves (Figure A.3).

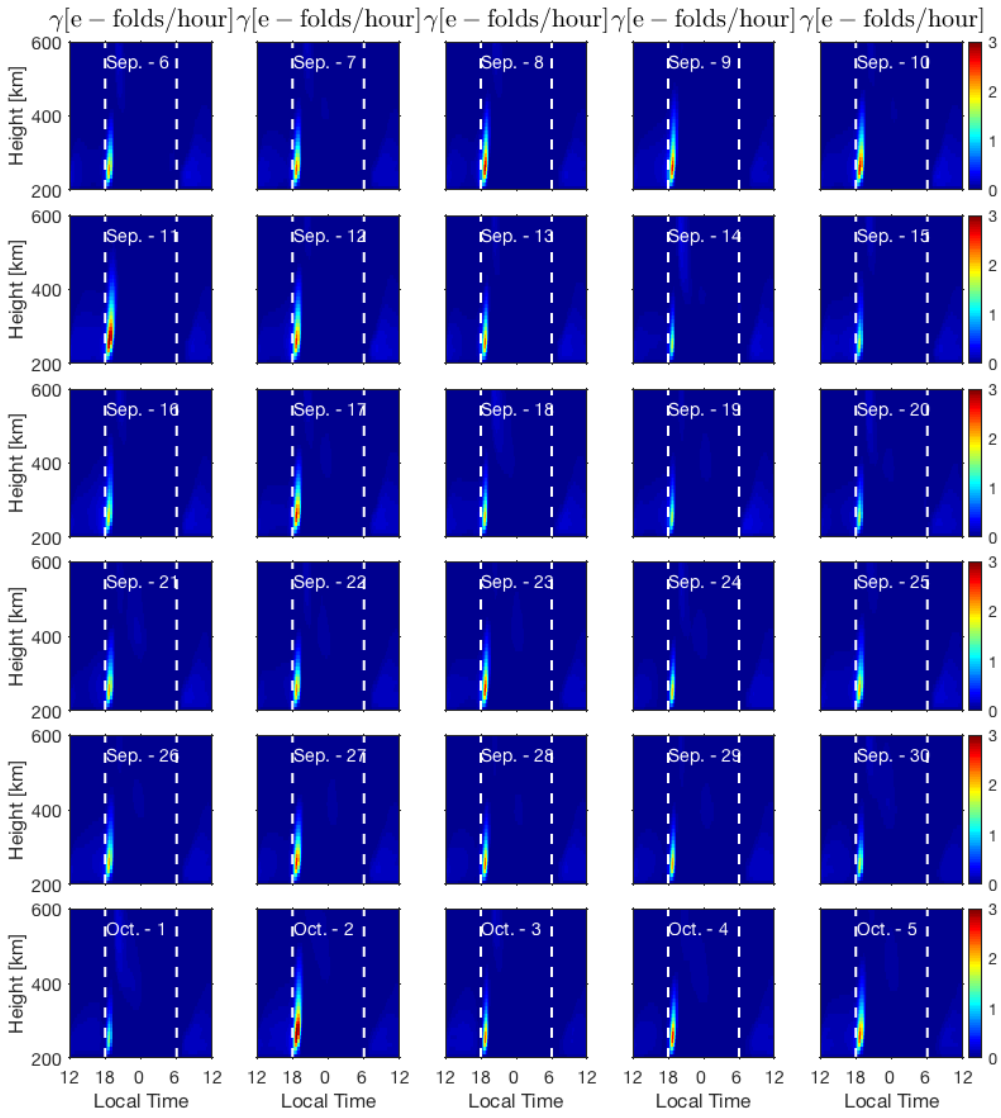

Figure A.6. Results of the linear growth rate estimates for September Equinox. The growth rates were estimated from SAMI2 outputs driven by the synthetic drift curves (Figure A.3).

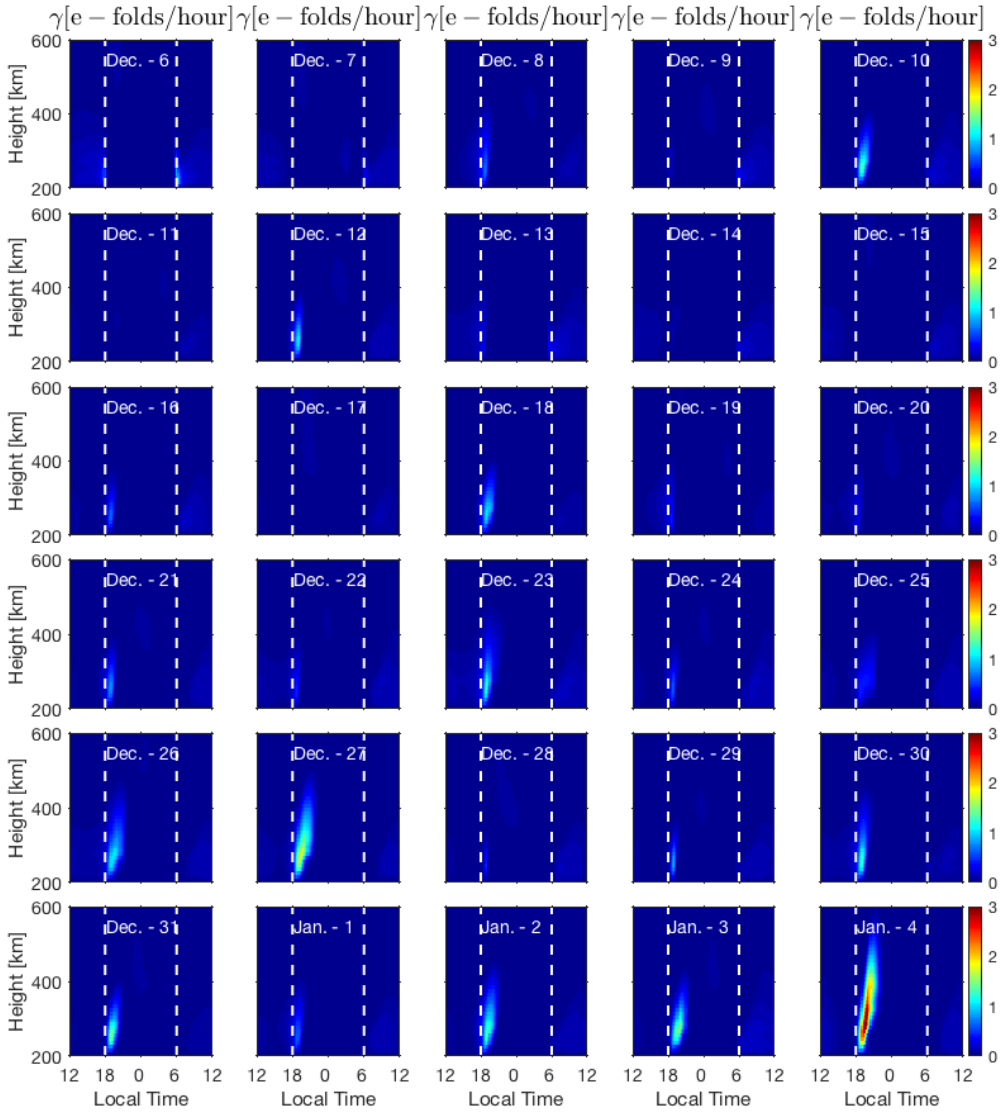

Figure A.7. Results of the linear growth rate estimates for December Solstice. The growth rates were estimated from SAMI2 outputs driven by the synthetic drift curves (Figure A.3).

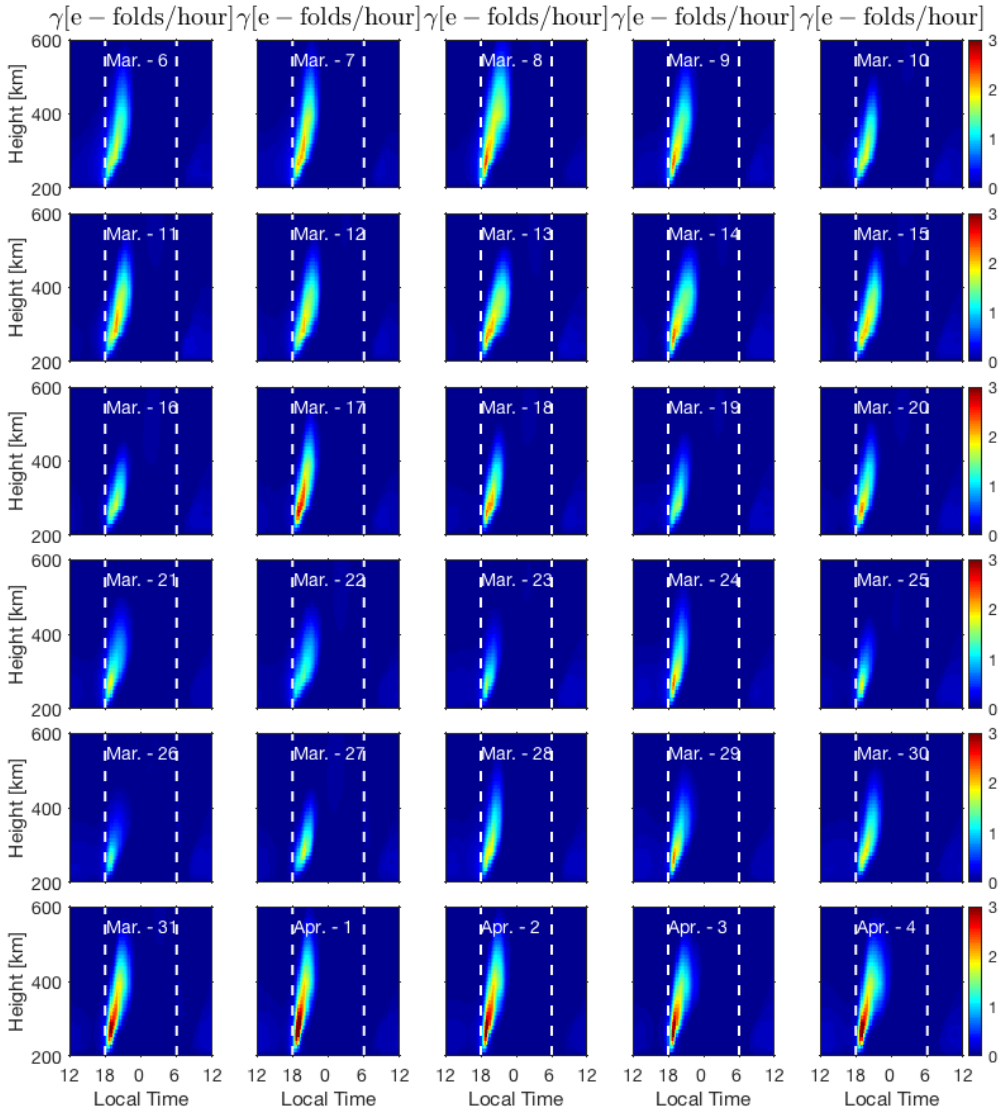

Figure A.8. Results of the linear growth rate estimates for March Equinox. The growth rates were estimated from SAMI2 outputs driven by WACCM-X drift curves (Figure A.2).

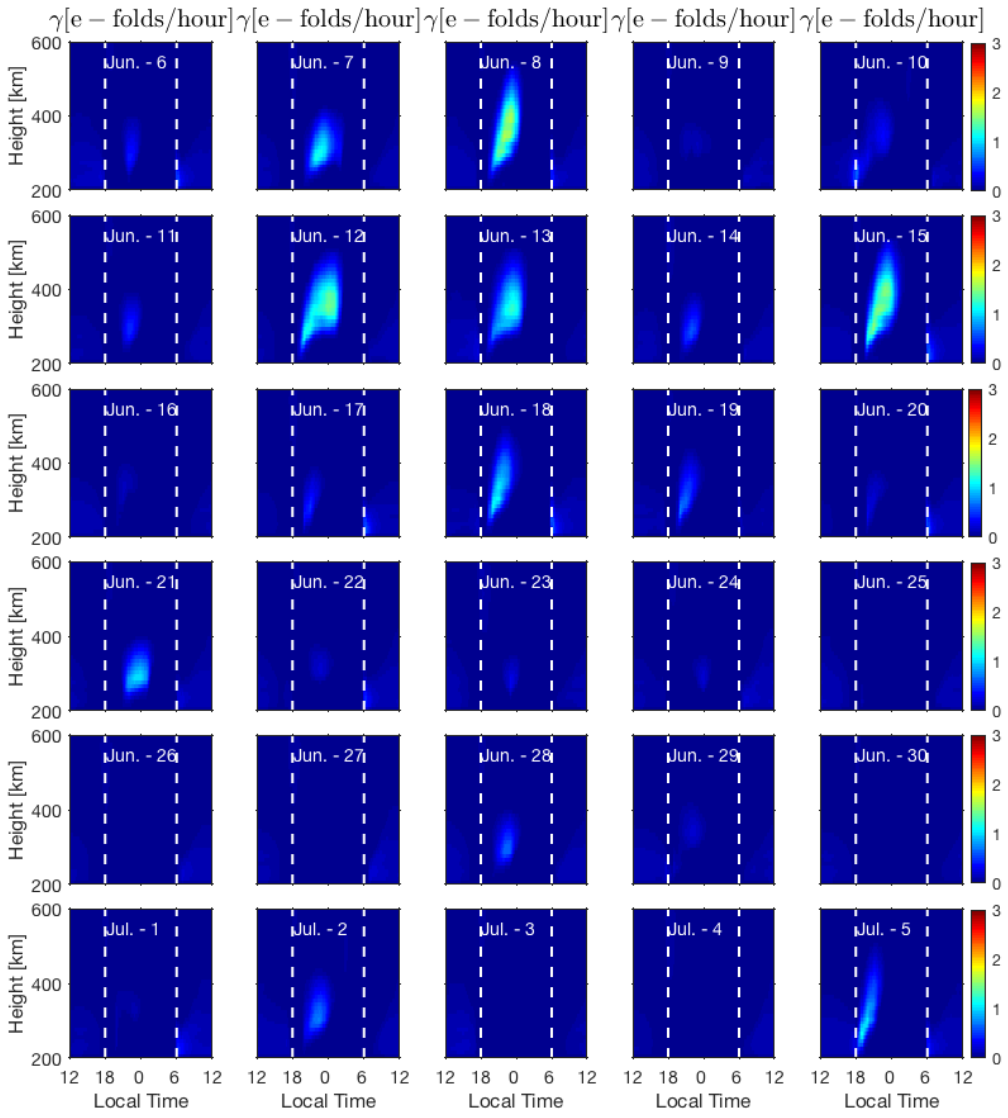

Figure A.9. Results of the linear growth rate estimates for June Solstice. The growth rates were estimated from SAMI2 outputs driven by WACCM-X drift curves (Figure A.2).

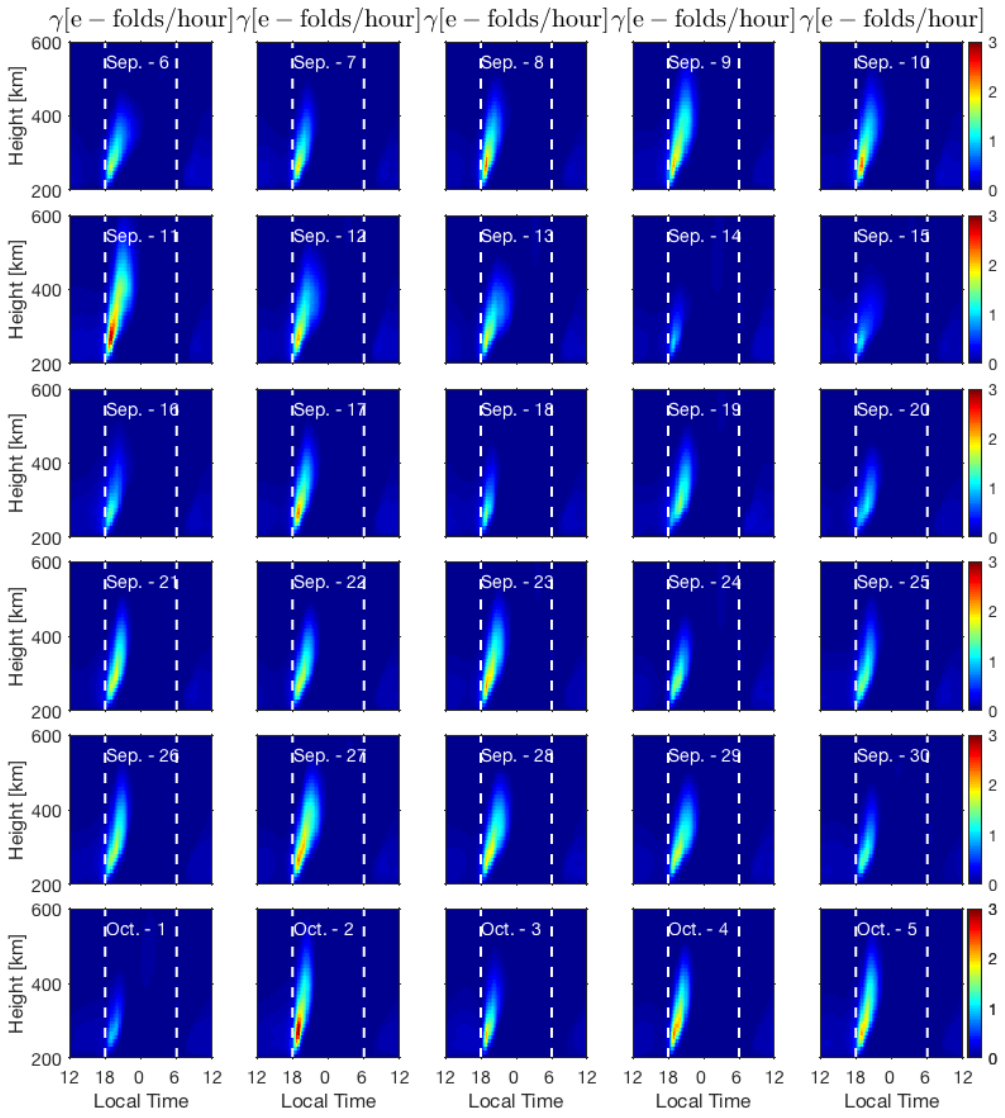

Figure A.10. Results of the linear growth rate estimates for September Equinox. The growth rates were estimated from SAMI2 outputs driven by WACCM-X drift curves (Figure A.2).

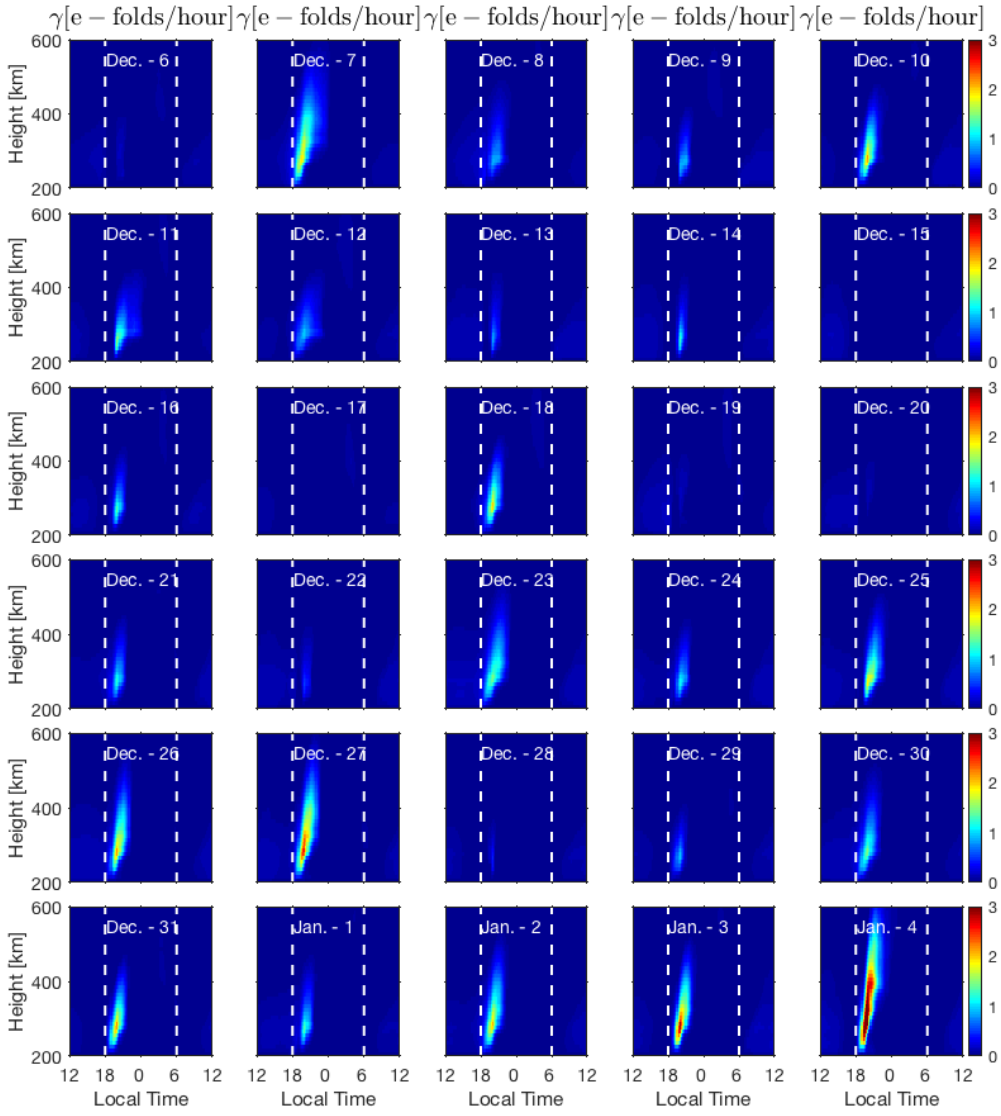

Figure A.11. Results of the linear growth rate estimates for December Solstice. The growth rates were estimated from SAMI2 outputs driven by WACCM-X drift curves (Figure A.2).

REFERENCES

Abdu, M. A. (2012). Equatorial spread F/plasma bubble irregularities under storm time disturbance electric fields. Journal of Atmospheric and Solar-Terrestrial Physics, 7576, 4456. https://doi.org/10.1016/j.jastp.2011.04.024

Abdu, M. A., J. A. Bittencourt, and I. S. Batista (1981), Magnetic declination control of the equatorial F region dynamo electric field development and spread F, J. Geophys. Res., 86(A13), 11443 - 11446, doi:10.1029/JA086iA13p11443.

Abdu, M. A., C.M. Denardini, J.H.A. Sobral, I.S. Batista, P. Muralikrishna, E.R. de Paula (2002), Equatorial electrojet irregularities investigations using a 50MHz back-scatter radar and a digisonde at Sao Luis: some initial results, Journal of Atmospheric and Solar-Terrestrial Physics, Volume 64, Issues 1214, 2002,1425-1434, ISSN 1364-6826, https://doi.org/10.1016/S1364-6826(02)00106-2.

Abdu, M. A. (2016) Electrodynamics of ionospheric weather over low latitudes, Geosci. Lett. 3:11 DOI 10.1186/s40562-016-0043-6.

Abdu, M. A. (2019). Day-to-day and short-term variabilities in the equatorial plasma bubble/spread F irregularity seeding and development, Progress in Earth and Planetary Science, 6, 1, 2019.

Ajith, K. K., S. T. Ram, M. Yamamoto, T. Yokoyama, V. S. Gowtam, Y. Otsuka, T. Tsugawa, and K. Niranjan (2015), Explicit characteristics of evolutionary-type plasma bubbles observed from Equatorial Atmosphere Radar during the low to moderate solar activity years 2010-2012, J. Geophys. Res. Sp. Phys., 120(2), 1371-1382, doi:10.1002/2014JA020878.

Ajith, K. K., S. Tulasi Ram, M. Yamamoto, Y. Otsuka, and K. Niranjan (2016), On the fresh development of equatorial plasma bubbles around the midnight hours of June solstice, J. Geophys. Res. A Sp. Phys., 121(9), 9051-9062, doi:10.1002/2016JA023024.

Alam Kherani, E., Abdu, M. A., de Paula, E. R., Fritts, D. C., Sobral, J. H. A., and de Meneses Jr., F. C. (2012) The impact of gravity waves rising from convection in the lower atmosphere on the generation and nonlinear evolution of equatorial bubble, Ann. Geophys., 27, 1657-1668, https://doi.org/10.5194/angeo-27-1657-2009, 2009.

Aveiro, H. C., and D. L. Hysell (2010), Threedimensional numerical simulation of equatorial F region plasma irregularities with bottomside shear flow, J. Geophys. Res., 115, A11321, doi:10.1029/2010JA015602.

Aveiro,H.C., D. L. Hysell, J.Park, andH.Lhr (2011), Equatorial spread Frelated currents: Threedimensional simulations and observations, Geophys. Res. Lett., 38, L21103, doi:10.1029/2011GL049586.

Aveiro, H. C., D. L. Hysell, R. G. Caton, K. M. Groves, J. Klenzing, R. F. Pfaff, R. Stoneback, and R. A. Heelis (2012), Three-dimensional numerical simulations of equatorial spread F: Results and observations in the Pacific sector, J. Geophys. Res., 117, A03325, doi:10.1029/2011JA017077.

Basu, S., E. MacKenzie, and S. Basu (1988), Ionospheric constraints on VHF/UHF communications links during solar maximum and minimum periods, Radio Sci., 23(3), 363378, doi:10.1029/RS023i003p00363.

Basu, B., On the linear theory of equatorial plasma instability: Comparison of different descriptions, J. Geophys. Res., 107(A8), doi:10.1029/2001JA000317, 2002.

Booker, H. G., and H. W. Wells (1938), Scattering of radio waves by the F-region of the ionosphere, Terr. Magn. Atmos. Electr., 43(3), 249-256, doi:10.1029/TE043i003p00249.

Burke, W. J., O. de La Beaujardire, L. C. Gentile, D. E. Hunton, R. F. Pfaff, P. A. Roddy, Y.-J. Su, and G. R. Wilson (2009), C/NOFS observations of plasma density and electric field irregularities at post-midnight local times, Geophys. Res. Lett., 36(18), L00C09, doi:10.1029/2009GL038879.

Burns, C. J., and J. K. Hargreaves (1996), The occurrence and properties of large-scale electron-density structures in the auroral F region, J. Atmos. Terr. Phys., 58(1-4), 217-232, doi:10.1016/0021-9169(95)00031-3.

Candido, C. M. N., Batista, I. S., BeckerGuedes, F., Abdu, M. A., Sobral, J. H. A., and Takahashi, H. (2011), Spread F occurrence over a southern anomaly crest location in Brazil during June solstice of solar minimum activity, J. Geophys. Res., 116, A06316, doi:10.1029/2010JA016374.

Carrano, C. S., K. M. Groves, and R. G. Caton (2012), Simulating the impacts of ionospheric scintillation on L band SAR image formation, Radio Sci., 47, RS0L20, doi: 10.1029/2011RS004956.

Chapagain, N. P., B. G. Fejer, and J. L. Chau (2009), Climatology of postsunset equatorial spread F over Jicamarca, J. Geophys. Res., 114, A07307, doi:10.1029/2008JA013911.

Chau, J. L., Woodman, R. F., and Flores, L. A (2002).: Statistical characteristics of low-latitude ionospheric field-aligned irregularities obtained with the Piura VHF radar, Ann. Geophys., 20, 1203-1212, https://doi.org/10.5194/angeo-20-1203-2002.

Cueva, R. Y. C., E. R. de Paula, and A. E. Kherani (2003), Statistical analysis of radar observed F region irregularities from three longitudinal sectors, Ann. Geophys., 31, 2137-2146, https://doi.org/10.5194/angeo-31-2137-2013.

Cohen, R., and K. L. Bowles (1961), On the nature of equatorial spread F, J. Geophys. Res., 66(4), 1081-1106, doi:10.1029/JZ066i004p01081.

Dao, T., Y. Otsuka, K. Shiokawa, M. Nishioka, M. Yamamoto, S. M. Buhari, M. Abdullah, and A. Husin (2017), Coordinated observations of postmidnight irregularities and thermospheric neutral winds and temperatures at low latitudes, J. Geophys. Res. Sp. Phys., 122(7), 7504-7518, doi:10.1002/2017JA024048.

Dao, E., M. C. Kelley, P. Roddy, J. Retterer, J. O. Ballenthin, O. de La Beaujardiere, and Y.-J. Su (2011), Longitudinal and seasonal dependence of nighttime equa- torial plasma density irregularities during solar minimum detected on the C/NOFS satellite, Geophys. Res. Lett., 38, L10104, doi:10.1029/2011GL047046.

Das, T., K. S. Paul, and A. Paul (2014), Observation of ionospheric irregularities around midnight and post-midnight near the northern crest of the Equatorial Ionization Anomaly in the Indian longitude sector: Case studies, J. Atmos. Solar-Terrestrial Phys., 121(PB), 188-195, doi:10.1016/j.jastp.2014.05.001.

de La Beaujardiere, O., et al. (2004), C/NOFS: A mission to forecast scintillations, J. Atmos. Sol. Terr. Phys., 66, 1573-1571, doi:10.1016/j.jastp.2004.07.030.

de La Beaujardire, O. et al. (2009), C/NOFS observations of deep plasma depletions at dawn, Geophys. Res. Lett., 36(18), L00C06, doi:10.1029/2009GL038884.

de Paula, E. R., and D. L. Hysell (2004), The São Luís 30 MHz coherent scatter ionospheric radar: System description and initial results, Radio Sci., 39, RS1014, doi:10.1029/2003RS002914.

de Paula, E. R., E. Alam Kherani, R. Y. C. Cueva, and L. A. P. Camargo (2011), Observations of pre-midnight 5-m irregularities in the equatorial F region over São Luís, Brazil: Solar-flux dependence and seasonal variations, J. Atmos. Solar-Terrestrial Phys., 73(1112), 15441554, doi:10.1016/j.jastp.2011.03.014.

Dungey, J. W. (1956), Convective diffusion in the equatorial F region, J. Atmos. Terr. Phys., 9(56), 304-310, doi:10.1016/0021-9169(56)90148-9.

Eccles, J. V., J. P. St. Maurice, and R. W. Schunk (2015), Mechanisms underlying the prereversal enhancement of the vertical plasma drift in the low-latitude ionosphere. J. Geophys. Res. Space Physics, 120, 4950-4970. doi: 10.1002/2014JA020664.

Fang, T.-W., R. A. Akmaev, R. A. Stoneback, T. Fuller-Rowell, H. Wang, and F. Wu (2016), Impact of midnight thermosphere dynamics on the equatorial ionospheric vertical drifts, J. Geophys. Res. Sp. Phys., 121(5), 4858-4868, doi:10.1002/2015JA022282.

Farley, D. T., B. B. Balsey, R. F. Woodman, and J. P. McClure (1970), Equatorial spread F : Implications of VHF radar observations, J. Geophys. Res., 75(34), 7199-7216, doi:10.1029/JA075i034p07199.

Farley, D. T., E. Bonelli, B. G. Fejer, and M. F. Larsen (1986), The prereversal enhancement of the zonal electric field in the equatorial ionosphere, J. Geophys. Res., 91(A12), 13723-13728, doi: 10.1029/JA091iA12p13723.

Fejer, B. G. (1981), The equatorial ionospheric electric fields: a review, J. Atmos-Terr. Phys., 43, 5/6, 377-386, doi:10.1016/0021-9169(81)90101-X.

Fejer, B. G. (1991), Low latitude electrodynamic plasma drifts: a review, J. Atmos-Terr. Phys., 53, 8, 677-693, doi:10.1016/0021-9169(91)90121-M.

Fejer, B. G., L. Scherliess, and E. R. de Paula (1999), Effects of the vertical plasma drift velocity on the generation and evolution of equatorial spread F, J. Geophys. Res. Sp. Phys., 104(A9), 19859-19869, doi:10.1029/1999JA900271.

Fukao, S., J.P. McClure, A. Ito, T. Sato, I. Kimura, T. Tsuda, and S. Kato (1988), First VHF radar observation of mid- latitude F-region field-aligned irregularities, Geophys. Res. Left., 15, 768-771, 1988.

Gentile, L. C., W. J. Burke, and F. J. Rich (2006), A global climatology for equatorial plasma bubbles in the topside ionosphere, Ann. Geophys., 24, 163-172.

Gentile, L. C., W. J. Burke, P. A. Roddy, J. M. Retterer, and R. T. Tsunoda (2011), Climatology of plasma density depletions observed by DMSP in the dawn sector, J. Geophys. Res. Sp. Phys., 116(3), 1-11, doi:10.1029/2010JA016176.

Harding, B. J., and Milla, M. (2013), Radar imaging with compressed sensing, Radio Sci., 48, 582 588, doi:10.1002/rds.20063.

Hargreaves, J. K. (1992), The Solar-Terrestrial Environment, Cambridge University Press, Cambridge.

Hedin, A. E., et al. (1996), Empirical wind model for the upper, middle and lower atmosphere, J. Atmos. Terr. Phys., 58(13), 14211447, doi:10.1016/0021-9169(95)00122-0.

Heelis, R. A. (2004), Electrodynamics in the low and middle latitude ionosphere: A tutorial, J. Atmos. Solar-Terrestrial Phys., 66(10), 825-838, doi:10.1016/j.jastp.2004.01.034.

Heelis, R. A., R. Stoneback, G. D. Earle, R. A. Haaser, and M. A. Abdu (2010), Mediumscale equatorial plasma irregularities observed by Coupled IonNeutral Dynamics Investigation sensors aboard the Communication Navigation Outage Forecast System in a prolonged solar minimum, J. Geophys. Res., 115, A10321, doi: 10.1029/2010JA015596.

Heelis, R. A., G. Crowley, F. Rodrigues, A. Reynolds, R. Wilder, I. Azeem, and A. Maute (2012), The role of zonal winds in the production of a pre-reversal enhancement in the vertical ion drift in the low latitude ionosphere, J. Geophys. Res. Sp. Phys., 117(8), 1-9, doi:10.1029/2012JA017547.

Hildebrand, P. H. and R. S. Sekhon (1974): Objective Determination of the Noise Level in Doppler Spectra. J. Appl. Meteor., 13, 808811, https://doi.org/10.1175/1520-0450(1974)013<0808:ODOTNL>2.0.CO;2

Huang, C. Y., W. J. Burke, J. S. Machuzak, L. C. Gentile, and P. J. Sultan, Equatorial plasma bubbles observed by DMSP satellites during a full solar cycle: Toward a global climatology, J. Geophys. Res., 107(A12), 1434, doi:10.1029/2002JA009452, 2002.

Huang, C. S., O. De La Beaujardiere, P. A. Roddy, D. E. Hunton, R. F. Pfaff, C. E. Valladares, and J. O. Ballenthin (2011), Evolution of equatorial ionospheric plasma bubbles and formation of broad plasma depletions measured by the C/NOFS satellite during deep solar minimum, J. Geophys. Res. Sp. Phys., 116(3), doi:10.1029/2010JA015982.

Huang, C.-S., O. de La Beaujardiere, P. A. Roddy, D. E. Hunton, J. Y. Liu, and S. P. Chen (2014), Occurrence probability and amplitude of equatorial ionospheric irregularities associated with plasma bubbles during low and moderate solar activities (2008-2012), J. Geophys. Res. Sp. Phys., 119(2), 1186-1199, doi:10.1002/2013JA019212.

Huang, C., and Hairston, M. R. (2015), The postsunset vertical plasma drift and its effects on the generation of equatorial plasma bubbles observed by the C/NOFS satellite. J. Geophys. Res. Space Physics, 120, 2263 2275. doi: 10.1002/2014JA020735.

Huba, J. D., G. Joyce, and J. a. Fedder (2000), Sami2 is Another Model of the Ionosphere (SAMI2): A new low-latitude ionosphere model, J. Geophys. Res., 105, 23035, doi:10.1029/2000JA000035.

Huba, J. D., G. Joyce, and J. Krall (2008), Three- dimensional equatorial spread F modeling, Geophys. Res. Lett., 35, L10102, doi:10.1029/2008GL033509.

Huba, J. D., S. L. Ossakow, G. Joyce, J. Krall, and S. L. England (2009), Three-dimensional equatorial spread F modeling: Zonal neutral wind effects, Geophys. Res. Lett., 36(19), 1-5, doi:10.1029/2009GL040284.

Huba, J. D., and G. Joyce (2010), Global modeling of equatorial plasma bubbles, Geophys. Res. Lett., 37(17), 1-5, doi:10.1029/2010GL044281.

Huba, J. D., and J. Krall (2013), Impact of meridional winds on equatorial spread F : Revisited, Geophys. Res. Lett., 40(7), 1268-1272, doi:10.1002/grl.50292.

Hunsucker, R. D. (1991), Radio Techniques for Probing the Terrestrial Ionosphere, Physics and Chemistry in Space, Springer Berlin Heidelberg, Berlin, Heidelberg.

Haerendel, G., and J. V. Eccles (1992), The role of the equatorial electrojet in the evening ionosphere, J. Geophys. Res., 97(A2), 1181-1192, doi: 10.1029/91JA02227.

Hysell, D. L., M. C. Kelley, W. E. Swartz, and D. T. Farley (1994), VHF radar and rocket observations of equatorial spread F on Kwajalein, J. Geophys. Res., 99(A8), 15065, doi:10.1029/94JA00476.

Hysell, D. L., M. F. Larsen, and R. F. Woodman (1997), Julia radar studies of electric fields in the equatorial electrojet, *Geophysical Research Letters*, *24*(13), 1687–1690, doi: 10.1029/97GL00373.

Hysell, D. L., and J. D. Burcham (1998), JULIA radar studies of equatorial spread F, J. Geophys. Res. Sp. Phys., 103(A12), 29155-29167, doi:10.1029/98JA02655.

Hysell, D. L., and J. D. Burcham (1999), Long term studies of equatorial spread F using the JULIA radar at Jicamarca, Journal of Atmospheric and Solar-Terrestrial Physics, 64(12-14), 1531-1543, doi:10.1016/S1364-6826(02)00091-3.

Hysell, D. L. (2000), An overview and synthesis of plasma irregularities in equatorial spread F, J. Atmos. Solar-Terrestrial Phys., 62(12), 1037-1056, doi:10.1016/S1364-6826(00)00095-X.

Hysell, D., and J. Burcham (2002), Long term studies of equatorial spread F using the JULIA radar at Jicamarca, Journal of Atmospheric and Solar-Terrestrial Physics, 64(12-14), 1531-1543, doi:10.1016/s1364-6826(02)00091-3.

Hysell, D. L., and J. L. Chau (2004), Interpreting the Doppler spectrum of coherent scatter from topside equatorial spread F, J. Atmos. Solar-Terr. Phys., 66, 1549-1557.

Hysell, D. L., M. F. Larsen, C. M. Swenson, and T. F. Wheeler (2006), Shear flow effects at the onset of equatorial spread F, J. Geophys. Res. Sp. Phys., 111(11), 1-9, doi:10.1029/2006JA011963.

Hysell, D. L., and Chau, J. L. (2006), Optimal aperture synthesis radar imaging, Radio Sci., 41, RS2003, doi:10.1029/2005RS003383.

Kelley, M. C., Haerendel, G. , Kappler, H. , Valenzuela, A. , Balsley, B. B., Carter, D. A., Ecklund, W. L., Carlson, C. W., Häusler, B. and Torbert, R. (1976), Evidence for a Rayleigh-Taylor type instability and upwelling of depleted density regions during equatorial spread F. Geophys. Res. Lett., 3: 448-450. doi:10.1029/GL003i008p00448.

Kelley, M. C., and T. Maruyama (1992), A Diagnostic Model for Equatorial Spread F, 2, The Effect of Magnetic Activity, J. Geophys. Res., 97(A2), 1271-1277, doi:10.1029/91ja02607.

Kelley, M. C. (2009), The Earth's Ionosphere: Plasma Physics and Electrodynamics, Second Edition, Academic Press, San Diego.

Kelley, M. C., F. S. Rodrigues, R. F. Pfaff, and J. Klenzing (2014), Observations of the generation of eastward equatorial electric fields near dawn, Ann. Geophys., 32(9), 1169-1175, doi:10.5194/angeo-32-1169-2014.

Kintner, P. M., B. M. Ledvina, and E. R. de Paula (2007), GPS and ionospheric scintillations, Space Weather, 5, S09003, doi: 10.1029/2006SW000260.

Krall, J., J. D. Huba, S. L. Ossakow, G. Joyce, J. J. Makela, E. S. Miller, and M. C. Kelley (2011), Modeling of equatorial plasma bubbles triggered by non-equatorial traveling ionospheric disturbances, Geophys. Res. Lett., 38(8), 2-6, doi:10.1029/2011GL046890.

Krall, J., J. D. Huba, and D. C. Fritts (2013), On the seeding of equatorial spread F by gravity waves, Geophys. Res. Lett., 40(4), 661-664, doi:10.1002/grl.50144.

Kudeki, E., B. G. Fejer, D. T. Farley, and H. M. Ierkic (1981), Interferometer studies of equatorial F region irregularities and drifts, Geophys. Res. Lett., 8(4), 377-380, doi:10.1029/GL008i004p00377.

Kudeki, E., S. Bhattacharyya, and R. F. Woodman (1999), A new approach in incoherent scatter F region ExB drift measurements at Jicamarca, J. Geophys. Res., 104(A12), 28145-28162, doi:10.1029/1998JA900110.

Li, G., B. Ning, M. A. Abdu, X. Yue, L. Liu, W. Wan, and L. Hu (2011), On the occurrence of postmidnight equatorial F region irregularities during the June solstice, J. Geophys. Res., 116, A04318, doi:10.1029/2010JA016056.

Li, G. et al. (2012), Equinoctial and june solstitial F-region irregularities over Sanya, Indian J. Radio Sp. Phys., 41(2), 184198.

Liu, C. H. (1989), World ionosphere/thermosphere study. WITS handbook, Volume 2, SCOSTEP, 1989.

Liu, H.-L., B. T. Foster, M. E. Hagan, J. M. McInerney, A. Maute, L. Qian, A. D. Richmond, R. G. Roble, S. C. Solomon, R. R. Garcia, D. Kinnison, D. R. Marsh, A. K. Smith, J. Richter, F. Sassi, and J. Oberheide (2010), Thermosphere extension of the Whole Atmosphere Community Climate Model, *J. Geophys. Res. Sp. Phys.*, *115*(A12), A12302, doi:10.1029/2010JA015586.

Liu, H.-L., C. G. Bardeen, B. T. Foster, P. Lauritzen, J. Liu, G. Lu, D. R. Marsh, A. Maute, J. M. McInerney, N. M. Pedatella, L. Qian, A. D. Richmond, R. G. Roble, S. C. Solomon, F. M. Vitt, and W. Wang (2018), Development and Validation of the Whole Atmosphere Community Climate Model With Thermosphere and Ionosphere Extension (WACCM-X 2.0), *J. Adv. Model. Earth Syst.*, *10*(2), 381–402, doi:10.1002/2017MS001232.

Liu, J., Liu, H., Wang, W., Burns, A. G., Wu, Q., Gan, Q., et al. (2018). First results from the ionospheric extension of WACCMX during the deep solar minimum year of 2008. Journal of Geophysical Research: Space Physics, 123, 1534 1553. https://doi.org/10.1002/2017JA025010.

MacDougall, J. W., M. A. Abdu, P. T. Jayachandran, J.-F. Cecile, and I. S. Batista (1998), Presunrise spread F at Fortaleza, J. Geophys. Res. Sp. Phys., 103(A10), 23415-23425, doi:10.1029/98JA01949.

Maruyama, T., and N. Matuura (1984), Longitudinal variability of annual changes in activity of equatorial spread F and plasma bubbles, J. Geophys. Res., 89(A12), 10903, doi:10.1029/JA089iA12p10903.

Maruyama, T. (1988), A diagnostic model for equatorial spread F , 1, Model description and application to electric field and neutral wind effects, J. Geophys. Res., 93(A12), 14611, doi:10.1029/JA093iA12p14611.

Martinis, C. R., Mendillo, M. J., and Aarons, J. (2005), Toward a synthesis of equatorial spread F onset and suppression during geomagnetic storms, J. Geophys. Res., 110, A07306, doi:10.1029/2003JA010362.

McClure, J. P., W. B. Hanson, and J. H. Hoffman (1977), Plasma bubbles and irregularities in the equatorial ionosphere, J. Geophys. Res., 82(19), 2650-2656, doi:10.1029/JA082i019p02650.

Navarro, L. A., Fejer, B. G., and Scherliess, L. (2019), Equatorial disturbance dynamo vertical plasma drifts over Jicamarca: Bimonthly and solar cycle dependence. Journal of Geophysical Research: Space Physics, 124, 4833 4841. https://doi.org/10.1029/2019JA026729.

Nicolls, M. J., M. C. Kelley, M. N. Vlasov, Y. Sahai, J. L. Chau, D. L. Hysell, P. R. Fagundes, F. Becker-Guedes, and W. L. C. Lima (2006), Observations and modeling of post-midnight uplifts near the magnetic equator, Ann. Geophys., 24(5), 1317-1331, doi:10.5194/angeo-24-1317-2006.

Ning, B., Hu, L., Li, G. et al., The first time observations of low-latitude ionospheric irregularities by VHF radar in Hainan, Sci. China Technol. Sci. (2012) 55: 1189. https://doi.org/10.1007/s11431-012-4800-2.

Niranjan, K., P. S. Brahmanandam, P. Ramakrishna Rao, G. Uma, D. S. V. V. D. Prasad, and P. V. S. Rama Rao (2003), Post midnight spread-F occurrence over Waltair (17.7°N, 83.3° E) during low and ascending phases of solar activity, Ann. Geophys., 21(3), 745-750, doi:10.5194/angeo-21-745-2003.

Nishioka, M., Su. Basu, S. Basu, C. E. Valladares, R. E. Sheehan, P. A. Roddy, and K. M. Groves (2011), C/NOFS satellite observations of equatorial ionospheric plasma structures supported by multiple groundbased diagnostics in October 2008, J. Geophys. Res., 116, A10323, doi:10.1029/2011JA016446.

Nishioka, M., Y. Otsuka, K. Shiokawa, T. Tsugawa, Effendy, P. Supnithi, T. Nagatsuma, and K. T. Murata (2012), On post-midnight field-aligned irregularities observed with a 30.8-MHz radar at a low latitude: Comparison with F-layer altitude near the geomagnetic equator, J. Geophys. Res., 117, A08337, doi:10.1029/2012JA017692.

Otsuka, Y., T. Ogawa, and Effendy (2009), VHF radar observations of nighttime F-region field-aligned irregularities over Kototabang, Indonesia, Earth, Planets Sp., 61(4), 431-437.

Otsuka, Y., K. Shiokawa, and M. Nishioka (2012), VHF radar observations of post-midnight F-region field-aligned irregularities over Indonesia during solar minimum, Indian J. Radio Sp. Phys., 41, 199-207.

Otsuka, Y. (2018), Review of the generation mechanisms of post-midnight irregularities in the equatorial and low-latitude ionosphere, Progress in Earth and Planetary Science, 5, 57,https://doi.org/10.1186/s40645-018-0212-7.

Patra, A. K., Anandan, V. K., Rao, P. B., and Jain, A. R. (1995), First observations of equatorial spread F from Indian MST radar, Radio Sci., 30(4), 1159 1165, doi:10.1029/95RS00650.

Patra, A. K., P. B. Rao, V. K. Anandan, and A. R. Jain (1997), Radar observations of 2.8 m equatorial spread-F irregularities, J. Atmos. Solar-Terrestrial Phys., 59(13), 1633-1641, doi:10.1016/S1364-6826(96)00162-9.

Patra, A. K., D. V. Phanikumar, and T. K. Pant (2009), Gadanki radar observations of F region field-aligned irregularities during June solstice of solar minimum: First results and preliminary analysis, J. Geophys. Res., 114, A12305, doi:10.1029/2009JA014437.

Picone, J. M., A. E. Hedin, D. P. Drob, and A. C. Aikin (2002), NRLMSISE-00 empirical model of the atmosphere: Statistical comparisons and scientific issues, J. Geophys. Res., 107(A12), 1468, doi:10.1029/2002JA009430.

Prabhakaran Nayar, S. R., T. J. Mathew, C. V. Sreehari, S. G. Sumod, C. V. Devasia, S. Ravindran, V. Sreeja, T. Kumar Pant, and R. Sridharan (2009), Electrodynamics of the equatorial F-region ionosphere during pre-sunrise period, Ann. Geophys., 27(1), 107-111, doi:10.5194/angeo-27-107-2009.

Tulasi Ram, S., K. K. Ajith, M. Yamamoto, Y. Otsuka, T. Yokoyama, K. Niranjan, and S. Gurubaran (2015), Fresh and evolutionary-type field-aligned irregularities generated near sunrise terminator due to overshielding electric fields, J. Geophys. Res. Sp. Phys., 120(7), 5922-5930, doi:10.1002/2015JA021427.

Retterer, J. M. (2005), Physics-based forecasts of equatorial radio scintillation for the Communication and Navigation Outage Forecasting System (C/NOFS), Space Weather, 3, S12C03, doi:10.1029/2005SW000146.

Retterer, J. M., D. T. Decker, W. S. Borer, R. E. Daniell, and B. G. Fejer (2005), Assimilative modeling of the equatorial ionosphere for scintillation forecasting: Modeling with vertical drifts, J. Geophys. Res., 110(A11), A11307, doi:10.1029/2002JA009613.

Retterer, J. M., and L. C. Gentile (2009), Modeling the climatology of equatorial plasma bubbles observed by DMSP, Radio Sci., 44(5), 1-10, doi:10.1029/2008RS004057.

Retterer, J. M., and P. Roddy (2014), Faith in a seed: On the origins of equatorial plasma bubbles, Ann. Geophys., 32(5), 485-498, doi:10.5194/angeo-32-485-2014.

Richmond, A. D. (1989), Modeling the ionosphere wind dynamo: A review, Pure Appl. Geophys. PAGEOPH, 131(3), 413-435, doi:10.1007/BF00876837.

Richmond, A. D., T. W. Fang, and A. Maute (2015), Electrodynamics of the equatorial evening ionosphere: 1. Importance of winds in different regions, J. Geophys. Res. A Sp. Phys., 120(3), 2118-2132, doi:10.1002/2014JA020934.

Rishbeth, H. (1971). The F-layer dynamo. Planetary and Space Science, 19(2), 263267. https://doi.org/10.1016/0032-0633(71)90205-4.

Rodrigues, F. S., E. R. de Paula, M. A. Abdu, A. C. Jardim, K. N. Iyer, P. M. Kintner, and D. L. Hysell (2004), Equatorial spread F irregularity characteristics over São Luís, Brazil, using VHF radar and GPS scintillation techniques, Radio Sci., 39,RS1S31, doi:10.1029/2002RS002826.

Rodrigues, F. da S. (2008), Incoherent and coherent scatter radar studies of the equatorial F region, Cornell University.

Rodrigues, F. S., D. L. Hysell, and E. R. de Paula (2008), Coherent backscatter radar imaging in Brazil: large-scale waves in the bottomside F-region at the onset of equatorial spread F, Ann. Geophys., 26(11), 3355-3364, doi:10.5194/angeo-26-3355-2008.

Rodrigues, F. S., de Paula, E. R., and G. K. Zewdie (2017), High-resolution coherent backscatter interferometric radar images of equatorial spread F using Capon's method, Ann. Geophys., 35, 393-402, doi:10.5194/angeo-35-393-2017.

Roble, R. G., E. C. Ridley, A. D. Richmond, and R. E. Dickinson (1988), A coupled thermosphere/ionosphere general circulation model, Geophys. Res. Lett., 15(12), 1325-1328, doi:10.1029/GL015i012p01325.

Sastri, J. H. (1999), Letter to the Editor: Post-midnight onset of spread-F at Kodaikanal during the June solstice of solar minimum, Ann. Geophys., 17(8), 1111-1115, doi:10.1007/s00585-999-1111-4.

Scannapieco, A. J., and S. L. Ossakow (1976), Nonlinear equatorial spread F, Geophys. Res. Lett., 3(8), 451-454, doi:10.1029/GL003i008p00451.

Scherliess, L. and Fejer, B. G. (1997). Storm time dependence of equatorial disturbance dynamo zonal electric fields. Journal of Geophysical Research, 102(A11), 24,03724,046. https://doi.org/10.1029/97JA02165.

Scherliess, L., and B. G. Fejer (1999), Radar and satellite global equatorial F region vertical drift model, J. Geophys. Res., 104(A4), 6829-6842, doi: 10.1029/1999JA900025.

Schunk, R., and A. Nagy (2009), Neutral atmospheres. In Ionospheres: Physics, Plasma Physics, and Chemistry (Cambridge Atmospheric and Space Science Series, pp. 289-334). Cambridge: Cambridge University Press. doi:10.1017/CBO9780511635342.010.

Shidler, S. A., Rodrigues, F., Fejer, B. G., and Milla, M. (2019). Radar studies of height-dependent equatorial F region vertical and zonal plasma drifts. Journal of Geophysical Research: Space Physics, 124, 2058 - 2071. https://doi.org/10.1029/2019JA026476.

Shume, E. B., E. R. De Paula, E. A. Kherani, M. A. Abdu, and C. M. Denardini (2011), Equatorial electrojet plasma irregularities observed during late afternoon by the 30MHz coherent scatter radar in São Luís, Brazil, J. Atmos. Solar-Terrestrial Phys., 73(1112), 15601567, doi:10.1016/j.jastp.2011.02.015.

Smith, J. M., F. S. Rodrigues, and E. R. De Paula (2015), Radar and satellite investigations of equatorial evening vertical drifts and spread F, Ann. Geophys, 33, 1403-1412, doi:10.5194/angeo-33-1403-2015.

Smith, J. M., F. S. Rodrigues, B. G. Fejer, and M. A. Milla (2016), Coherent and incoherent scatter radar study of the climatology and day-to-day variability of mean F region vertical drifts and equatorial spread F, J. Geophys. Res. Sp. Phys., 121(2), 1466-1482, doi:10.1002/2015JA021934.

Smith, J., and Heelis, R. A. (2017). Equatorial plasma bubbles: Variations of occurrence and spatial scale in local time, longitude, season, and solar activity. Journal of Geophysical Research: Space Physics, 122(5), 5743-5755. https://doi.org/10.1002/2017JA024128.

Smith, J. M., and Heelis, R. A. (2018). The Plasma Environment Associated With Equatorial Ionospheric Irregularities. Journal of Geophysical Research: Space Physics, 123(2), 1583-1592. https://doi.org/10.1002/2017JA024933.

Smith, J. M., and Heelis, R. A. (2018). Plasma Dynamics Associated With Equatorial Ionospheric Irregularities. Geophysical Research Letters, 45(16), 7927-7932. https://doi.org/10.1029/2018GL078560.

Stoneback, R. A., R. A. Heelis, A. G. Burrell, W. R. Coley, B. G. Fejer, and E. Pacheco (2011), Observations of quiet time vertical ion drift in the equatorial ionosphere during the solar minimum period of 2009, J. Geophys. Res. Sp. Phys., 116(12), 1-11, doi:10.1029/2011JA016712.

Sobral, J. H., Abdu, M. A., Zamlutti, C. J. and Batista, I. S. (1980), Association between plasma bubble irregularities and airglow disturbances over Brazilian low latitudes. Geophys. Res. Lett., 7: 980-982. doi:10.1029/GL007i011p00980.

Sobral, J. H. A., Abdu, M. A., Takahashi, H., Taylor, M. J., de Paula, E. R., Zamlutti, C. J., Aquino, M. G., and Borba, G. L. (2002). Ionospheric plasma bubble climatology over Brazil based on 22 years (19771998) of 630 nm airglow observations. Journal of Atmospheric and Solar Terrestrial Physics, 64(1214), 1517 1524. https://doi.org/10.1016/S13646826(02)000895.

Su, Y. J., J. M. Retterer, O. De La Beaujardire, W. J. Burke, P. A. Roddy, R. F. Pfaff, G. R. Wilson, and D. E. Hunton (2009), Assimilative modeling of equatorial plasma depletions observed by C/NOFS, Geophys. Res. Lett., 36(18), 2-5, doi:10.1029/2009GL038946.

Sultan, P. J. (1996), Linear theory and modeling of the Rayleigh-Taylor instability leading to the occurrence of equatorial spread F, J. Geophys. Res. Sp. Phys., 101(A12), 26875-26891, doi:10.1029/96JA00682.

Sulzer, M. P., and S. Gonzlez (1999), The effect of electron Coulomb collisions on the incoherent scatter spectrum in the F region at Jicamarca, J. Geophys. Res., 104(A10), 22535-22551, doi:10.1029/1999JA900288.

Swartz, W. E., and Woodman, R. F. (1998), Same night observations of spreadF by the Jicamarca Radio Observatory in Peru and CUPRI in Alcantara, Brazil, Geophys. Res. Lett., 25(1), 17 20, doi:10.1029/97GL03484.

Tarpley, J. D. (1970), The ionospheric wind dynamo-II. Solar tides, Planet. Space Sci., 18(7), 1091-1103, doi:10.1016/0032-0633(70)90110-8.

Tiwari, D., A. K. Patra, C. V Devasia, R. Sridharan, N. Jyoti, K. S. Viswanathan, and K. S. V Subbarao (2004), Radar Observations of 8.3-m scale equatorial spread F irregularities over Trivandrum, Ann. Geophys., 22(3), 911-922, doi:10.5194/angeo-22-911-2004.

Tsunoda, R. T., Baron, M. J., Owen, J., and Towle, D. M. (1979), Altair: an incoherent scatter radar for equatorial spread F studies, Radio Sci., 14(6), 1111 1119, doi:10.1029/RS014i006p01111.

Tsunoda, R. T. (1985), Control of the seasonal and longitudinal occurrence of equatorial scintillations by the longitudinal gradient in integrated e region pedersen conductivity, *Journal of Geophysical Research: Space Physics*, *90*(A1), 447–456, doi:10.1029/JA090iA01p00447.

Tsunoda, R. T., Bubenik, D. M., Thampi, S. V., and Yamamoto, M. (2010), On largescale wave structure and equatorial spread F without a postsunset rise of the F layer, Geophys. Res. Lett., 37, L07105, doi:10.1029/2009GL042357.

Woodman, R. F. (1970), Vertical drift velocities and east-west electric fields at the magnetic equator, *J. Geophys. Res.*, *75*(31), 6249–6259, doi:10.1029/JA075i031p06249.

Woodman, R., and C. Hoz (1976), Radar observations of F region equatorial irregularities, J Geophys Res, 81(31), 5447-5466, doi:10.1029/JA081i031p05447.

Woodman, R. F. (1985), Spectral moment estimation in MST radars, Radio Sci., 20(6), 1185-1195, doi:10.1029/RS020i006p01185.

Woodman, R. F. (2009), Spread Fan old equatorial aeronomy problem finally resolved? Ann. Geophys., 27, 1915 1934, doi:10.5194/angeo2719152009.

Xiong, C., J. Park, H. Lhr, C. Stolle, and S. Y. Ma (2010), Comparing plasma bubble occurrence rates at CHAMP and GRACE altitudes during high and low solar activity, Ann. Geophys., 28(9), 1647-1658, doi:10.5194/angeo-28-1647-2010.

Yizengaw, E., J. Retterer, E. E. Pacheco, P. Roddy, K. Groves, R. Caton, and P. Baki (2013), Postmidnight bubbles and scintillations in the quiet-time June solstice, Geophys. Res. Lett., 40(21), 5592-5597, doi:10.1002/2013GL058307.

Yokoyama, T., S. Fukao, and M. Yamamoto (2004), Relationship of the onset of equatorial f region irregularities with the sunset terminator observed with the equatorial atmosphere radar, *Geophysical Research Letters*, *31*, L24,804, doi:10.1029/2004GL021529, l24804.

Yokoyama, T., M. Yamamoto, Y. Otsuka, M. Nishioka, T. Tsugawa, S. Watanabe, and R. F. Pfaff (2011), On postmidnight lowlatitude ionospheric irregularities during solar minimum: 1. Equatorial Atmosphere Radar and GPSTEC observations in Indonesia, J. Geophys. Res., 116, A11325, doi:10.1029/2011JA016797.

Yokoyama, T., R. F. Pfaff, P. A. Roddy, M. Yamamoto, and Y. Otsuka (2011), On postmidnight lowlatitude ionospheric irregularities during solar minimum: 2. C/NOFS observations and comparisons with the Equatorial Atmosphere Radar, J. Geophys. Res., 116, A11326, doi:10.1029/2011JA016798.

Yokoyama, T., H. Shinagawa, and H. Jin (2014), Nonlinear growth, bifurcation, and pinching of equatorial plasma bubble simulated by three-dimensional high-resolution bubble model, J. Geophys. Res. Sp. Phys., 119(12), 10474-10482, doi:10.1002/2014JA020708.

Yokoyama, T. (2017), A review on the numerical simulation of equatorial plasma bubbles toward scintillation evaluation and forecasting, Prog. Earth Planet. Sci., 4(1), 37, doi:10.1186/s40645-017-0153-6.

Zalesak, S. T., and S. L. Ossakow (1980), Nonlinear equatorial spread F : Spatially large bubbles resulting from large horizontal scale initial perturbations, J. Geophys. Res., 85(A5), 2131, doi:10.1029/JA085iA05p02131.

Zalesak, S. T., S. L. Ossakow, and P. K. Chaturvedi (1982), Nonlinear equatorial spread F : The effect of neutral winds and background Pedersen conductivity, J. Geophys. Res., 87(A1), 151, doi:10.1029/JA087iA01p00151.

Zhan, W., and F. S. Rodrigues (2018), June Solstice Equatorial Spread F in the American Sector: A Numerical Assessment of Linear Stability Aided by Incoherent Scatter Radar Measurements, J. Geophys. Res. Sp. Phys., 123(1), 755-767, doi:10.1002/2017JA024969.

Zhan, W., Rodrigues, F., and Milla, M. (2018). On the genesis of postmidnight equatorial spread F: Results for the American/Peruvian sector. Geophysical Research Letters, 45, 7354-7361. https://doi.org/10.1029/2018GL078822.

BIOGRAPHICAL SKETCH

Weijia Zhan was born in Hong'an, Hubei, China. After completing his high school at the No. 1 High School of Hong'an County in Hong'an in 2007, Weijia entered Wuhan University in Wuhan, Hubei, China. Then he went on to seek a master's degree in spacephysics at Wuhan University in 2012. In 2015, Weijia graduated from Wuhan University and started to pursue a PhD degree at The University of Texas at Dallas in Richardson, Texas. During his PhD study and research, Weijia focused on seeking a comprehensive understanding of postmidnight ESF irregularities in the American sector through radar and numerical methods.

CURRICULUM VITAE

Weijia Zhan

October, 2019

Contact Information:

Department of Physics
The University of Texas at Dallas
800 W. Campbell Rd.
Richardson, TX 75080-3021, U.S.A.

Email: wxz151530@utdallas.edu

Educational History:

B.S., Communication Engineering, Wuhan University, 2012
M.S., Spacephysics, Wuhan University, 2016
M.S., Physics, University of Texas at Dallas, 2017
Ph.D., Physics, University of Texas at Dallas, 2019

Radar studies of atypical equatorial spread F events in the American sector
Ph.D. Dissertation
Department of Physics, The University of Texas at Dallas
Advisor: Dr. Fabiano Rodrigues

Employment History:

Research Assistant, The University of Texas at Dallas, September 2016 – present
Teaching Assistant, The University of Texas at Dallas, August 2015 – December 2015

Research interests:

Equatorial Ionosphere; Ionosphere-thermosphere coupling

Professional Memberships:

American Geophysical Union (AGU), 2019-present

Publications:

1. **Zhan, W.**, F. Rodrigues, and M. Milla. (2018), On the genesis of postmidnight equatorial spread F: Results for the American/Peruvian sector. *Geophysical Research Letters*, 45, 7354 – 7361. https://doi.org/10.1029/2018GL078822.

2. **Zhan, W.**, and S. Rodrigues, F. (2018). June Solstice Equatorial Spread F in the American Sector: A Numerical Assessment of Linear Stability Aided by Incoherent Scatter Radar Measurements. *Journal of Geophysical Research: Space Physics*, 123(1), 755 –767. https://doi.org/10.1002/2017JA024969.

3. Rodrigues, F. S., Hickey, D. A., **Zhan, W.**, Martinis, C. R., Fejer, B. G., Milla, M. A., and Arratia, J. F. (2018). Multi-instrumented observations of the equatorial F-region during June solstice: large-scale wave structures and spread-F. *Progress in Earth and Planetary Science*, 5(1), 14. https://doi.org/10.1186/s40645-018-0170-0.

4. Fabiano S. Rodrigues, **Weijia Zhan**, Marco A. Milla, Bela G. Fejer, Eurico R. de Paula, Acacio C. Neto, Angela M. Santos, and Inez S. Batista, Melissa: system description and spectral features of pre- and post-midnight F-region echoes, accepted by *Journal of Geophysical Research: Space Physics*.

5. Cai, H., Li, F., Shen, G., **Zhan, W.**, Zhou, K., McCrea, I.W. and Ma, S. 2014, "E layer dominated ionosphere observed by EISCAT ESR radars during solar minimum", *Annales Geophysicae*, vol. 32, no. 10, pp. 1223 – 1231.

6. ZHOU Kang-Jun, CAI Hong-Tao, CHENG Li-Jun MA Shu-Ying, **ZHAN Wei-Jia**, SHEN Ge, LI Fei, 2014. Feature of ion up-flow at high-latitude topside ionosphere during geomagnetic storms from the Defense Meteorological Satellite Program. *Chinese Journal Of Geophysics*, 57(11): 3541 – 3550, doi: 10.6038/cjg20141106.

7. SHEN Ge, CAI Hong-Tao, LI Fei, ZHOU Kang-Jun, **ZHAN Wei-Jia**, HUANG Ding-Juan, 2014. EISCAT/ESR radar observations of ELDI in polar region during solar minimum. *Chinese Journal Of Geophysics*, 57(11): 3532 – 3540, doi: 10.6038/cjg20141105.

Conference presentations:

1. CEDAR-GEM Joint Workshop, Santa Fe, NM — Jun 2016
2. International ISR Summer School, Sodankyl, Finland — Jul 2016
3. National Radio Science Meeting (URSI), Boulder, CO — Jan 2017
4. CEDAR Workshop, Keystone, CO — Jun 2017
5. National Radio Science Meeting (URSI), Boulder, CO — Jan 2018
6. CEDAR Workshop, Santa Fe, NM — Jun 2018
7. CEDAR Workshop, Santa Fe, NM — Jun 2019

Awards and Honors:

1. 2017 USNC-URSI Student Fellowship Award, Boulder, CO Jan 2017
2. 2017 Betty and Gifford Johnson Scholarship, UTDallas, Richardson, TX Nov. 2017
3. 2018 USNC-URSI Student Fellowship Award, Boulder, CO Jan 2018
4. 2018 Renfrow Student Support Fund, UTDallas, March 2018